MM SCALE 3D SILICA WAVEGUIDE FABRICATION TECHNIQUE FOR SOLAR ENERGY CONCENTRATION SYSTEMS

A Dissertation

by

YUSUF DOGAN

Submitted to the Office of Graduate and Professional Studies of
Texas A&M University
in partial fulfillment of the requirements for the degree of

DOCTOR OF PHILOSOPHY

Chair of Committee,	Christi K. Madsen
Committee Members,	Ohannes Eknoyan
	Mehrdad Ehsani
	Alexey Belyanin
Head of Department,	Miroslav M. Begovic

December 2018

Major Subject: Electrical Engineering

Copyright 2018 Yusuf Dogan

ABSTRACT

The overreaching goal of this dissertation research is to achieve fabrication of mm scale waveguide structure for solar energy concentration systems. In the proposed design, a high concentrator photovoltaics (HCPV) with 1000x concentration and >90 % optical efficiency is targeted. The concept consists of three components: lens array, coupler and waveguiding section. Fused silica is assigned as the waveguide material, since it has a high optical transmission and low absorption and it provides the scalability and low manufacturing cost sought in the fabrication technique. To acquire the desired shape in waveguide, femtosecond laser irradiation followed by chemical etching (FLICE) process is used for fused silica light pipes fabrication. Among two widely used etchants potassium hydroxide (KOH) is preferred over hydrogen fluoride (HF) regarding its higher selectivity. FLICE process parameters have been optimized to achieve higher selectivity, higher manufacturing speed and better surface quality. The minimum number of overlapped pulses is reduced to 3.2 which corresponds to 1.25 m/s writing speed at given 2 MHz laser pulse repetition rate at given 2 µm spot size and an acceptable filtered surface roughness of 400 nm for 1 mm^2 area is achieved. The achieved minimum filtered surface roughness is scaled down to 21.8 nm for given 1 mm^2 area. Up to 1X5 staggered and tapered light pipes with up to 12.75x geometric concentration factor with a 45° angled input facet is successfully fabricated. The achieved accuracy of the angled surfaces is smaller than ±0.5° and ±0.01° for 45° and side wall tapered surfaces, respectively. Having evaluated the polishing techniques, CO_2 laser polishing is decided to be employed in this study to obtain a smooth surface finish. Surface profiles are measured by atomic force microscopy (AFM) for generally high spatial frequency analysis and

white light interferometry (WLI) for low spatial frequency analysis. Measurements demonstrate that the surface root mean square (RMS) roughness is decreased almost two order of magnitude. 95 % transmission efficiency is measured for waveguide samples up to 50 mm in length and 1 mm^2 cross sectional area when the Fresnel losses are ignored and incident angles (in air) are averaged according to F/1.5 lens. Complex shapes in waveguides such as angled facets, tapering of the cross-section along the length, and combiners are proven to be possible to fabricate with high precision.

CONTRIBUTORS AND FUNDING SOURCES

Contributors

This work was supervised by a dissertation committee consisting of Professors Christi Madsen, Ohannes Eknoyan and Mehrdad Ehsani of the Department of Electrical and Computer Engineering and Professor Alexey Belyanin of the Department of Physics.

The work conducted for the dissertation was completed by the student independently.

Founding Sources

Graduate study was supported by a fellowship from Texas A&M University and a dissertation research fellowship from ARPA-E.

NOMENCLATURE

AFM	Atomic Force Microscopy
AOM	Acousto-optic Modulator
AR	Anti-Reflection
CPV	Concentrator Photovoltaic
DC	Direct Current
DIW	Deionized Water
FLICE	Femtosecond Laser Irradiation Followed By Chemical Etching
FS	Femtosecond
FWHM	Full Width Half Maximum
HCPV	High Concentrator Photovoltaics
HF	Hydrogen Fluoride
HR	High-Reflection
IPA	Isopropyl Alcohol
IR	Infrared Radiation
KOH	Potassium Hydroxide
MJPV	Multi-junction Photovoltaic
NA	Numerical Aperture
RMS	Root Mean Square
PRR	Pulse Repetition Rate
PSD	Power Spectral Density
PSI	Phase Shifting Interferometry
PV	Photovoltaic
PWM	Pulse Width Modulation
SEM	Scanning Electron Microscopy
TIR	Total Internal Reflection
VSI	Vertical Scanning Interferometry
WLI	White Light Interferometry

TABLE OF CONTENTS

Page

ABSTRACT ii

CONTRIBUTORS AND FUNDING SOURCES iv

NOMENCLATURE v

TABLE OF CONTENTS vi

LIST OF TABLES xii

1. INTRODUCTION 1

1.1 Objective and Motivation 1
1.2 HCPV Project Details 2
1.3 Light Pipes 4
1.3.1 Specifications and Goals 4
1.3.2 Material Selection 7
1.3.3 Light Pipe Fabrication Methods 9
1.3.4 Femtosecond Laser Processing of Glass 11
1.3.5 Surface & Optical Quality 17

2. FLICE EXPERIMENTAL SETUP AND BASIC PROCESS 21

2.1 Experimental Setup 21
2.2 Fs Laser Direct Writing Technique 34
2.3 FLICE Basic Process for Fused Silica 36
2.4 Etching Selectivity Studies 37
2.4.1 Dimensional Control 42
2.4.2 Release Issues 44
2.5 Surface Metrology 45

3. FLICE PROCESS PARAMETERS VS TRADEOFF 48

3.1 Nanogratings 49
3.1.1 Polarization Effect on Nanogratings 50

3.1.2 Number of Overlapped Pulse Effect 51
3.1.3 Pulse Energy Effect on Nanogratings 53
3.2 Selective Etching 55
3.2.1 Pulse Width Effect 56
3.2.2 Polarization Effect on Selective Etching 57
3.3 Prototyped 2D Plane Etching 58
3.3.1 Polarization Effect 60
3.3.2 Pulse Energy Effect 62
3.3.3 Overlapped Number of Pulses 63
3.3.4 2D Optimized Results 64
3.3.5 45° Coupler Surface 69
3.3.6 Other Process Capabilities for Complex Structures 74
4. GLASS POLISHING FOR LOW SURFACE ROUGHNESS AND DEFORMATION OF LIGHT PIPES 77
4.1 Glass Polishing Techniques 77
4.2 CO_2 Laser Processing of Silica 79
4.3 Experimental CO_2 Polishing Setup 81
5. POLISHING PROCESS DEVELOPMENT AND EXPERIMENTAL RESULTS 90
5.1 Raster Scan as a CO_2 Laser Polishing Method 90
5.2 Deformation Analysis 100
5.3 Solutions Attempts 102
5.3.1 Masking 102
5.3.2 Laser On/Off Timing with Pulse Wave 103
5.3.3 Arbitrary Signal Generation 104
5.3.4 Substrate Heating Effect 107
5.3.5 Substrate Material Effect 108
6. SUMMARY 113
REFERENCES 116

LIST OF FIGURES

Page

Figure 1. High-concentration waveguiding architecture: (a) 3D view, (b) side view. 4

Figure 2. 1000x 1x5 staggered waveguide design for prototype 6

Figure 3. Glass cutting techniques schematics and explanations 10

Figure 4. Time scale of laser and material interaction...12

Figure 5. Schematic diagram of nonlinear photoionization...15

Figure 6. The left image represents the type 2 region with nanogratings, while the right image represents the type 3 region with micro explosions 17

Figure 7. The root mean square (RMS) roughness Rq. 19

Figure 8. a) Form, waviness and roughness of the surface and b) spatial wavelength distribution of the surface 20

Figure 9. Schematic of fs laser system..21

Figure 10. Fs laser setup: a) Fs laser amplifier unit, b) external delay generator and AOM with nano precision stage drivers, c) beam optics and workstation..22

Figure 11. a) The power on the stage with modulation efficiency with corresponding system transmission, b) the modulation efficiency effect on pulse energy with 100 and 500 KHz and c) 1ps pulse width measured with autocorrelator 25

Figure 12. Depiction of the beam width as a function of the distance z along the beam 30

Figure 13. Beam profile before and after the beam expander: a) before beam expander and b) after beam expander..31

Figure 14. Focused beam on NIR detector and formed airy disk patterns 32

Figure 15. Required distance for stage speed up 34

Figure 16. Direct writing images: a) complex writing inside silica, b) powerful writing on the surface, c) pulse shots inside of silica sample at low PRR and high scan speed, d) bright and dark field images of birefringent effect of nanogratings resulting from fs laser irradiation...36

Figure 17. Femtosecond laser irradiation followed by chemical etching (FLICE) 37

Figure 18. a) Normalized etch rate over KOH concentration, b) 1D selectivity over time with various KOH etchant....41

Figure 19. Three different silica samples with different purity level and after etching process: a) Corning 7980 fused silica, b) Ted Pella GE124, and c) unknown (Ebay) JGS1 42

Figure 20. a) 1000x 1*5 staggered waveguide design for prototype with separation gap b) laser scribe width during etching c) sample width after etching process 43

Figure 21. a) Cracks at sample edges, b-c) center irradiation and etching problems 44

Figure 22. AFM vs optical profiler feature sizes and resolution 46

Figure 23. The proposed direct writing process for nanograting analysis 48

Figure 24. Cross section SEM images: Perpendicular polarization with 0.4 μJ with 300fs and N = 3333. a) at low magnification (8K scale is 1 μm), b) at high magnification (40K scale is 100 nm), ...50

Figure 25. Cross section SEM images: 300fs, the circular perpendicular and parallel polarization SEM images 51

Figure 26. The number of overlapped pulse N effect for perpendicular (s) polarized light with pulse width of 300fs and pulse energy of 0.8 μJ. 52

Figure 27. Effect of N to nanograting numbers and spacing between them and the laser irradiated region lateral and vertical dimensions for given N....53

Figure 28 SEM images of modified spot with various pulse energies from 0.2 μJ to 1.6 μJ by perpendicular polarized beam which has pulse duration of 1000fs with 1000 overlapped number of pulses. 54

Figure 29. Pulse energy effect on nanograting number and spacing 55

Figure 30. Pulse width affect at various condition on 1D channel selectivity a) for 300 fs, b) for 1000 fs....56

Figure 31. Polarization effect on selectivity with various channel writing conditions....57

Figure 32. 2D plane writing direction with combination of multiple 1d writing from bottom to up with z increments 59

Figure 33. Laser irradiation and released material from 1 mm fused silica substrate after chemical etching. 60

Figure 34. White light interferometry images, profiles and microscope images of the surfaces which are written at 1 mm/s and 0.4 μJ with parallel, perpendicular and circular polarizations, respectively....61

Figure 35. Surface profiles which are written in perpendicular polarization with various pulse energy 63

Figure 36. Surfaces which are written in perpendicular polarization at 0.55 μJ pulse energy with various writing speeds 64

Figure 37. The microscope images of scanned surface with various writing condition....65

Figure 38. Surface roughness over overlapped number of pulses with 3 different polarization. ..66

Figure 39. Microscope images of scanned surfaces for optimization....67

Figure 40. The laser writing conditions for best surface quality 68

Figure 41. Some of the optimized configurations for the application needs for high manufacturing speed, complex writing and high surface quality. 69

Figure 42. Top and bottom face of fabricated 45° coupler surface 70

Figure 43. The modified focal spot before and after etching....71

Figure 44. AFM images of etched surface with various z a) $\Delta z = 15$ μm, b) $\Delta z = 3$ μm....72

Figure 45. 45° coupler surface microscope images with various z increment and z increment vs surface roughness of all coupling surface (1 x 1.41 mm^2)....73

Figure 46. Microscope image of 45° surfaces for angle measurement....74

Figure 47. Released the tapered surface without cracks at corners a) top view, b) side view....74

Figure 48. The cracks at the corners are prevented after optimizing the coding....76

Figure 49. a) 1x3 straight staggered light pipe, b) 1x2 bi-directional tapered light pipe....76

Figure 50. Schematic of polishing setup....82

Figure 51. Attenuated copies of the reflected and transmitted beams 84

Figure 52. The experimental setup consists of the CO_2 laser, diode pointer, isolator, beam splitter and shutter 85

Figure 53. The laser polishing work station with stages, heater, vacuum chuck and imaging systems....86

Figure 54. Laser exposure on silica rod with defocused laser beam 87

Figure 55. X direction raster scan polishing and deformation analysis....91

Figure 56. Y direction raster scan and polishing and deformation analysis 92

Figure 57. One pass Y+X direction raster scan polishing and deformation analysis with AFM and microscope images 93

Figure 58. Polishing test with multiple passes Y+X direction raster scan of AFM and microscope images....94

Figure 59. Microscope and AFM images of rough surface before and after polishing 95

Figure 60. The profile, PSD and slope of the surface before and after polishing....96

Figure 61. Raster scan polished surfaces a) Microscope images, b) true profile and c) filtered profile with Sq_gf = 121 nm, 34 nm and 11 nm, respectively....97

Figure 62. a) Large beam one scan and b) surface profile behaviors over various polishing levels. 99

Figure 63. Surface profiles of three different polishing methods 100

Figure 64. a) One pass laser scan on y and x axis b) surface profile after scan....101

Figure 65. Laser beam effect on edge....101

Figure 66. Surface profile of polished sample under mask layer. 103

Figure 67. Surface change over exposure duration, square pulse timing (20 KHz, 80 % PWM, ~2 mm radius, Ton/off = 150/50ms, 1sec, 3sec and 5sec) 104

Figure 68. Surface profiles of samples polished with arbitrary PWM signal....106

Figure 69. Surface profile of polished sample under 35% and 80% PWM with cold and hot substrate 108

Figure 70. Surface profiles of two polished samples at 35% and 80% PWM with tungsten carbide and silica substrate on hot plate 109

Figure 71. Non-polished side surface profile of polished sample to observe the corners 110

Figure 72. 70 mm silica sample surface profiles 112

Figure 73. Polished sidewall surface and proposed prototype....115

LIST OF TABLES

Page

Table 1. Properties of some candidate materials 8

Table 2. Laser parameters 23

Table 3. Accuracy of horizontal tapered surface angle 75

Table 4. Contact free polishing techniques 77

Table 5. CO_2 laser parameters 82

Table 6. Laser polishing parameters for PWM control 105

Table 7. CO_2 laser polishing parameters for heat effect study 107

Table 8. CO_2 laser polishing parameters for substrate material effect 109

Table 9. CO_2 laser polishing parameters for long silica rod polishing 111

1. INTRODUCTION

1.1 Objective and Motivation

Solar energy, the most important source of renewable energy, refers to energy from the sun which is powerful, completely free, found in abundance and produced for billions of years. More energy from the sun strikes on the earth in one hour than is used by everyone in the world in one year according to the National Renewable Energy Laboratory (NREL) solar energy discussion. The consumption of non-renewable sources like oil, gas and coal is increasing at an alarming rate making it a must to search for other renewable sources of energy. The large magnitude of solar energy makes it a highly appealing source of electricity. Although solar energy is utilized extensively in many countries, still there is a long way to exploit this energy to fulfill the daily demand for energy.

Radiant heat and light from the sun can be harnessed and converted to usable energy with a variety of modern technologies like photovoltaic. Photovoltaic (PV) cells convert sunlight to direct current (DC) electricity. The first PV cells were made of silicon combined, or doped, with other elements to affect the behavior of electrons and holes. The low efficiency of conventional PV system and its reaching to the maximum theoretical limits makes researcher find some alternative solutions to satisfy the increasing power need. Currently concentrator photovoltaics (CPV) are studied as an alternative.

CPV is a photovoltaic system employing optical light collectors such as lenses and mirrors, yielding optical concentration devices which focus the light into smaller and highly efficient multi junction solar cells differing from the conventional silicon based photovoltaic systems. CPV

consists of multiple p-n junctions each of which has different wavelength range. Theoretically multi junction cells has an efficiency of 86.8 % while the conventional photovoltaic system has around 34 % efficiency limit. [1]

CPV systems can be separated in three groups: low (<10x), medium (10x to 100x) and high (>100) concentration systems. These systems use solar trackers to promote their performance and efficiency more. However, HCPV requires two axes tracking with precision allowing most of the direct incident sunlight hitting the solar cells.[2] The multi junction cells in HCPV requires more sophisticated cooling systems, which can be costly.[3] Nowadays many researchers are focusing on to find solutions to the cooling systems, additional diffuse light collection and uniform temperature distribution on multi-junction solar cells.

On the other hand, CPV reduces the system cost as it utilizes quite smaller size cells and less semiconductor material. Optical components of the system are relatively cheaper than Si PV cells. CPV systems are environmentally friendly due to highly reduced amount of semiconductor material.

1.2 HCPV Project Details

The promising increase in multi-junction solar cell efficiency and the decrease in the price with upcoming technologies, the willingness of using multi-junction solar cell is growing. However; the price of these cell is relatively more expensive than the regular Si PV cells. Concentrator photovoltaics is considered as a potential solution to overcome this price challenge. There are significant amount of commercially available applications of CPV by using lenses and mirrors. The system, on the other hand, requires multi-junction cells for each focal point due to the nature of concentrator photovoltaics. Thus, a system with a high vertical distance is used. Using

this gigantic systems brings some issues with itself. First of all, it requires more vertical space which consumes more materials and gets expensive accordingly. Moreover, CPV system employs solar tracking and this gets complicated and needs expensive tracking control systems.[4] Wiring of the multi-junction solar cells causes another problem because spot size gets smaller, it is nearly impossible to get a MJ solar cell and this results in low concentration. Finally, cell efficiency decreases and more complex and expensive cooling systems are required as the temperature over the MJ solar cell is not uniform due to high focusing intensity. To overcome all of this challenge, the waveguiding is offered as a solution.[5, 6] The regular HCPV with waveguiding systems consist of a three-layer structure: lens array as primary concentration, coupler for coupling the light to the planar waveguide, waveguide for the transmission of the light to multi-junction solar cell with uniform output.[7] Excellent illumination uniformity of the MJPVs is provided as well as a common edge for heat dissipation to minimize temperature-related degradations.

In this dissertation, a compact HCPV system design with a planar light pipe as a waveguide is proposed as illustrated in Figure 1. In proposed structure 3 by 5 lens array is used to concentrate the direct normal incident light to the coupler face with roughly 90x concentration. One directional and two directional taperings in light pipe are used to provide secondary concentration to give additional 12.75x concentration. With both concentrations, geometrical concentration of the overall system will be higher than 1000x with an acceptance angle of $> \pm 0.9°$ without micro tracking. The 45˚ high reflective surface is used for coupling the light coming from lens to the light pipe, and there is no separate coupling element. Light hitting the mirror is reflected into the waveguides. As each staggered reflective 45˚ surface and tapered sidewalls are physically separated from the previous light pipe with micron scale gap, light already coupled into the light

pipe will not hit the subsequent reflective surface and tapered surface, which avoid the decoupling issue. In addition, the proposed design also allows the diffuse light collection by using conventional Si PV solar cells at the bottom of the light pipe. More than 5 % extra efficiency can be collected with the bottom PV cells.

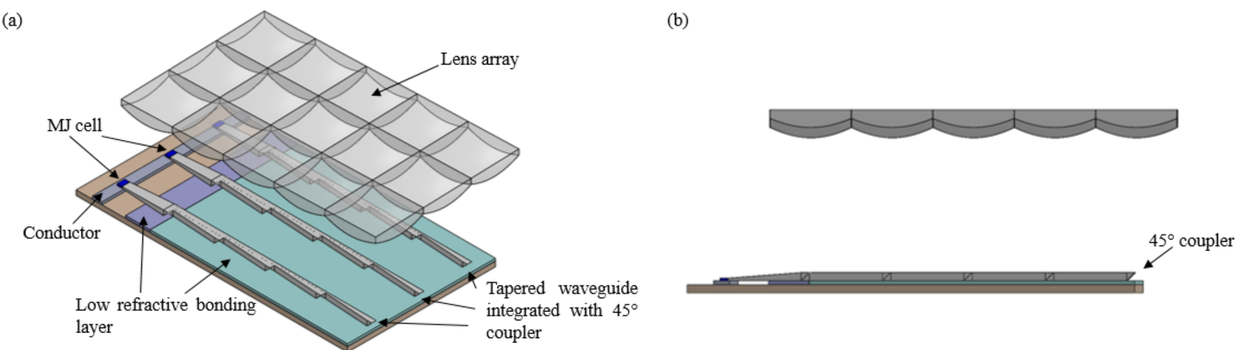

Figure 1. High-concentration waveguiding architecture: (a) 3D view, (b) side view.

1.3 Light Pipes

1.3.1 Specifications and Goals

Light pipes as multimode waveguides are the structures for guiding the light by restricting the spatial region in which light can propagate. With the use of coupler, the concentrated sunlight gets into the light pipe and couples into the photovoltaic cells or thermal receivers. This light pipe can also be used as secondary concentrator that not only deliver the light but also confine it into a smaller area. Another benefit of light pipes is that it has a uniform output of light due to multiple reflections of the light inside the light pipe. This uniform distribution increase efficiency of solar cell and help us to control the temperature on solar cell. Light pipe is the essential part of our overall design in terms of achieving the high efficiency goal. This essential part is expected to have

high transmission to get the highest efficiency. In our proposed CPV design, we aim to achieve more than 90 % transmission efficiency of whole optical system which requires a nearly ideal optical quality light pipe.

In addition to straight light pipes, we have demonstrated light pipes with advanced geometries such as angled facets, tapered cross-sections and combiners with micron-scale precision. A 45° angled input facet allows the focused light from the lens element to be coupled into the light pipe. The light from multiple lens elements can be combined into a single light pipe. Cascaded structures have been fabricated for coupling two (2x1) and three (3x1) lens elements into a common output. We have also fabricated 5x1 staggered light pipe. Novel methods to keep the light from decoupling at a subsequent 45° facet include a narrow slit. The effective kerf width after etching is measured to be less than 25 μm for a 1 mm-deep etch.

Tapered waveguide structures are key elements to reach high concentration. A complex prototype including horizontal tapering and bi-directional tapering, as well as 45° angled coupler surfaces, is shown in Figure 2. Tapered light pipes with magnification factors up to 12.75x for concentrating light were fabricated with a 45° angled input facet to turn the beam and a straight output facet to couple to the solar cell. For tapering, control over the laser irradiation path allows us to obtain precise tapering in the horizontal and vertical directions. We have demonstrated 45° and 4° plane tapered 3D shape silica light pipe structure. The accuracy and precision are the important criteria to meet the desired efficiency for the prototype.

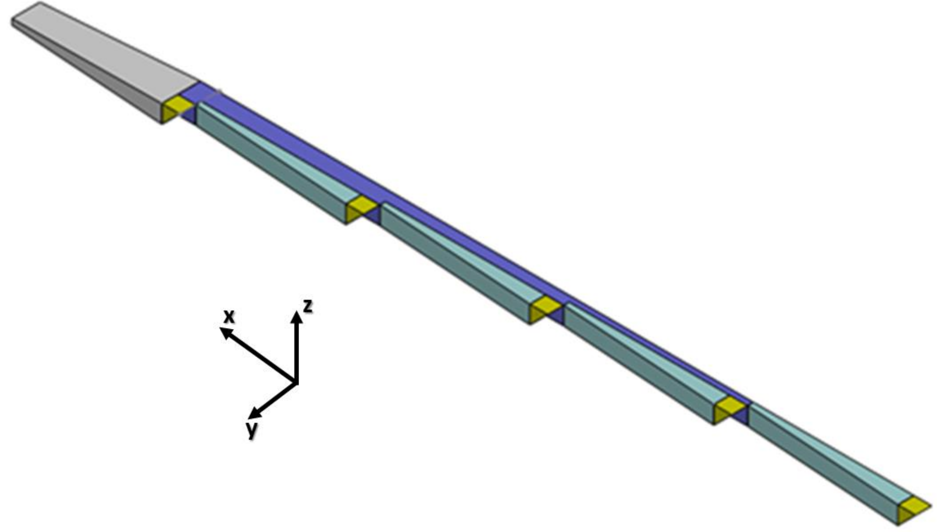

Figure 2. 1000x 1x5 staggered waveguide design for prototype

The light pipe for the HCPV project was first designed as being tapered in two directions right after the coupling surface. However, this design was not only decreasing the efficiency by confining the light on the z axis at the front end of the light pipe but also it was making the fabrication process even more difficult. The proposed design is made up of one piece that includes side tapering on y axis for each staggering and tapering on z axis at the end of the light pipe.

The width of the first light pipe is 0.9 mm. For each reflection at the tapered surface, the incident angle will be increased by a tapered angle θ. Since the light can propagate in the light pipe by TIR (total internal reflection), the incident angle has to be smaller than the critical angle. In order to avoid multiple reflection at the tapered surface, there is a spacing of 25 μm between each tapered zone and the side light pipe. So that the light only hits the tapered surface once and will not hit the tapered surface of the next light pipes. Thus, the width of the rest of the waveguide is 0.89 mm. The total width is reduced to 0.316 mm at the end of each individual light pipe. The

required total width of outlet will be 5*0.316 mm with the addition of 5 lens arrays in the system. The thickness of the waveguide is 1 mm and is reduced to 0.316 mm at the end of the waveguide array. The proposed 1x5 staggered waveguide design can be seen in Figure 2. While the vertical maximum dimension is 1 mm, the lateral dimension changes with added number of lens arrays. The maximum lateral dimensions 53.7 mm in x direction and 2.16 mm in y direction as the proposed is a 1x5 staggered waveguide. The outlet facet size of the light pipe is 0.316 mm in z and 1.58 mm in y direction. Thus, concentration for 1x5 proposed design is calculated as followed:

$$C_{waveguide} = \frac{Coupler\ Area}{Cell\ Area} = \frac{0.9 * \sqrt{2}}{0.316 * 0316} = 12.75$$

$$C_{system} = \frac{Lens\ Area}{Cell\ Area} = \frac{10.74 * 10.74}{0.316 * 0316} = 1115.14$$

There is a limitation on the length of staggered waveguide or number of lenses in one row. Several parameters can affect the waveguide length. For a given design the number of lenses in array can be extended up to 29 lens with the adjusted offset angle between the lens array and light pipe. The light coming from each staggered coupling region goes straight without striking the following 45 degree surface by a small air gap to prevent the previous coming lights from hitting the following tilted surface. And this process continues for each coupling area with satisfying the total internal reflection (TIR) condition.

1.3.2 Material Selection

Waveguides are constructed with different kinds of materials each of which offers distinctive features. In the decision-making process about the material of the waveguide structure certain criteria such as reflective index, absorption, thermal resistance are evaluated. Refractive

index is desired to be as high as possible as the light is concentrated and coupled to the waveguide from the lens. On the other hand, the waveguide should be kept non-absorptive along Am1.5 solar spectrum. Thermal resistance is sought to prevent any deformation on the waveguide. When the material is less absorptive, the temperature effect will not play an important role. Some other demanded criteria are being solid phase, commercially available, and eligible to some post processing. Evaluating these criteria as seen in Table 1 and previous waveguide study references, fused silica has been determined to be the best candidate for the waveguide material in this solar concentrator project.

Table 1. Properties of some candidate materials

Materials	**Corning 7980 Fused Silica**	**N-BK7**	**PMMA**
Transmission Range 250-1800 nm	180-2100	380-2100	400-1800
Refractive Index @550 nm	1.46	1.52	1.49
Knoop Hardness Kg/mm^2	522	610	20
Density g/cm3 @25C	2.20	2.51	1.18
Young's Modulus GPa	71	82	2.5
Tensile Strength MPa	54	n/a	62
Thermal Conductivity W/(m K)	1.38	1.11	0.2
Melting Point	1650	557°C	130
Thermal Expansion Coefficient (K–1) x 10-6	0.57	7.1	75

1.3.3 Light Pipe Fabrication Methods

While typical planar waveguides are fabricated using thin film deposition followed by photolithography and etching, the desired thickness for solar concentrator applications does not lend itself to thin film deposition approaches. So, we determined that making the light pipes from a glass substrate with the desired maximum thickness would be a better starting point. Glass as a light pipe material offers advantages like low loss, broadband and high concentration. The glass type materials possess the disadvantage of fragility making the cutting process a challenging task since one can easily end up breaking the glass into pieces. However, using some laser cutting technologies instead of conventional techniques like diamond tool cutting will not only eliminate the fragility but also furnish the glass with flexibility by eliminating the micro and nano cracks at edges.[8, 9]

Many glass cutting techniques have been studied and analyzed so far. These techniques can be separated into two main groups: conventional and non-conventional. The conventional technique diamond cutting is simply marking and scribing the glass using a diamond point tool and applying an external force to break the glass along the scribing path. [9, 10] Although scribing provides high precision and accuracy, it results in irregular cutting, poor surface finish and material deformation. It is known to develop internal cracks which may reduce the strength of glass to 60 %. Moreover, it is not suitable for complex cutting. Among non-conventional cutting techniques the most suitable one for our application is laser cutting which has advantages of better surface quality, complex shapes cutting, noncontact process and quick and optimum cost. Nearly all of the fabrication techniques mentioned in Figure 3 have not been able to prove the feasibility of 3D

micromachining. However, laser cutting of glass is getting popular with intensive capabilities of new laser processing.

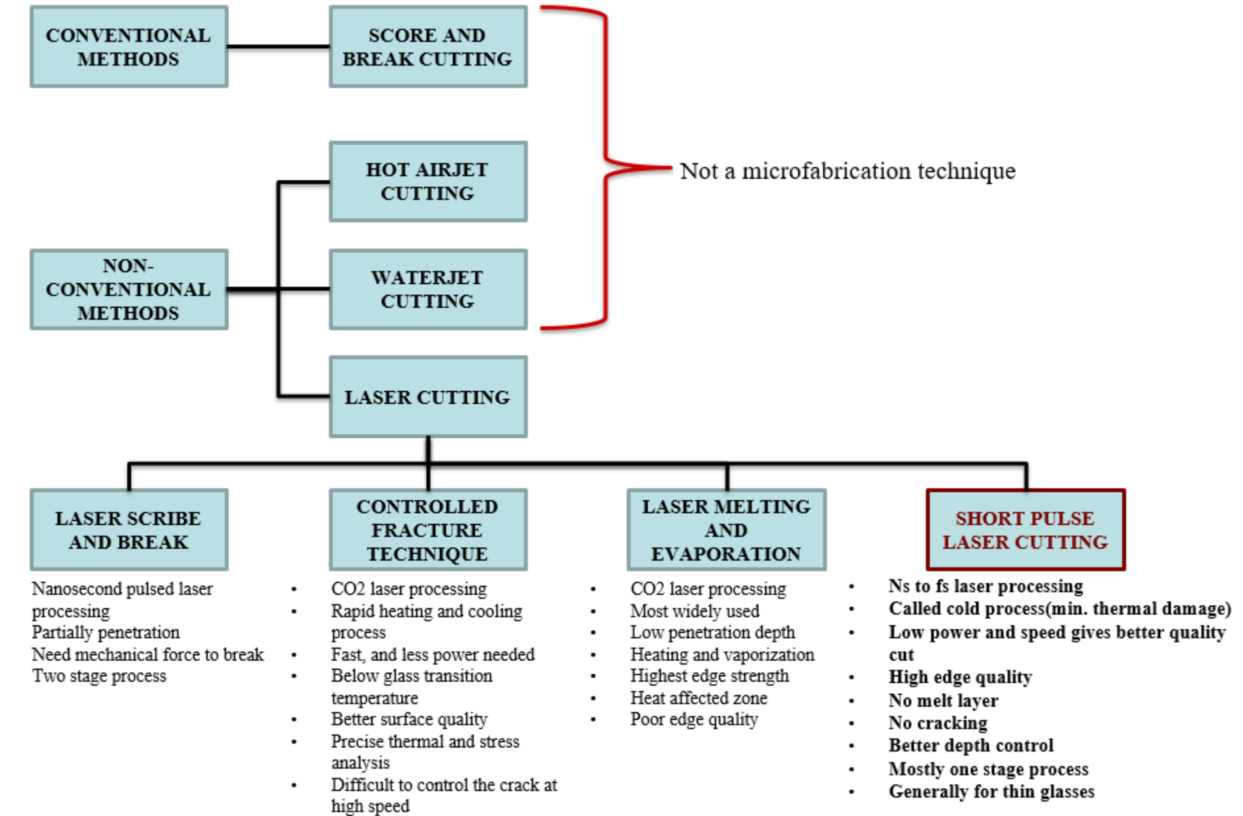

Figure 3. Glass cutting techniques schematics and explanations

All glass cutting techniques are summarized in the diagram shown in Figure 3. There are several laser cutting techniques, but the short pulse laser gives us the best cutting potential due to having key virtues for our purpose like minimized environmental thermal damage, high edge quality, no melt layer, no cracking, and better depth control.[11]

Ultrafast lasers offer a unique 3D capability within transparent materials and enable space selection resulting from the nonlinear interaction with the transparent material. A diverse range of

modifications inside materials are rendered with tight focus feature and direct writing. These modifications can be exemplified with refractive index modification [12], nanovoid and nanograting formation [13, 14], element distribution, nanocrystallization and nonreciprocal writing[15-17]. More than one function can be induced in a single substrate by changing the physical and chemical properties of transparent materials using ultrafast laser pulses. [16]

Laser can be described as a self-sustained oscillator for light, and explained by light amplification by stimulated emission of radiation (Laser). The laser obtains the optical gain from the laser active media, thus laser out gets higher power than laser in. The laser gets back to media via a feedback loop. For lasing condition the gain of power that laser gets should be higher than the loss of power the laser losses due to outcoupling, scattering and absorption. In other words, the lasing condition, light amplifying medium and feedback should be satisfied to generate laser. As a lasing material there is a broad emission according to wavelength spectrum in recombination process. Depending on the laser cavity or feedback loop distance only at defined wavelengths and its harmonics can survive. The circulated pulses hit the coupler mirror and emit a pulse to the output while this circulation decides the pulse repetition rates. The fiber laser has a gain media of fiber doped with ytterbium, which amplifies the laser.[18] Because the laser is mode locked, it is capable of emitting short pulses. If the laser has a larger bandwidth with more modes, this will result in shorter pulse widths. Ultrashort pulses are available thanks to mode locked laser which also improves the nonlinear effect on transparent materials due to its high peak power intensity.

1.3.4 Femtosecond Laser Processing of Glass

Among short pulsed lasers femtosecond lasers are the newest and getting popular day by day. Femtosecond laser systems have been the center of interest in science and industry to satisfy

the ever-growing demand for high quality transparent material fabrication which has a wide spectrum of usage in various areas including medicine, material engineering, metrology, telecommunication and energy. Femtosecond laser microfabrication offers elimination of crack fabrication, 3D microfabrication limitations and low fabrication rates encountered in conventional methods.[19, 20]

The time scale of laser and material interaction is shown in Figure 4. In femtoseconds photon excites the electron, in picoseconds the absorbed energy is transferred to the lattice, in nanoseconds the shockwave spreads, and in microseconds thermal energy diffuses. [8, 21]

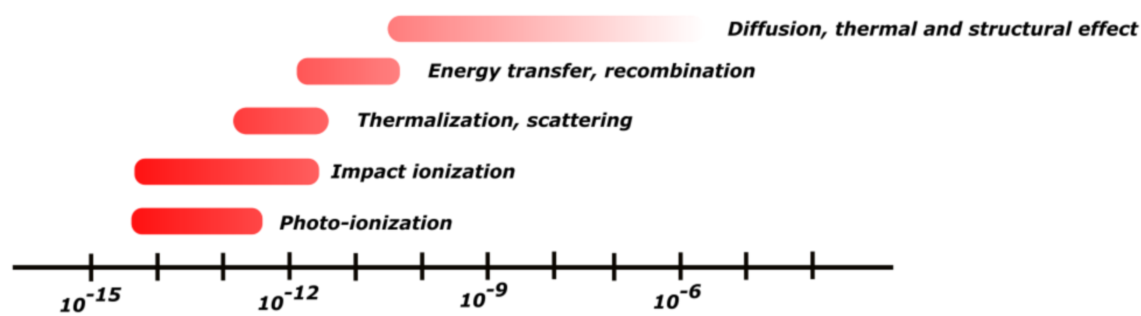

Figure 4. Time scale of laser and material interaction

Femtosecond lasers, generate ultra-short pulses with time durations from a few femtoseconds to several hundred femtoseconds up to a few picoseconds to minimize the damage to any of the surrounding tissues and make material modifications on the micron scale with minimal or precisely controllable effects. The energy of each pulse can be found by diving the average laser power to laser pulse repetition rate as calculated in the below equation:

$$E_p = \frac{P_{avg}}{PRR}$$

where $E_p$is pulse energy in joule, $P_{avg}$is the average power of the laser emitting in watt, PRR is the pulse repetition rate of laser which refers the number of pulses in seconds.

Because the fs laser has short pulse duration, it has a very high peak power intensity. Pulse duration can be defined in couple ways, but the most practical one is full width half maximum (FWHM) which refers the distance between the points and means the half of the maximum intensity on a Gaussian beam.

$$P_{pk} = \frac{E_P}{D_{pulse}}$$

where P_{pk} is peak power energy in watt, D_{pulse} is the pulse width of the laser in seconds. There is an inverse relation between the pulse duration and peak power. When the laser pulse duration decreases, the peak power increases even when they have the same pulse energy.

There are couple pulse generation mechanisms like modulation by continuous wave light source, gain switching, Q switching, mode locking and high harmonic generation. The generation of fs scale pulse duration became possible with the improvements in passive mode locking technique.[22]

The laser is normally not perfect that cannot emit only one wavelength during recombination process and the emitted beam has a bandwidth due to the laser gain medium. According to the used gain medium, the bandwidth can change from 0.001 nm to 500 nm. The fs laser produces a laser beam which has a center wavelength with a large bandwidth. In the optical cavity with high reflective mirrors, the light moves back and forth, increases the laser intensity in gain medium, and makes a standing wave with discrete wavelengths. All other wavelengths

diminishes due to the destructive interference. At a given cavity length, the laser has much higher modes in the cavity and the laser excites all these multi modes. These various modes generate a strong pulse via constructively interference. More number of modes or more broadband mode locked frequencies generate shorter pulse widths. The pulse repetition rate is determined by the frequency of the burst pulse travelling between the two reflective mirrors one of which is slightly less reflective than the other. The transmitted pulse then propagates to the laser aperture.

Fs laser interaction with transparent materials is an interesting topic that is to be highlighted. The material is normally transparent to the laser wavelength. For silica sample, it is totally transparent to the given fs lasers which have wavelengths of in visible or near infrared range which is totally transparent for glass substrate. Thus, there is no linear absorption of laser pulses inside the silica substrate. However; the laser intensity will be pretty high at the spot size with the help of both focusing and short pulses when the short pulse laser is focused inside the silica substrate with the objective lens. This high peak intensity at 10^{15} watt/cm^2 will trigger the nonlinear absorption by increasing the absorption coefficient which is optical intensity dependent. Laser intensity on nonlinear absorption coefficient is studied in some studies.[23] There is also a self-focusing effect in transparent materials that the intense optical exposure change the refractive index of the material, and this affected zone focuses the beam more.[24]

Light absorption is nonlinear in transparent materials as mentioned above and causes optical damage with transferring electrons from the valence band to the conduction band: photoionization and avalanche ionization are the two nonlinear excitation mechanisms for nonlinear absorption which cause permanent damage inside the transparent materials.[25, 26]

The photoionization mechanism consist of two regimes: tunneling ionization regime and multiphoton ionization as describe in Figure 5. With the tunneling ionization, the suppression of atomic potential barrier with strong laser electric field, the electron in valence band tunnels become free. With multiphoton ionization, an electron moves from valence band to conduction band with absorption of multiple photons. Number of photons absorbed times photon energy (1.2eV for λ = 1030 nm) should be equal or greater than transparent material band gap (Eg = 8.9eV for silica sample). Then it will generate free electrons. For avalanche ionization, the election at conduction band excited by photons moves to the higher energy level. Then the electron which has enough kinetic energy can ionize another electron from valence band. According to applied intensity regime the dominant ionization changes from multiphoton ionization to tunneling ionization zone.

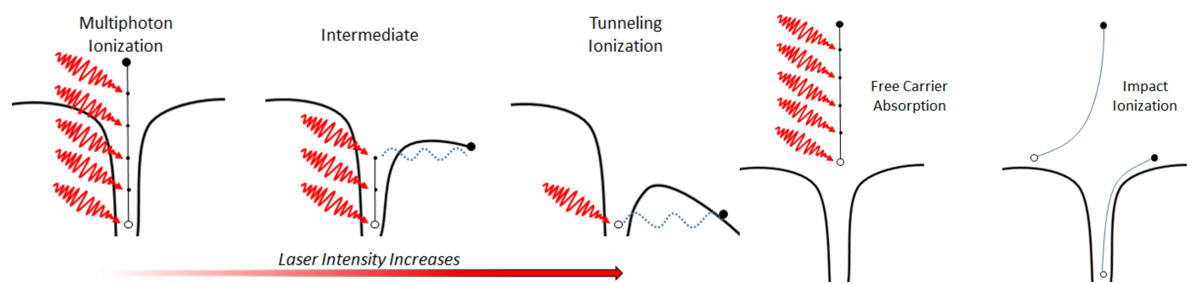

Figure 5. Schematic diagram of nonlinear photoionization

Photoionization and avalanche ionization can happen at the same time. The tunneling ionization occurs when the optical intensity is increased. The psychics behind this interaction is still under investigation in reference to the material change with nanoplasma generation. Keldysh *et al.* developed a parameter that represents the relation between multiphoton and tunneling ionization regimes. According to their study, the process is related to laser wavelength, laser

intensity and material band gap, refractive index and effective mass. And they made a correlation between those parameters. For Keldysh parameter (γ) is smaller than 1.5, tunneling ionization occurs. For γ is nearly 1.5, combination of tunneling and multiphoton ionization occurs. For γ is greater than 1.5, the multiphoton ionization occurs. The Keldysh parameter is defined with equation below.

$$\gamma = \frac{\omega}{e}\sqrt{\frac{m_e c n_0 \varepsilon_0 E_g}{I}}$$

where ω is frequency, e is charge of the electron, m_e is effective mass, c is the speed of light, n is the refractive index, ε_0 is the electric permittivity, E_g is the bandgap energy and I is the laser intensity.[25]

The free electrons in conduction band, after electron hole pair generation, turn into nonradiative recombination like lattice vibration (phonon). In other words, for short pulse irradiation photon electron interaction is faster than the energy transfer from hot free electron to phonon. As a result of the irradiation, the material can undergo a phase or structural modification that causes localized permanent change or even void. The region modified by fs laser exposure is more prone to be etched with general etchants than the non-modified region.[27]

The modification at the focal region groups into three types relating to pulse energy and duration: while Type 1 describes the homogeneous refractive index increase, Type 2 describes even formation of nanogratings that low and high refractive index formation happens perpendicular to polarization and Type 3 describes uneven formation of nanogratings and gaps due to micro explosion.[28] SEM images of Type 2 and 3 regions are given in Figure 6.

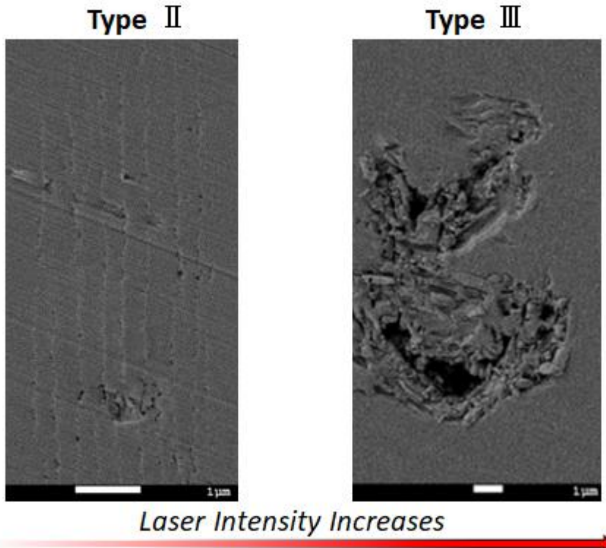

Figure 6. The left image represents the type 2 region with nanogratings, while the right image represents the type 3 region with micro explosions

The ultrashort pulse laser technology is getting promising solutions for vast variety of applications for both industry and science. With developing laser production, the lasers getting more robust to use in difficult environment. There are intensive application areas for short pulse laser and some of the application areas are nano-surgery like cataract surgery [29], two photon imaging of cells [30], spectroscopy [31], defense like infrared countermeasure (CM) applications [32], optical communications and remote sensing through aerosol [33], polymerization [34], material processing [35], microfluidic application [36], rapid prototyping of photonic devices such as waveguides [37], active devices [38], filters [39], resonators [40].

1.3.5 Surface & Optical Quality

Surface defects such as scratches, pits or digs may increase absorption, cause damage, easily break the TIR condition and negatively affect the efficiency. The surface can be noted as

standard, precision and high precision quality as the scratches and diameter of digs are changing. The surface quality is quantified by calibrated standards published by institutions like International Organization for Standardization (ISO), American National Standards Institute (ANSI) and military standard (MIL-STD).

The surface flatness is another criteria for surface quality. To understand the surface flatness, the sample is placed under the focused beam and the shape of fringes and separation are checked. If the sample has straight and uniformly separated fringes, the surface can be denominated as optically flat. The parallel difference between the tangent line of the bended fringe at center and the parallel line at edge of the fringe indicate the surface flatness. A surface is called as typical, precision and high precision grade, when the separation is 1λ, $\lambda/4$ and $\lambda/20$ respectively.

A Surface finish is described as typical, precision and high precision quality, when the surface RMS roughness is about 5 nm, 2 nm and 0.5 nm respectively. The RMS roughness refers the standard deviation of the surface profile. While Rq represents RMS roughness of a line, Sq. represents the RMS roughness of an area. Even if there are different representations of surface roughness, the root mean square of a surface (RMS) is chosen to evaluate our test results. Peaks and valleys affects RMS roughness more than the average roughness, bringing about the fact that Rq values are higher than the Ra values.

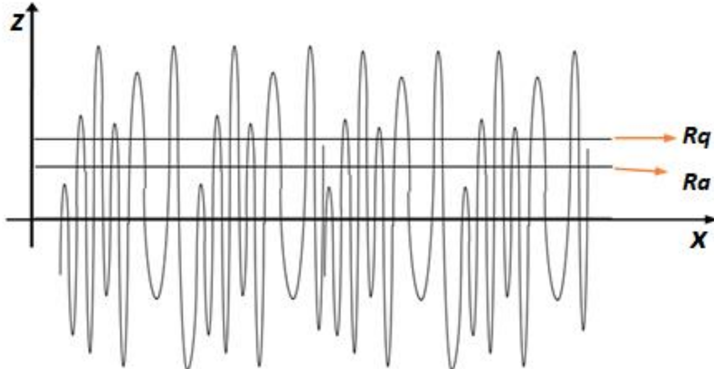

Figure 7. The root mean square (RMS) roughness Rq.

$$R_q = \sqrt{\frac{1}{a}\int_0^a Z^2(x)dx}$$

$$S_q = \sqrt{\frac{1}{ab}\int_0^b \int_0^a Z^2(x,y)dxdy}$$

where a defines the distance on x axis, b defines the distance on y axis, z defines the vertical distance at given data points.

The surface profile is composed of spatial wavelength or frequencies. While the higher wavelength represents the form of the surface, the lower the wavelength shows the roughness of the surface as shown in Figure 8.[41] In addition to the importance of the roughness, the waviness and surface form also important for most optical experiments. Figure 8 shows the surface profile from roughness to form with representation of spatial wavelength.

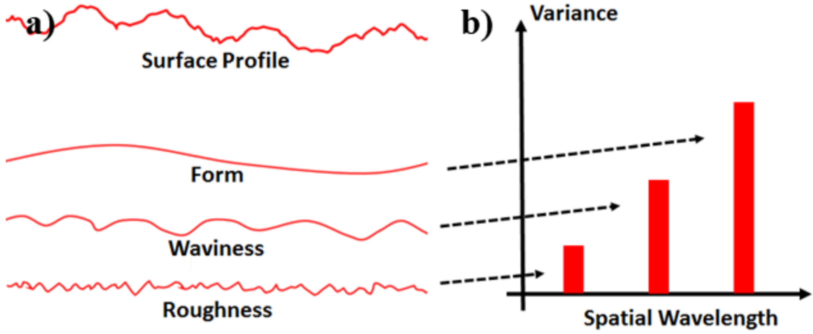

Figure 8. a) Form, waviness and roughness of the surface and b) spatial wavelength distribution of the surface

2. FLICE EXPERIMENTAL SETUP AND BASIC PROCESS

In this chapter, an approach known as femtosecond laser irradiation followed by chemical etching (FLICE) technique will be addressed and brought bear on a glass sample to achieve the targeted 3D shape of light pipe. We will discuss fs laser setup and specifications, optical beam path details, laser control and focusing, polarization effect, and alignment details, direct writing technique and basic process for fused silica with sample preparation, laser exposure, etching selectivity, etchant types, dimension control, release issues and surface measurement details.

2.1 Experimental Setup

Our high energy femtosecond laser machining system includes a mode locked fiber fs laser, Aerotech high precision positioning stages and automation control system. The fs laser schematic and experimental setup images are represented in Figure 9 and Figure 10 respectively.

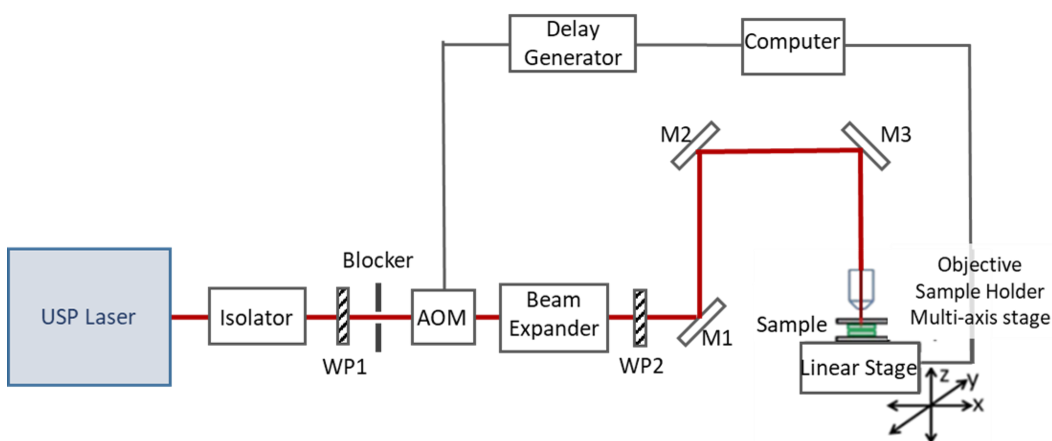

Figure 9. Schematic of fs laser system

a)

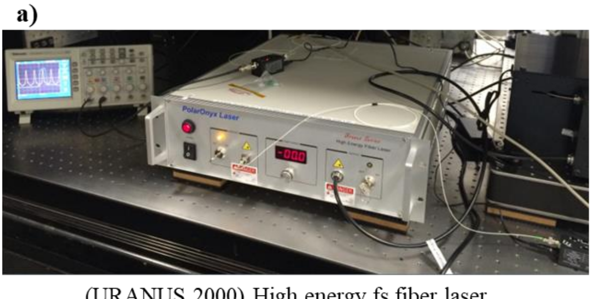

(URANUS 2000) High energy fs fiber laser

b)

c)

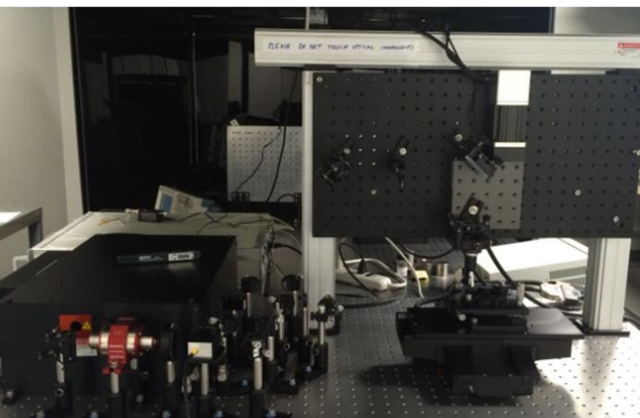

Optical elements and motorized stages

Figure 10. Fs laser setup: a) Fs laser amplifier unit, b) external delay generator and AOM with nano precision stage drivers, c) beam optics and workstation

The workstation for laser system is shown in Figure 10 for FLICE process. The fs laser is mode locked fiber laser (Uranus, PolarOnyx Laser Inc.) generating full width half maximum (FWHM) of 800 fs pulses at wavelength of 1030 nm with pulse repetition rate (PRR) of 100 KHz and maximum pulse energy of nearly 20 μJ with beam propagation ratio of 1.3. The beam propagation ratio refers the beam quality that shows the difference of the beam from ideal Gaussian profile. The PRR and pulse energy is adjusted via external delay generator and acousto-optic modulator (AOM). The polarization of the beam is linearly polarized. The beam is focused by 20x high power micro focusing objective (0.4 NA). The process is controlled by Aerotech nano positioning stages on XYZ planes. Another Ytterbium-doped photonic crystal fiber fs laser that we used in our experiment is (Satsuma, Amplitude Systems) due to its ability to change the pulse

width and relatively high repetition rate. It generates 300 fs to 4 ps pulses at 1030 nm with up to 2 MHz repetition rate and it delivers 20 µJ with beam propagation ratio of 1.2. In our studies we used both femtosecond lasers which gave us broader perspective and ability to optimize tests by manipulating laser parameters with a great variety of choices. Laser parameters are compared in Table 2.

Table 2. Laser parameters

	Uranus	**Satsuma**
Average Power	2 W	> 10 W
Pulse Energy	> 20 µJ	> 20 µJ
Pulse Duration	700-800 fs	< 350 fs to 10 ps
Repetition Rate	up to 100 KHz	up to 2 MHz
Wavelength	1030 nm	1030 nm
Beam Quality	M^2 <1.3	M^2 < 1.2
Beam Size at Aperture	3 mm	2 mm

Nd:Yag fiber femtosecond laser is operating at 1030 nm with 300fs to 1ps and up to 2 MHz pulse repetition rate with maximum 20 µJ pulse energy. The laser focuses on high precision X-Y and Z stages after bouncing couple mirrors, beam expander, and high power focusing objective. After adjusting the beam at far field and placing the focusing objective, the beam is aligned according to its reflection from Kentek IR detector which converts 900 nm to 1700 nm IR light to visible green color. Maximizing the power transmission through the focusing objective helps us place the center the focusing objective. Fine tuning of the laser adjustment is carried out by means

of visible interference fringe pattern. To hold the sample on the stage along the process, a vacuum holder is designed to keep the silica plate at a fixed location without vibration. Al holder surface that conducts with silica plate is finely polished to improve the vacuum force and efficiency. Once the sample is placed at center of the holder, the relatively high powered laser beam is irradiated on the plate. The laser beam moved on z axis by nanopositioning z stages to find the beam spot on the 1 mm thick silica plate. Due to high intensity of the laser pulse and plasma generation at the beam spot, the z position of silica sample is defined at nearly 5 μm z resolution Following the identification of the z location of the sample, the stage is moved around the sample to further adjust the sample tip and tilted with the adjustments knobs. The silica sample and holder surface is cleaned with cotton swabs wetted with deionized water (DIW), Methanol and Isopropyl alcohol (IPA) in order.

Laser parameters are measured by equipments such as power meters, beam profiler, autocorrelator and other optical tools. Thermal power meters changes the optical power to heat with using some absorptive material for specified wavelength range and measures the temperature difference between the absorbed material and ambient environment. For power meter selection there are couple important parameters that should be taken into account like detector type, wavelength range, power range, maximum power and pulse energy density and response time. Autocorrelator is a device used to measure the pulse duration. Because the pulse duration of short pulse laser is around 10^{-15}s, there are no optoelectronic tool that can detect that short time. However, autocorrelator uses interferometric approach to measure the pulse width. The coming laser beam splits to two copies via beam splitter. While one of them is reflected by a fixed mirror, the other beam is reflected by a movable mirror which generate delay on the pulse. And those

reflected beams get combined each other and time delay can be measured with cross correlation of two pulses. Measured pulse energy, power, transmission efficiency and pulse width can be seen in Figure 11. The transmission efficiency is the ratio of the power measured after objective and the power after the laser head. It is observed that the system transmission efficiency decreases with power increase due to the losses at optical beam path.

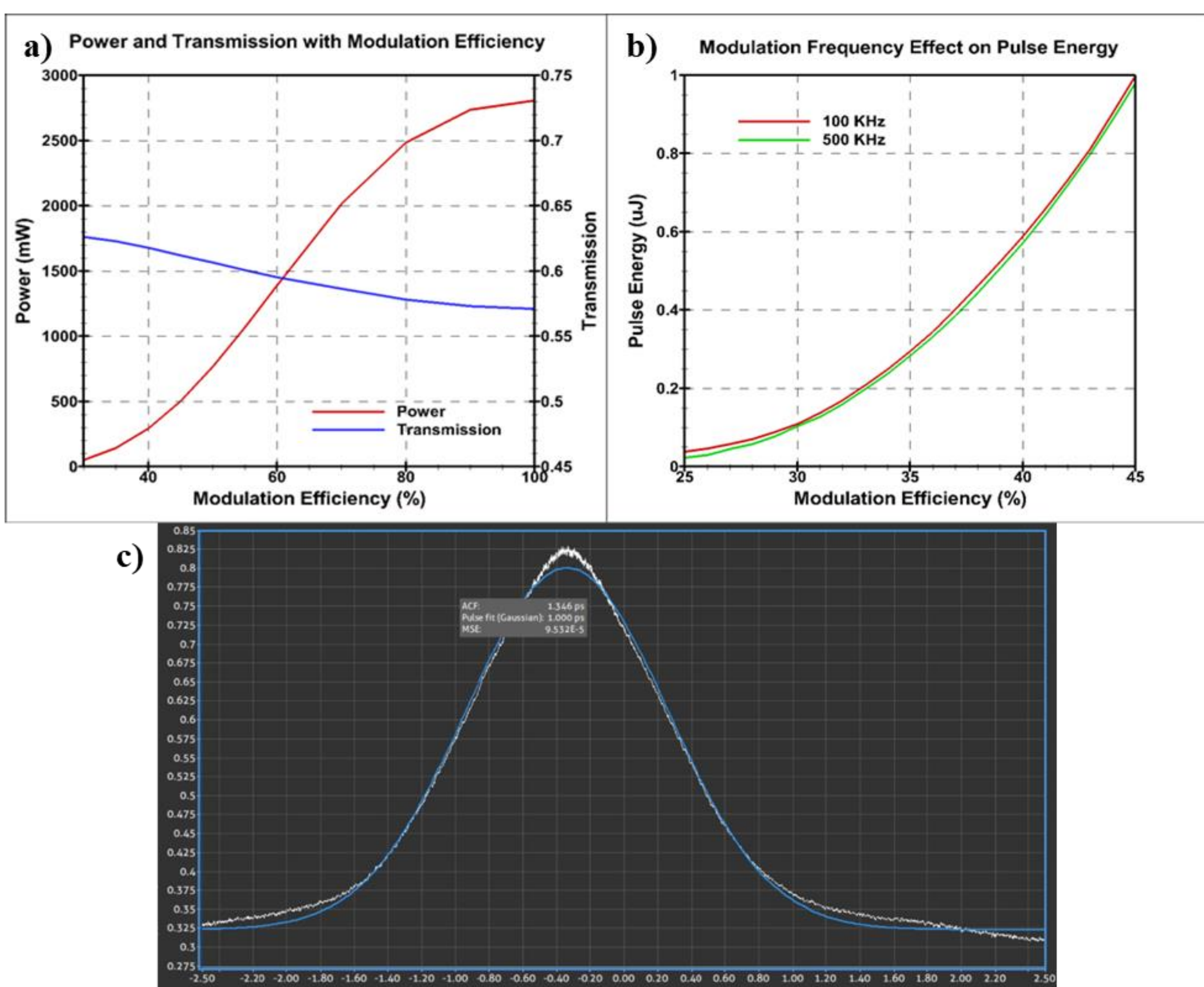

Figure 11. a) The power on the stage with modulation efficiency with corresponding system transmission, b) the modulation efficiency effect on pulse energy with 100 and 500 KHz and c) 1ps pulse width measured with autocorrelator

A periscope assembly from Thorlabs is used to elevate and redirect the beam coming directly from the laser. The periscope has a full range of rotation redirecting the beam while it is elevating, and it changes the polarization of the beam. The beam path is redirected to expand the beam at initial phase of the experiments, a beam expander was used later on to control the beam size and corresponding focusing. The variable beam expander (Altechna) is made up of two lens pairs for diverging and converging the beam and it is capable of expanding the beam from 2x to 8x.

High power optical isolator is used for protecting the laser from back reflection. The isolator consists of two main components, Faraday rotator optics and polarizers. The Faraday rotator optic should have high damage threshold, low refractive index and high transmission over the given laser wavelength. The optic should also be so small that it should not be affected by self-focusing. Another important part of isolator is polarizers which are located at the two sides of the isolator. To achieve the best performance, the input polarization assembly of the optical isolator should be adjusted in accordance with the laser polarization. When the input polarization of the isolator is adjusted vertically, the output polarization should be adjusted at 45° on the axis. This way, the light will directly pass through the isolator. The 45° polarized and back reflected light will get additional 45 degree rotation and the horizontal polarized light will not pass through the input polarizer and not able to reach to the laser. In the isolator, the pulse broadening caused by Faraday rotator is one of the main concerns especially for the short pulse laser systems due to the dispersion of light. The dispersion caused by Faraday rotation could be a significant impact for less than 100 fs pulse width. In our system it will not pose a problem as we have pulse width of larger than 100fs. The beam polarization for the experiment is controlled by waveplates. The

waveplate is an optical element managing the polarization direction. It has discrete refractive indexes at each orientation like parallel or perpendicular to the optical axis. Different propagation speeds between the waves switch the polarization of the beam.

Polarization has a key role for our applications. Although the output of the fs laser beam is linearly polarized after isolator, periscope and other optics, the position may change; so the polarization should be controlled during the experiments. To control the polarization, both zero order half wave plate and quarter waveplate optics are used. The polarization optics are mounted on rotation stages for a more effective usage. Polarization is checked with polarizer and power meter.

For PolarOnyx setup we used an external acousto-optic modulator (AOM) to control the power of the beam. AOM helps managing the intensity of light and works as a mechanical shutter. The power of RF signal is influential on the amount of diffracted light. The rise time of a modulator is one of the key parameters that determines the delay of the system. The modulator response is related to input beam diameter. Fast modulation requires lower rise time and tight beam focusing. An overall AOM selection depends on many criteria like wavelength, power, beam diameter, polarization and extinction ratio.

Implementation of AOM as a shutter necessitates high on/off state difference which means high extinction ratio. Therefore, the first order diffracted beam leading us more than 90 % transmission efficiency should be used.

Both nanoprecision stages and AOM is monitored and controlled by A3200 motion controller software by using G codes. The laser on/off state and intensity are modulated by connecting the stage drivers' digital output pins to AOM driver digital input pins. The transmitted

signal noise is one of the key factors that have an impact on the laser power fluctuation. To eliminate or minimize the noise, low pass filters are utilized.

AOM is an optical device to control the laser with on and off state or between while keeping the laser beam coming from the laser is not affected. AOM basically has an optical medium that when the sound wave running through it, the molecules vibrates, and the medium density changes. The AOM driver generates RF signal and is converted to sound wave via piezoelectric transducer which is attached to crystal medium. This sound wave causes compression and rarefactions states in the crystal medium with density and pressure variations.[42]

Refractive index is high in the compression area and low in the rarefaction region. Hence, the sound wave creates the density varied medium. This periodicity of refractive index changed material is directed by altering the sound wave frequencies. Sound wave propagates as planar wave which has an equation of

$$S_{(x,t)} = S_0 cos(kx - wt)$$

where $S_0$is amplitude, k is wavenumber and w is angular frequency.

The refractive index change depends on the amplitude of the wave: it increases as the amplitude of RF signal gets larger, and it will lead more diffraction to the 1st order which is going to the system while zero order or non-diffracted beam hits to beam blocker. The periodic structures of these refractive index changed region make some refraction on the incident beam when the constructive interference condition is satisfied:

$$2dsin(\theta) = n\lambda$$

where d is the distance between the two compressions, θ is incident angle of the beam, n is an integer and λ is the incident beam wavelength. AOM has optical material of crystalline quartz and

sound wave should have nearly 6000 m/s velocity in glass media with accepting the wave as plane and longitudinal wave. The operating frequency of the AOM is 80 MHz which generates 75 μm (d) periods of compression and rarefaction regions in quartz material. Then the Bragg angle can be found close to 7 mrad that the angle of the diffracted light should be twice of the Bragg angle which is 14 mrad. The reflected beam can be separated from the original or undeflected beam only at the Bragg angle. There is a small frequency shift due to the interaction between laser and acoustic wave.

The AOM drivers have a fixed frequency, but the amplitude can differentiate with input voltage. The amplitude is non-effective for the Bragg angle while the frequency can influence the Bragg angle. The RF power controls the sound wave amplitude, density, refractive index change and diffracted beam power. There is a time delay due to the travelling time of the sound wave. Repetition rate of the laser can be adjusted by using delay generator that generates another digital signal for AOM driver. The delay generator is functionally similar with pulse generator but it has a much higher time resolution.

To quantify the beam parameters, the laser beam is considered to have a Gaussian distribution. There are many ways to define the beam radius like 1/e2 intensity, full width at half maximum and 86.5 % of the beam energy. In all of these different beam width definitions 1/e2 intensity criteria is used for further explanations. The $1/e^2$ width equals nearly 13.5 % of the maximum intensity. The optical intensity of Gaussian function can be calculated as:

$$I(r,z) = \frac{P}{\pi w_z^2/2} exp(-2\frac{r^2}{w_z^2})$$

where P is power, r is distance from the center of the beam, z is the distance on beam propagation direction and w_z is beam radius at the intensity is equal to 13.5 % of the maximum intensity. The beam radius can be calculated as:

$$w_z = w_0\sqrt{1 + (z/z_R)^2}$$

where w_0 is the minimum beam diameter which is located at the beam waist, z_R is Rayleigh range which is the distance from the beam waist that the beam diameter is increases by a factor of √2, and can be calculated as:

$$z_R = \frac{\pi w_0^2}{\lambda M^2}$$

Far field beam divergence can be found from the equation below:

$$\theta = \frac{M^2\lambda}{\pi w_0}$$

where $M^2$is beam quality.

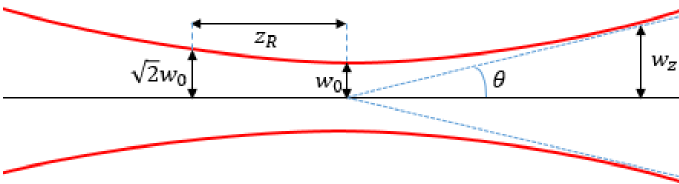

Figure 12. Depiction of the beam width as a function of the distance z along the beam

Beam quality of the laser beam is measured 1.14 and 1.10 for x and y direction respectively. This is increasing the beam ellipticity which is measured 0.96. Thus, in the setup the beam on x direction is diverging more than on y direction. Beam diameter at laser aperture is measured nearly

2 mm which has Rayleigh range of 2.7 m. The beam expander is set to 4x that makes the laser beam diameter 7.95 mm. Before and after beam expander profile images are shown in Figure 13. After following couple mirrors, the beam dimeter gets 8.2 mm on the objective.

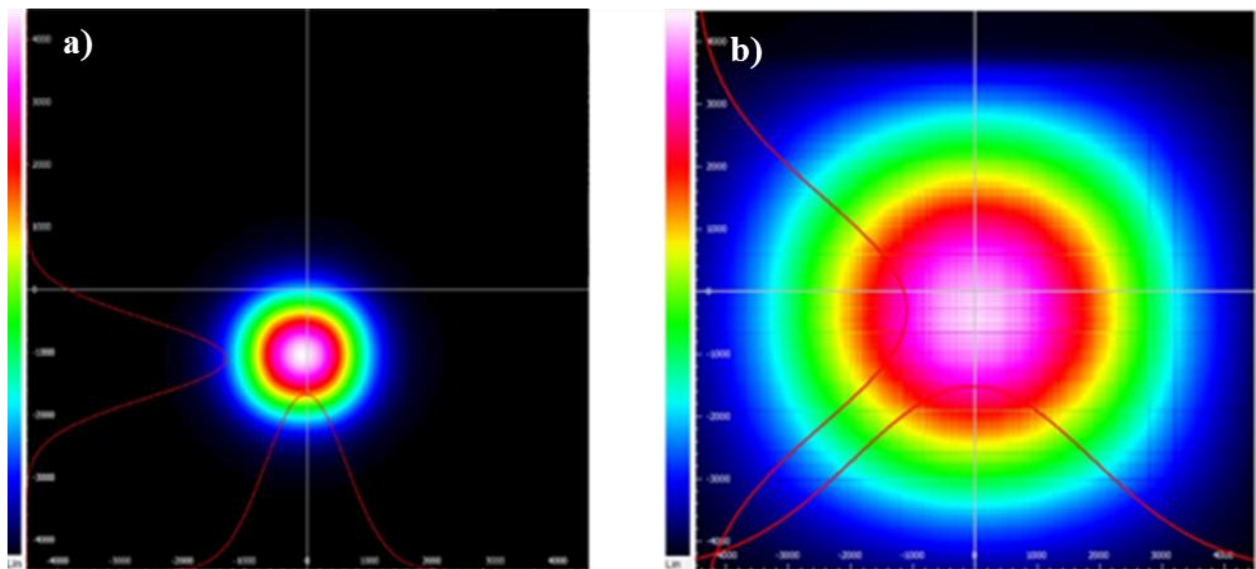

Figure 13. Beam profile before and after the beam expander: a) before beam expander and b) after beam expander

The power is transmitted through all the optics before objective is around 85.4 %. After widening the beam by using beam expander with adjustment of 4X, the beam diameter is increased up to 8 mm before the high power microscope focusing objective that has 1064 nm center wavelength, 20x magnification, 6 mm working distance with 10 mm effective focal length, 0.4 NA and 8 mm entrance aperture. Thus, the beam size is limited by entrance aperture.

Alignment of the beam is one of the most challenging steps for the optics. Dealing with near infrared laser is especially difficult to align due to invisibility with naked eye. To this respect, infrared detectors and viewing cards are used to align the beam. Mirrors and kinetic mounts are

added to control and align the beam in more effective and a simple way. The beam is aligned and the optics are placed accordingly as shown in Figure 9.

The beam enters the high power ND-YAG focusing objective from Thorlabs after following a couple of mirrors. The focusing objective is mounted on an Aerotech single axis linear direct drive nanopositioning z stage. Though two different objectives (20x and 10x) are engaged for our experiments, 20x objective has been prioritized for its tight focusing in line with main purpose of the test. Before placing the objective lens, the beam is straightened along the z axis. After the beam is aligned on z axis, the objective lens is placed on z stage and flattening is controlled by inclinometer. The objective is centered to the beam path by adjusting the 5 axis kinetic mount attached to the objective. The alignment is checked on infrared detector which can stands for high power and reflects visible light as seen in Figure 14. The airy disk patterns are checked for alignment. The fine tuning is performed inside fused silica by defining the minimum threshold laser power for visible inspection and small and slow adjustment of the objective kinetic mounts.

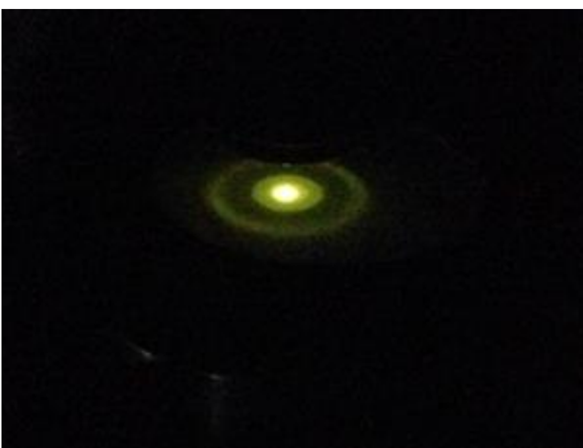

Figure 14. Focused beam on NIR detector and formed airy disk patterns

The beam diameter and corresponding focusing value is changed to understand the threshold pulse energy or the power inside the fused silica. In the initial experiments the beam is 3.8 mm in diameter that corresponds to nearly 4 μm spot size in the sample. The deviation between the beam spot size and x and y plane causes beam astigmatism which affects the focusing and polarization results due to not homogenous focusing. When the beam is expanded to 8 mm, the spot size is calculated nearly 2 μm. This change in the spot size affects the threshold power and the optimization setup significantly. 4X Expanded beam is determined to be used for further experiments. The spot size can be calculated with the equation below:

$$d = \frac{2\lambda M^2 f}{\pi w_{lens}}$$

where d is spot size, λ is wavelength, M^2 is beam quality factor, f is focal length, w_{lens} is beam diameter on objective. Because the beam dimeter is little over the objective entrance aperture (8 mm), the maximum beam size is expected as 8 mm.

The beam is focused on the sample which is placed on a vacuum-assisted sample holder mechanically designed and manufactured according to our specifications. The fixture has an opening at the center which holds the sample from the bottom part. The sample is located at the center so that it not only provides better holding position at high speed stage movements, but also leaves empty zone for laser micromachining of the bottom. The focused spot can be moved in z direction, and the location of top and bottom surfaces of the sample can be specified. Flatness of the sample can be adjusted via laser focusing and using pitch and yaw axis stages. The sample and the holder are mounted on a manual pitch and yaw axis stage on the top of Aerotech XY two axis direct drive nanopositioning stage. The accuracy of the X, Y and Z stage is ± 250 nm with a reservation of 1 nm. The accuracy and stage performance are crucial to successful for the

application. The stage acceleration and reaching to the desired speed takes time and requires some distance. For the process goal and consistency, the acceleration of the stage is kept maximum. The required distance for stage to reach the desired speed is shown in Figure 15.

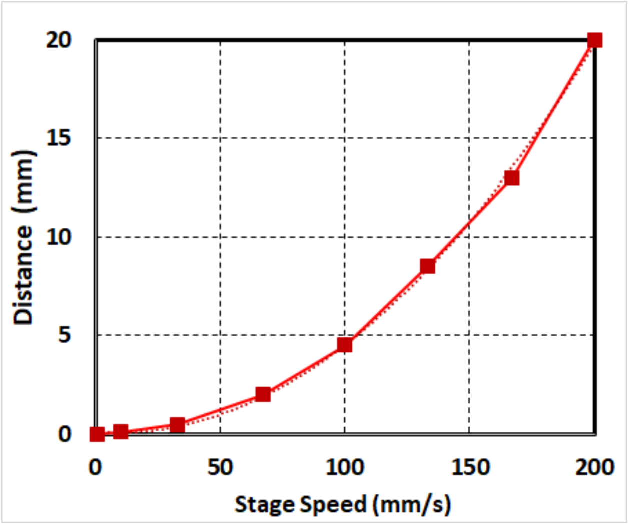

Figure 15. Required distance for stage speed up

2.2 Fs Laser Direct Writing Technique

Direct writing in transparent materials by femtosecond laser is a promising and rewarding technique enabling complex three-dimensional precise micro fabrication. This technique, known also as femtosecond micromachining, can be summarized as permanent multiphoton modification in glass and it has been a center of interest and studied by many regarding nanogratings formation and refractive index change. It is shown to be ideal for rapid production of passive and active micro devices like waveguides.[43] The greatest advantage of direct writing technique over the conventional methods is that it offers the possibility of writing complex 3D structures directly on

the contrary to other methods only allowing for planar geometries. Moreover, this method is simple, adaptable, scalable and cost effective.[44]

Local modification inside the fused silica is induced with the locally deposited energy when the laser pulses are focused tightly inside the sample. The focused laser pulse carries a great number of photons in a small volume and in a short time. Thus, nonlinear interaction of light with materials becomes possible. Energy can be deposited with the combination of multiphoton, tunneling and avalanche ionization.[15] The nonlinear absorption happens only in the focal volume and it could be sub micrometer size for tight focusing.

Fs lasers cause different types of modifications in the material with processing speed. A refractive index change occurs with low influence, produced by individual pulses. Nanogratings are formed in the material with higher influence, produced by successive pulses. The time between pulses is shorter than thermal diffusion time, thus heat accumulates in the focal volume.[45] Nanogratings could be utilized in fabricating optical elements and microfluidic channels. For light pipes, chemical etching is required after the fused silica is irradiated in the desired shape to remove the irradiated part. Direct writing technique was successfully tested as a starting point.

Figure 16 demonstrates that this technique enables complex pattern writing as well as control of the power and speed. Some of the important parameters for direct writing are laser pulse repetition rate, stage speed, spot size and pulse energy.

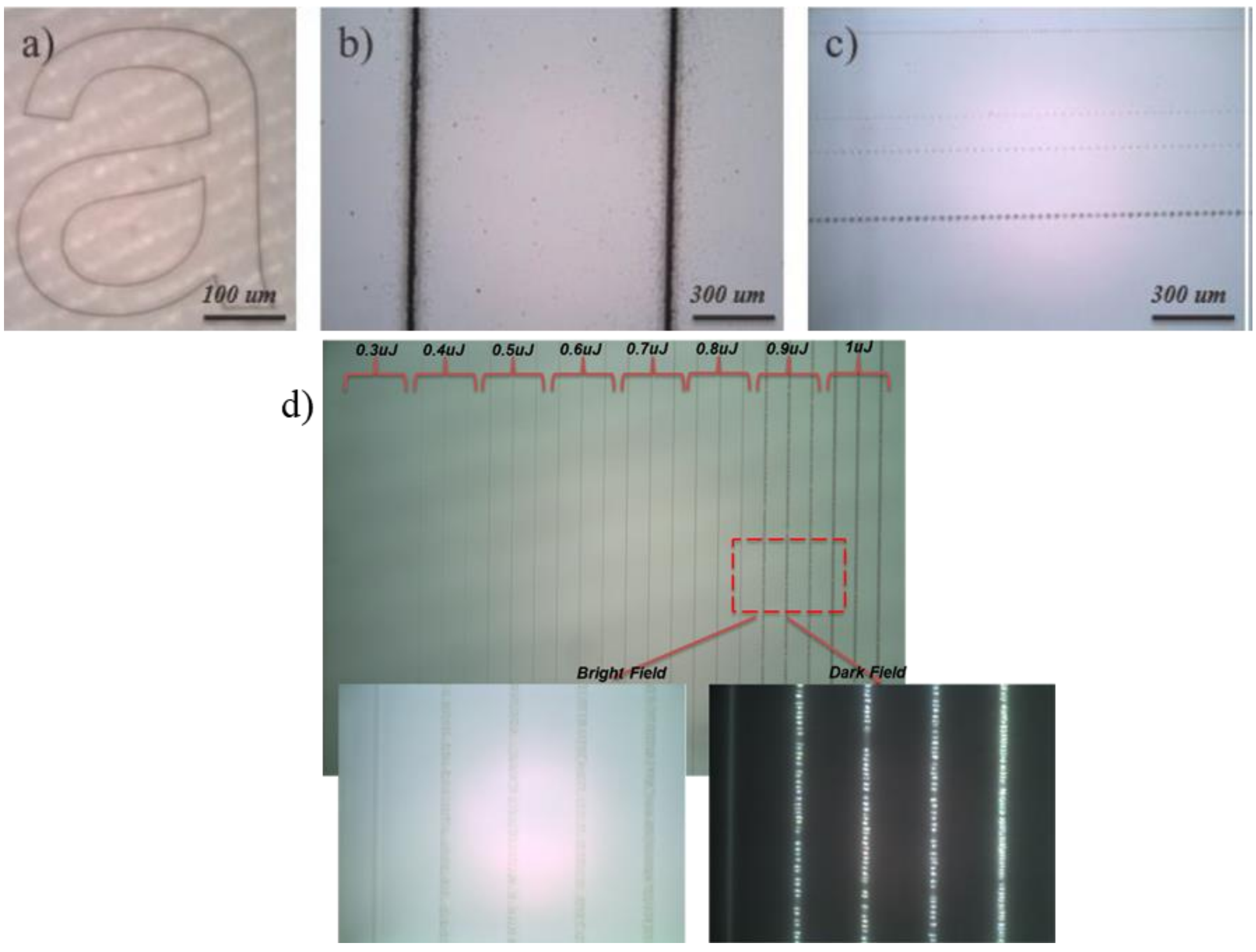

Figure 16. Direct writing images: a) complex writing inside silica, b) powerful writing on the surface, c) pulse shots inside of silica sample at low PRR and high scan speed, d) bright and dark field images of birefringent effect of nanogratings resulting from fs laser irradiation.

2.3 FLICE Basic Process for Fused Silica

The femtosecond laser irradiation and chemical etching (FLICE) process is a novel microfabrication technique and has gained popularity as it has the ability of fabricating 3D structures with high aspect ratios. It is a simple and maskless technology and it has a great potential for rapid prototyping. The process has two step: femtosecond irradiation on transparent material and wet chemical etching for removing laser affected zone (shown in Figure 17).[16, 46-49] It is

scalable, affordable and suitable for high volume industrial optical component production. Laser wavelength, pulse width, power, repetition rate, stage speed, lens numerical aperture and etchant type, concentration and condition are the key factors of the process.

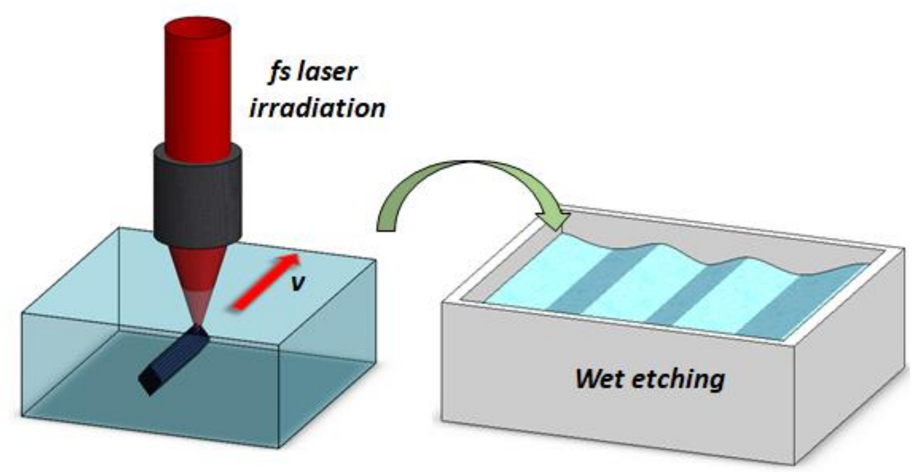

Figure 17. Femtosecond laser irradiation followed by chemical etching (FLICE)

For 1D selectivity etch studies, 1 mm thick, 25×25 mm^2 UV grade high purity fused silica are used. Various pulse energy and translation speeds are used for optimizing the 1d selective and 2d selective etching studies. Following the direct wiring scans, the sample is dipped into KOH solution which is prepared in a plastic beaker placed on the hot plate at 85°C, and a stirrer at 75 rpm stirring speed is placed to induce fluid flow inside the beaker.

2.4 Etching Selectivity Studies

Wet chemical etching is the process of etching solid materials in an aqueous chemical solution. The whole substrate, fused silica sample in our case, is dipped into the solution. It is a very selective method as it can be stopped at a certain point [50] and it is an ideal method as it

enables high selectivity, a controllable etch rate and a planar etching surface. [51] However, exposure time should be controlled as the lateral etching may continue. There are many parameters that affect the etching rate and selectivity such as pulse energy, pulse repetition rate, scan speed, polarization of the beam, temperature, and other environmental effects. The most significant factor is the molecular chemistry between the glass and etchant.[28]

Among the 3 types of modification zones, only Type 2 modification zone is applicable to selectively wet etch. [27] The underlying reason for this selective etch zone, the enhanced etching rate in the laser irradiated parts is still under investigation. There are two strong possibilities: bond angle change of Si-O or the etchant diffusion through the nanogratings.[52] The etching efficiency depends on many parameters like pulse width, polarization, pulse energy, writing speed, focusing lens specs and etchant type, concentration and condition. There are several studies that discuss the polarization impact on the etching selectivity which states that laser scanning should be applied along the polarization direction to achieve a better selectivity.[53, 54]

The nanogratings region helps the etchant penetrate through the modified region. Etchant diffusion and the etched bay product is vital for etching selectivity studies. The fused silica etching actualizes once the etchant is diffused in the modified region. The selectively etching process is not through selectively etching of modified and non-modified etching process, it is rather the diffusion of etchant through the cracks. Hence, the etching speed is strongly related to the diffusion process and confinement. Diffusion mechanism of etchant and product at high aspect ratio confined structures should be further investigated. Since the etching process happens at all sidewalls of nanocracks, concentration over time and place should be taken into account utilizing Fick's law. Concentration of acids and product over depth is another point to be considered. In

nano-scale regimes, some other effects like effective diffusion coefficient, surface charge effect, Debye length, electro kinetics, Dukhin number and viscosity of the solutions should be studied intensively to understand the etching in confined areas. The steady state and non-steady state diffusion equations are as following:

$$J = -D\frac{dC}{dx}$$

$$\frac{dC}{dt} = D\frac{d^2C}{dx^2}$$

where J is flux, D is diffusion coefficient, C is concentration.

Selectivity is the ratio between etch rate of modified and unmodified materials. There are two well-known etchants, and one is HF and the other one is KOH. Both of these etchants has advantages and disadvantages. While HF acid has high etching rate and low selectivity, KOH solution has low etching rate, high selectivity, less toxic and easier to handle according to safety perspective.[55-57] To understand the etching effect, 1D laser line irradiation inside the fused silica is selectively etched and the etched channel length and bare silica etching rate is compared to calculate the selectivity experiments. To understand the etching efficiency, selectivity is an important parameter. Selectivity is basically the ratio of etching rates of modified region vs non modified region, which can be calculated with the following equation:

$$S = (r_s + r_0)/r_0$$

where S is selectivity, r_s is etch rate on modified region, r_0 is etch rate on non-modified region or bare silica. In 1d selective etching condition the laser irradiated sample is placed inside the etchant and the 1D modified channel etch length is measured hourly manner under the microscope. To understand the bare silica etch rate, the silica plate thickness is measured over time. Silica plate

thickness shrinks with top and bottom surface by etching which is similar to 1D channel side etching and the measurements closely match with both cases.

In this study, we will analyze the one dimensional and two dimensional etching in fused silica by adjusting the parameters.

$$SIO_2 + 2KOH = K_2SIO_3 + H_2O$$

$$SiO_2 + 6HF \rightarrow H_2SiF_6 + 2H_2O$$

As a result, 5 % to 45 % weight/weight percentage (w/w) KOH solution at 85°C with 75 rpm stirring speed is chosen for the optimization. KOH solution is prepared from pellets dissolved in deionized water (DIW). To prepare 5 % w/w KOH solution, 5gr KOH pellets dissolved in 100ml of its solution. 1D direct writing methods is applied on a silica plate under 300 µm beneath the top surface at same condition like same speed, pulse energy, polarization and direction. Later the silica plate is diced with precise dicing saw machine at same condition. Thus, we get many identical irradiated silica pieces for comparing the etching selectivity studies. In 1D channel etching, the modified and non-modified region etching is measured hourly fashion under microscope. As the solution percentage increasing, the selectivity is decreasing in time as seen in Figure 18. 5 % KOH solution is chosen for further experiments as it has best selectivity over time.

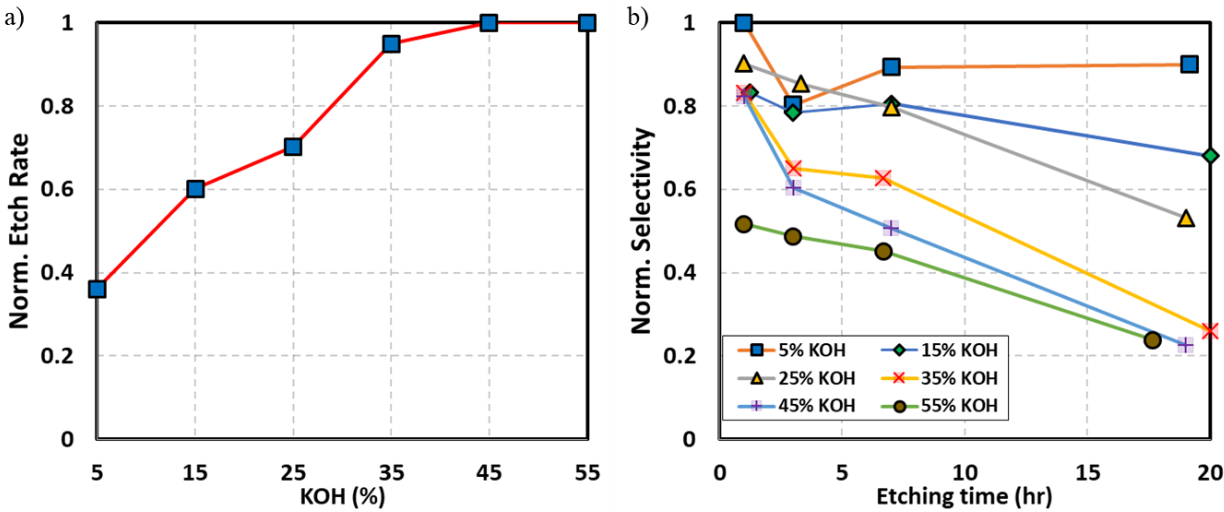

Figure 18. a) Normalized etch rate over KOH concentration, b) 1D selectivity over time with various KOH etchant

The importance of high chemical purity and resistance of various silica samples is investigated. Non-laser irradiated, polished, original silica surfaces after wet etching with different purity level silica are presented in the following microscope images. (Figure 19) The importance of material selection comes to the fore with the fact that the not pure samples generate scratch and digs on their original surfaces after etching process. The best quality surface after wet etching is observed on the surface of Corning fused silica.

Figure 19. Three different silica samples with different purity level and after etching process: a) Corning 7980 fused silica, b) Ted Pella GE124, and c) unknown (Ebay) JGS1

As per sample purity, the materials inside the silica will affect focusing irradiation and etching negatively if the sample is not pure. The high purity quartz meaning that the sample has SiO_2 content of >99.995 %. In general, it is hard to find a pure sample; however, this will not be a huge problem for laser irradiation as long as the size of the particle is small enough.

2.4.1 Dimensional Control

The plasma generation at the focal spot of the laser beam and precision stages are used to adjust the sample flatness. It is possible to find the surface location at given spot with an accuracy less than 10 µm. 25 mm by 25 mm square silica sample is flattened on the holder with an angle of ≤0.023°, which is nearly ignorable. This tolerance depends on the sample dimensions as well: Longer sample means lower error.

Etchant starts to penetrate and etch from top and bottom of the sample. Due to the challenges of diffusion and selectivity, it takes time for the etchant to reach the center of the irradiated 2D surface. This nature of the etching process causes some surface deformation such as bump and dip shaped 2D sidewall surface profiles and some releasing issues. After releasing, the

sidewall angle should be taken into the account, which is not ignorable especially with low selectivity etchants. However, selectivity of KOH is high enough to obtain a bump smaller than 10 µm even flat surface.

High selective etching provides smaller scribe width which is used for separating one coupler from the side waveguide as shown in Figure 20a. Having observed at the end of the experiments, nearly 35 µm width is achieved as shown in Figure 20c. The sample width is adjusted for 1 mm, after etching process the sample width is measured ~0.965 mm.

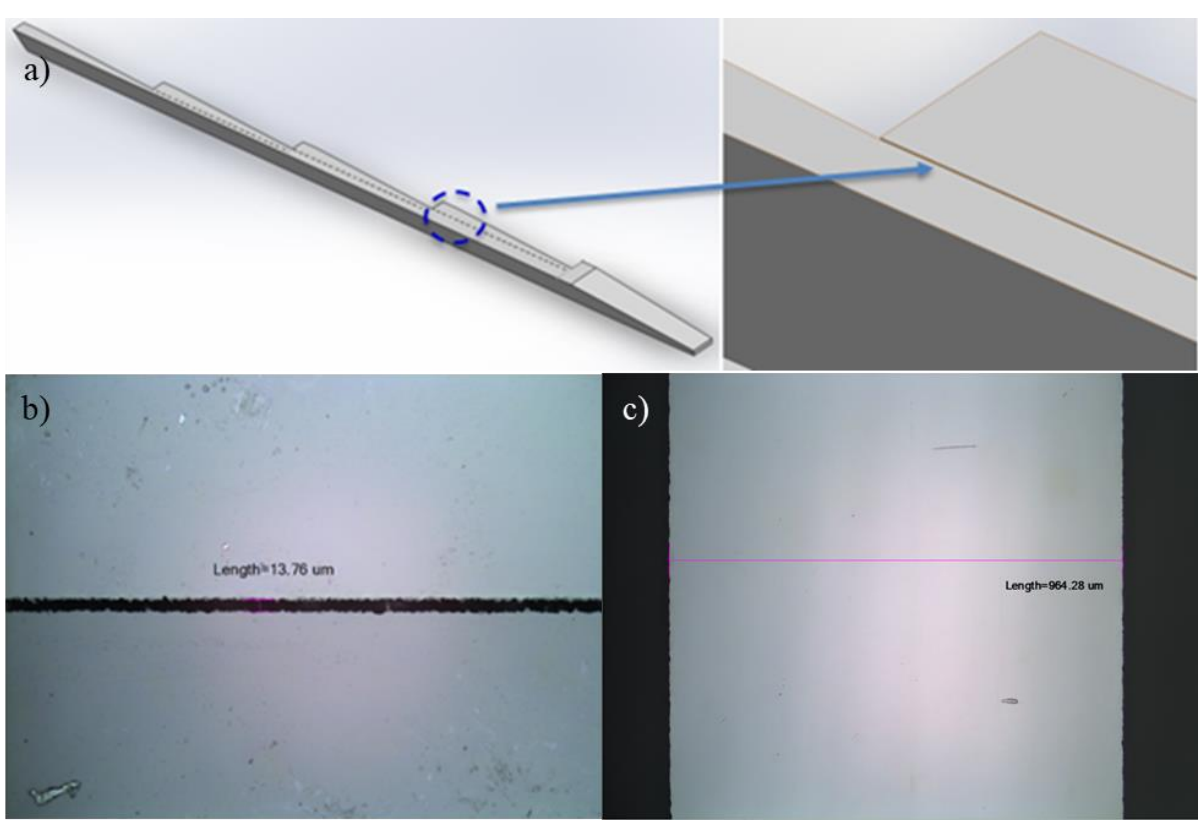

Figure 20. a) 1000x 1*5 staggered waveguide design for prototype with separation gap b) laser scribe width during etching c) sample width after etching process

For a homogenous etching rate from top and bottom of the sample, the irradiated sample is placed on a small part of silica piece to give enough height to etchant to react well with both sides. Same etching speed at the top and bottom of the sample is expected in this case.

2.4.2 Release Issues

Releasing the irradiated part from the sample is one of the key process for getting high quality surfaces. Etching occurs in both directions in a 2D laser irradiated plane if we ignore the non-irradiated etching. Thus, etching is expected to occur only in x-z or y-z plane. Z direction etching is one of the key step as the etching goes in z plane and the center of the sample is the most critical part for releasing. For the etchant to move in both directions, the last etching area will be the center of the sample and if the sample is not placed correctly, the sample will break at that location and there will be some residual parts stuck on the surface. The sample should be supported from the bottom to prevent cracks.

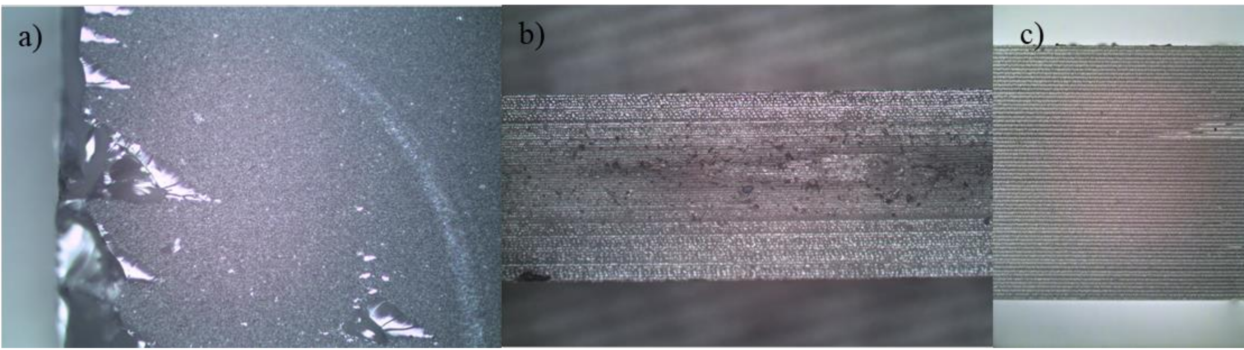

Figure 21. a) Cracks at sample edges, b-c) center irradiation and etching problems

We could mention about some possible challenges for laser irradiation. One of the challenges is irradiation at the edge of the sample. When the laser beam is moved from outside of

the sample to the inside, at the edge the sample, a non-uniform irradiated zone is observed, and this zone is not etched as shown in Figure 21a. The reason for this phenomenon is the laser beam focusing. At the edge of the sample, the half of the beam focuses inside of the glass while the outside part of the beam focuses on a different location. As a result, the beam will not correctly focus on a spot and not irradiate the edge portion correctly. Another challenge is laser parameters that if the laser parameters are chosen not properly, the required time to etchant reach the center portion of the irradiated zone takes longer and even not able to reach the whole surface. Cracking in the sample is even possible to happen with gravity force as shown in Figure 21b-c. The sample should be supported from the bottom part and possibly more etching time is required to release structures to make sure the sample is etched uniformly. One should keep in mind that laser parameters have a strong effect on the releasing process which will be discuss in detail in the Chapter 3.

2.5 Surface Metrology

There are many metrology tools such as SEM, AFM, stylus profiler, and white light interferometry to analyze and understand the surface characteristics of the sample. While AFM has highest lateral resolution,[58] optical profiler has larger vertical sizes as shown in Figure 22. Although the stylus profiler has 3D scan options, they are very slow when we compared to optical profilers and very sensitive to stylus tip. Stylus profiler is eliminated as an option as time is a significant factor.

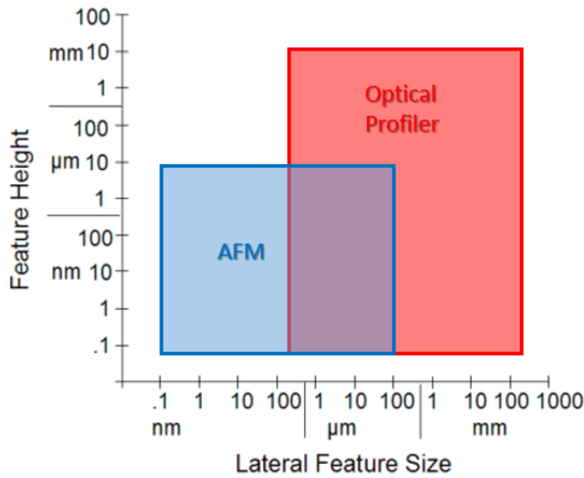

Figure 22. AFM vs optical profiler feature sizes and resolution

Precision, accuracy and resolution of the measurements are influenced with various factors such as scan speed, wavelength, field of view, processing algorithms, sample properties like slope, feature, roughness and environment like temperature, noise and vibration. Optical systems are limited by optics and camera resolution while AFM and stylus are limited with their tip sizes. In metrology tools accurate, precise and high resolution is important for getting a good data. In low magnification optical profilers, the resolution is mostly limited by detector or camera resolution. But when magnification increases, the limitation goes to optical systems. When the spacing (d) between the objects or features in imaging area is greater than 0.6λ/NA, this is detector limited, and when the spacing is smaller than 0.6λ/NA, this is optics limited. There are some parameters which is important for our optical profiler measurements like roughness, heights, curvature, width, defects, and structure size. We aim to achieve the highest lateral and vertical resolution with dominant spatial frequency of the surface in the course of taking measurements.

White light interferometry uses a white light source and divides the beam into two via beam splitter, then combine them back to make an interference pattern.[59] This pattern is used to determine the difference in path. In flat surface the spacing of the fringes is ½ of the wavelength of the light. Vertical scanning interferometry (VSI) measures the separation between two fringes while moving over z direction. Noise level is nm level and could be too high for very flat surfaces. Phase shifting interferometry (PSI), on the other hand, has a noise level of less than nm. Psi uses a monochromatic light and calculates the phase of the fringes and has <<1 nm vertical resolution as a result.

Surface texture composed of various phases of spatial frequencies which are named as roughness, waviness and form as shown in Figure 8. Form has lower spatial frequencies while the micro roughness has higher spatial frequencies. To see the actual surface profile, various cut off filters can be applied in accordance with the limitations of the tools. Short cut off is generally used to eliminate the noise on the measured surface, and the long cut off filtering is used to distinguish micro roughness from surface form or waviness. Filtering means excluding the wavelengths below or above the specified filtering wavelength. We have determined to use 0.08 mm as cut off wavelength in line with the recommended sampling distances and cut off wavelengths by ISO 4288.

3. FLICE PROCESS PARAMETERS VS TRADEOFF

The main goal of this chapter is to optimize all parameters affecting the surface quality of the sample process with FLICE, and represent the ways to overcome the challenges. To optimize the process parameters, formation of nanograting is studied first. This chapter starts with the parameters effect on nanograting formation such as polarization, writing speed or corresponding number of overlapped pulses and pulse energy as the importance of nanograting on selective etching is discussed in previous chapter. The direct writing experiments is performed 300 µm beneath the top silica plate with 50 µm separated varying parameters of raster scans as shown in Figure 23.

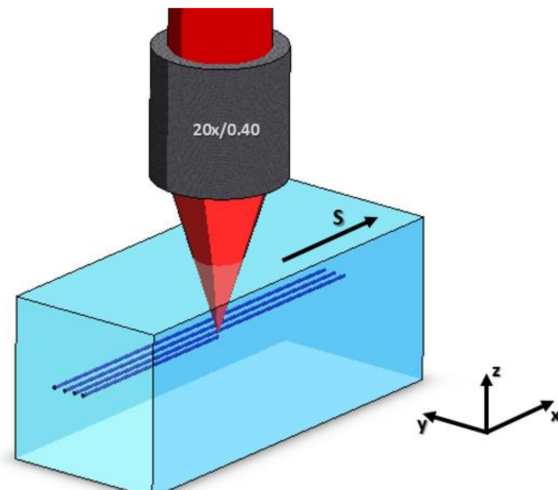

Figure 23. The proposed direct writing process for nanograting analysis

A good etching is strongly related to the arrangement of nanogratings. The optimum surface quality and etch-rate selectivity can be achieved by controlling the arrangement of nanogratings that form within the inscribed region for a specific window of parameters.

3.1 Nanogratings

Short pulse laser interaction with silica glass through nonlinear absorption generates plasma via multiphoton ionization regimes which is called Type 2 regimes as previously mentioned. These formed nanoplasmas in the dielectric substrate creates structural change in material. Optical intensity is required to be a little over the threshold to form nanograting. After laser direct writing technique is applied 300 μm beneath the top silica sample, the sample is diced through the perpendicular direction to laser writing direction for cross sectional analysis the modified zone shown in Figure 23. The diced surface is then finely polished by using lapping machine. The lapped surface is placed into 0.5 % HF for 2 min, afterwards. The modified zone is scanned and investigated under SEM. Figure 24 shows the formed nano-scale cracks in the modified zone with the laser beam perpendicular polarized to writing direction. The spacing between the nanograting is shown as Δ. The beam duration is adjusted to 300fs, the pulse energy is specified as 0.4 μJ, and the stage speed and pulse repetition rate is configured accordingly to get the desired overlapped number of pulses.

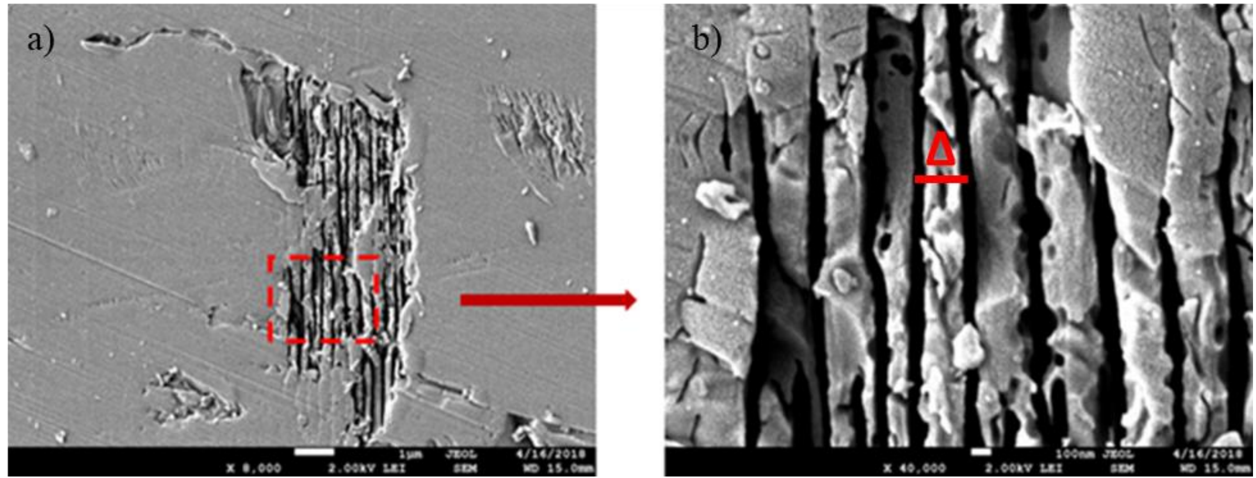

Figure 24. Cross section SEM images: Perpendicular polarization with 0.4 µJ with 300fs and N=3333. a) at low magnification (8K scale is 1 µm), b) at high magnification (40K scale is 100 nm),

To understand the laser parameters effect on nanogratings; laser wavelength, pulse energy, repetition rate, polarization, scan speed, number of overlapped pulses are varied and the above mentioned process is repeated for imaging.

3.1.1 Polarization Effect on Nanogratings

The polarization is adjusted manually by using wave plate optics and rotation stage. Direction of the polarization is precisely checked with polarizer and power meter. The half wave plate is used to change the direction of the linear polarized beam, the quarter wave plate turns the linear polarized light into circularly polarized light. The directions of electric field or polarization and nanogratings are perpendicular to each other. When the polarization is perpendicular to the writing direction, nanograting lines and spacing are observed along the writing direction. The circular, perpendicular and parallel polarized beam effect on nanograting is represented in Figure 25.

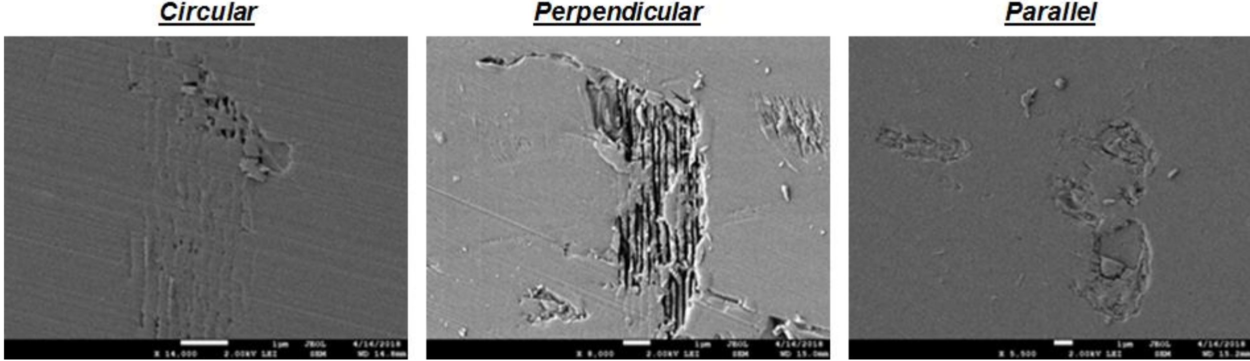

Figure 25. Cross section SEM images: 300fs, the circular perpendicular and parallel polarization SEM images

The difference in the directions of nanogratings in the perpendicular and parallel polarization is clearly visible. For circular polarization, the direction of nanograting is different from the others. For imaging circular polarization, the image taken from top side of the sample will be more helpful. However, the image in Figure 25 showing the circular polarization gives us a clue to make the interpretation that the direction of nanogratings should be a mixture of the nanogratings formed by other linear polarized beams.

3.1.2 Number of Overlapped Pulse Effect

One of the key parameters for nanograting formation is the writing speed. The number of overlapped pulses decreases if the writing speed increases for a given pulse repetition rate. The overlapped number of pulses can be calculated with the equation below:

$$N = PRR * d/v$$

where $N$is overlapped number of pulses, $PRR$is pulse repetition rate, d is spot size diameter, v is writing speed. The effect of N to nanogratings can be seen in the following SEM images. The irradiated regions have some deformation through the left side due to the lapping process.

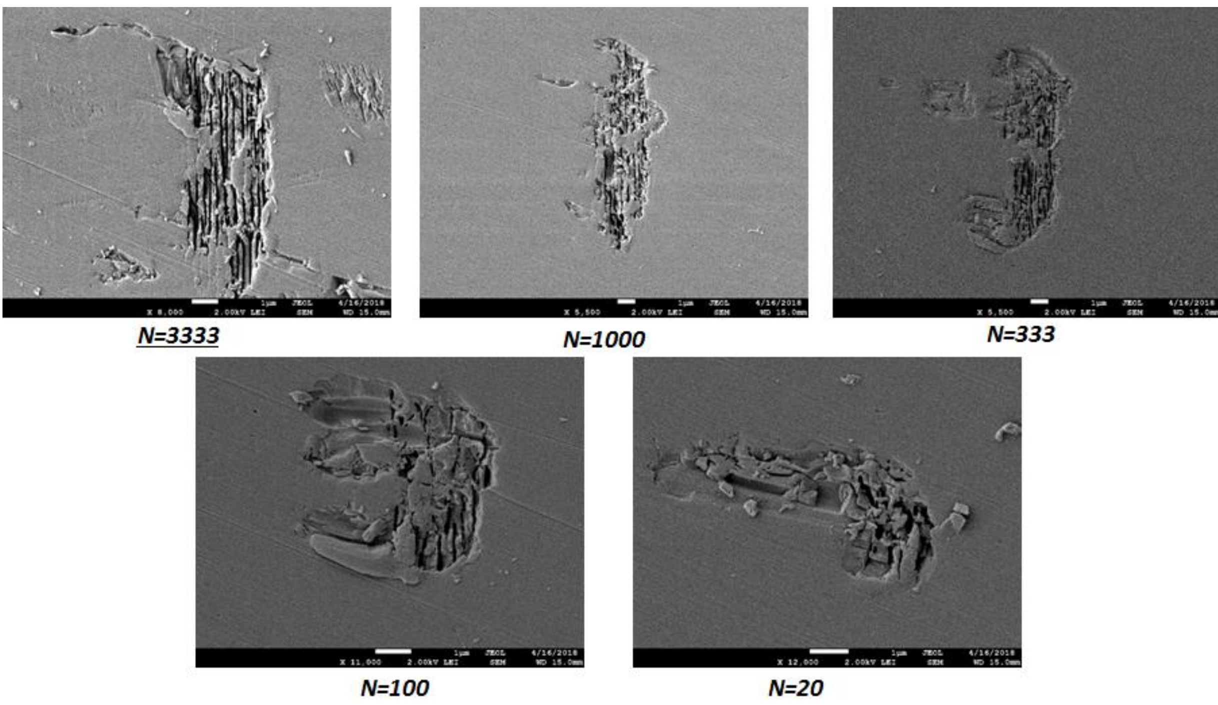

Figure 26. The number of overlapped pulse N effect for perpendicular (s) polarized light with pulse width of 300fs and pulse energy of 0.8 μJ.

When N increases, the number of nanograting and the lateral and vertical size of modified spot sizes increase while the spacing between the nanogratings decreases. All of this should improve the etch rate, but it is hard to understand the effect on the surface quality at this point.

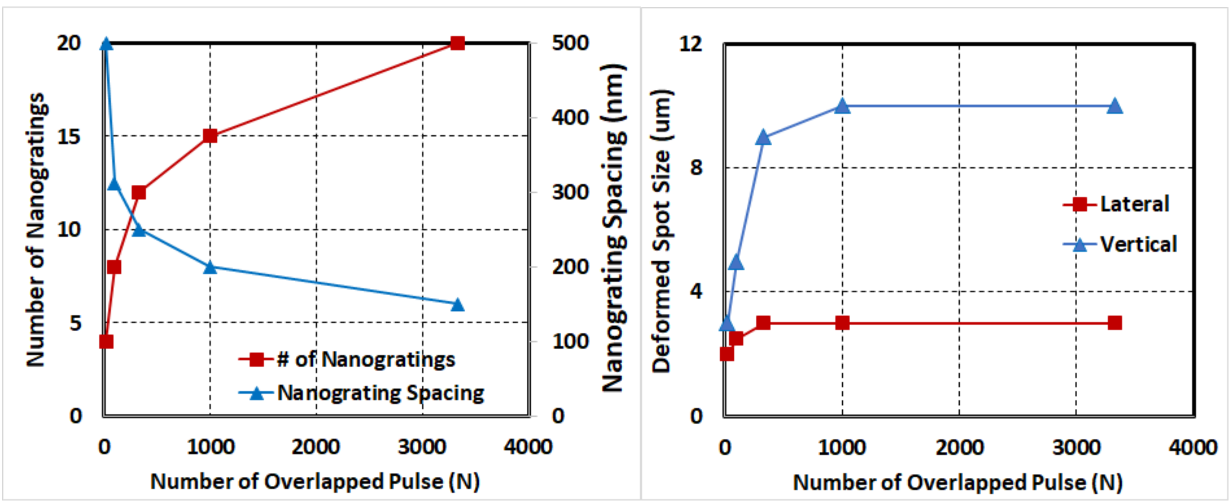

Figure 27. Effect of N to nanograting numbers and spacing between them and the laser irradiated region lateral and vertical dimensions for given N.

When N increases the number of nanograting is increased from a few nanogratings to around 20 nanogratings and the spacing between the nanogratings is decreased from around 500 nm to nearly 150 nm. We should note that the changing of these values are not linear. The changes are more critical while N is smaller than 1000. The size of modified region at beam spot is related to N as well. However, we should note that after N is greater than 333, the lateral and vertical modified zone stays nearly the same. According to Shimotsuma, the spacing between the gratings is decreased from 240 nm to 140 nm as the laser pulses are increased.[60]

3.1.3 Pulse Energy Effect on Nanogratings

Another important laser direct writing parameter affecting the nanograting formation is laser pulse energy. Pulse energy has a crucial effect on laser deformation regimes like Type 1, 2 and 3. Type 1 is refractive index change zone which requires pulse duration of less than 100fs. The laser pulse durations in this experiment has more than 300fs, thus the Type 1 regime is not observed in the experiment. Type 2 and 3 regimes are the main focus in our study. The formation of the

nanogratings are observed after the threshold pulse energy. The number of nanogratings increases and the deformed spot area gets larger when the pulse energy is higher. Micro explosions comes into existence when high pulse energy is used. The change of formation of nanograting and voids can be seen in Figure 28.

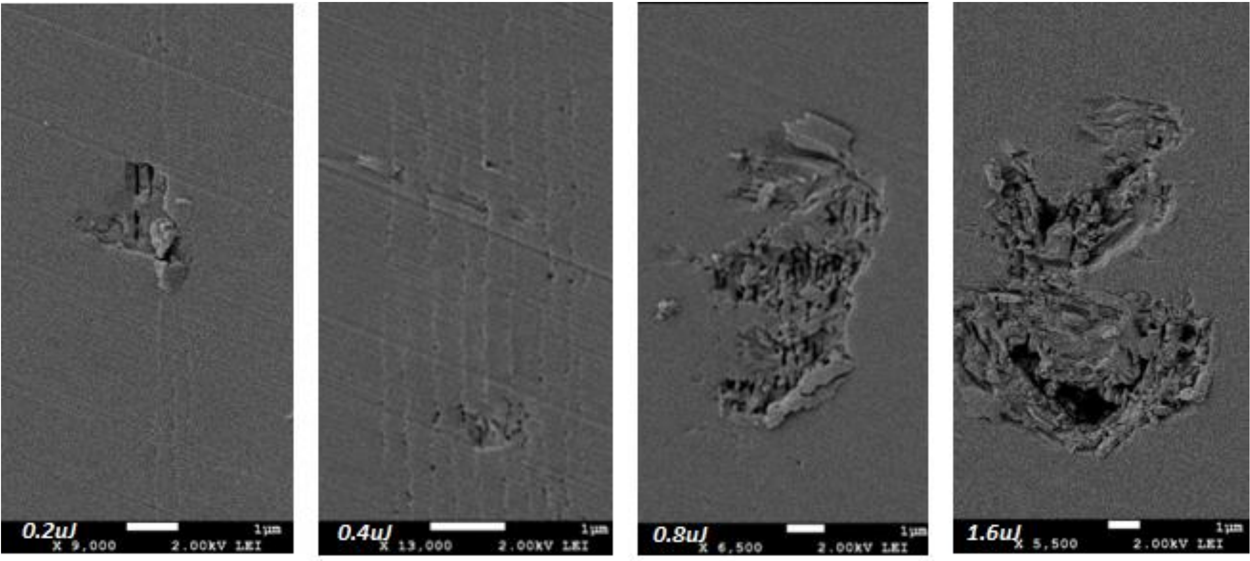

Figure 28 SEM images of modified spot with various pulse energies from 0.2 μJ to 1.6 μJ by perpendicular polarized beam which has pulse duration of 1000fs with 1000 overlapped number of pulses.

When the pulse energy is changed from 0.2 μJ to 0.8 μJ, the nanograting is increases from roughly from 5 to 15 while keeping the space between nanogratings nearly same as shown in Figure 29. According to Shimotsuma, when the laser pulse energy is increased from 1 μJ to 2.8 μJ, the spacing is changed from 180 nm to 320 nm.[60] This data doesn't match with our experiment. On the other hand, according to Sun, the spacing between the nanograting keeps

constant with the change in laser pulse energy from 170 nJ to 870 nJ which closely matches with our results.[61]

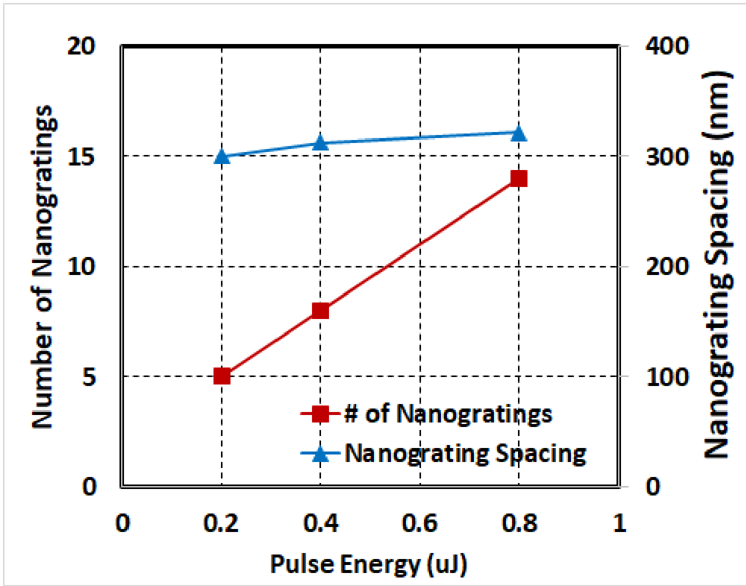

Figure 29. Pulse energy effect on nanograting number and spacing

3.2 Selective Etching

The nanograting formation and laser parameters are studied previously and the nanograting effect on selective etching is to be studied. All the parameters are aimed to be optimized. To lessen the parameters 1d selectivity test is executed at first. In this step, one directional modified channel is immersed into the etchant, and the etching distance is analyzed to examine the selectivity. The selectivity basically represents the modified channel etch rate divided by non-modified silica etching rate. The previously optimized etching concentration 5 % w/w KOH solution is chosen for

this study. The sample which has been applied direct writing with various laser parameters placed in the etchant at 85C at 75 rpm stirring speed and the etching rate is measured under microscope.

3.2.1 Pulse Width Effect

The pulse width is evaluated and tried to be optimized as the first step. To understand the pulse width effect, consecutive tests are conducted and it is evaluated how the etching is affected by pulse duration. Various conditions are tested for more accurate result; the pulse duration is measured with different pulse energies and overlapped number of pulses. It is found that the selectivity of the modified channel with pulse width of 1000fs is much better than 300fs pulse duration as shown in the Figure 30. The 1000 fs laser pulse giving higher selectivity with more broad energy and overlapped number of pulses range. The process is done with three different polarization results, but the perpendicular one is picked for simplifying the explanations.

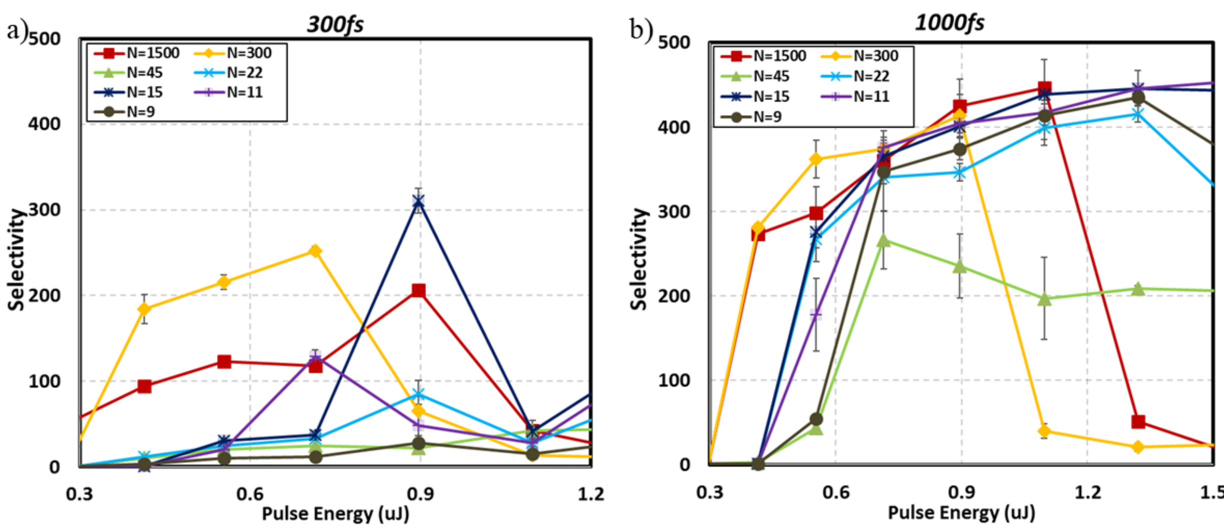

Figure 30. Pulse width affect at various condition on 1D channel selectivity a) for 300 fs, b) for 1000 fs

3.2.2 Polarization Effect on Selective Etching

Deciding the pulse duration as 1ps, the same experiment is conducted under a variety of polarization conditions. As expected from the nanograting data, the beam polarized perpendicular to the writing direction yields a better selectivity than the other two polarizations. As seen in Figure 31, the modified channel via perpendicularly polarized beam has much broader pulse energy and N ranges. In all three polarizations the selectivity is reached up to 500, however perpendicular polarization gives much broader range of both writing speed and pulse energy range. In parallel polarization, at the low writing speed or at high overlapped pulses, the channel doesn't etch and doesn't give any selectivity. In circular polarization case, the high speed and low overlapped number of pulses gives less selectivity which is opposite to the results at parallel polarization.

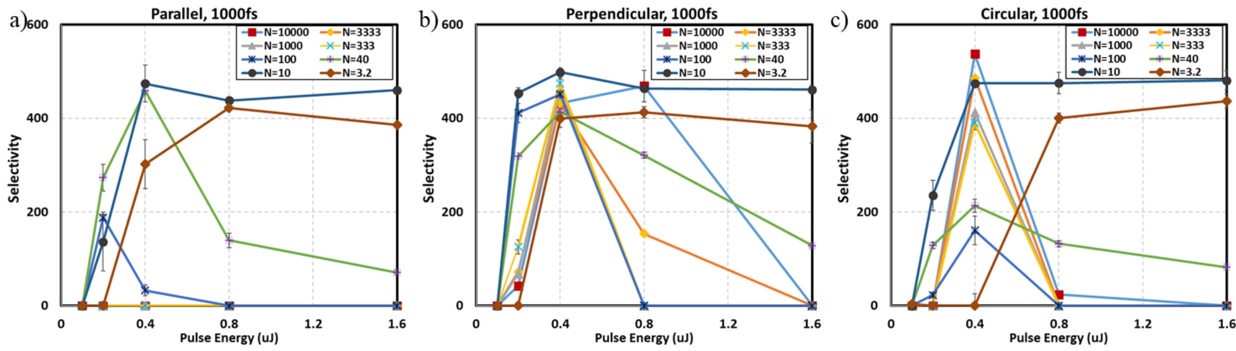

Figure 31. Polarization effect on selectivity with various channel writing conditions

The data gained from experiments reveals that the modified channel with parallel polarization and the low writing speed or high number of overlapped pulses doesn't etch while higher writing speeds results in good selectivity. Circular polarization and perpendicular polarization results seem nearly the same but perpendicular polarization has a broader pulse energy

range from 0.2 μJ to 0.8 μJ while the circular polarization is mainly localized at 0.4 μJ. It is interesting that the circular polarization with nearly 20 to 100 overlapped pulses has lower selectivity than the others. In conclusion, there are many sets of conditions that have high selectivity and could be a candidate for 2D plane surface etching studies. In overall the perpendicularly polarized and 0.4 μJ pulse energy has the best selectivity at the given number of overlapped pulses. The optical systems very sensitive to the alignment and these test result may change slightly according your alignment which definitely affects the focusing. It is observed that even there is small change selectivity with various tests, the general results show the same effects that we presented above.

3.3 Prototyped 2D Plane Etching

Following the 1D channel optimization, the 2D plane etching optimization is planned for analyzing the surface quality further. 2D etching refers that the laser modified region is not a line but a modified area on a plane. 2D plane is basically composed of a combination of 1D modified channels. The experiment is conducted with fs laser focusing on the bottom surface of the silica plate. Later the focus is moved 5 μm on z plane and the following xy plane is conducted. In this way the writing plane is moved from bottom to top. There are couple important writing rules that should be applied programing the systems. First of all, the laser spot size inside the silica sample should be considered whenever a change occurs in the pulse energy, stage speed, or pulse width lead change in the depth of focus. Another important rule is direct writing position on z plane. As we accept the laser beam coming on z axis, any modified zone prevents laser to penetrate down due to diffusion of laser at modified region. To prevent this effect the laser writing speed should start at the lowest z location and should be a step by step process. These steps are called as z

increments. The writing process is illuminated in Figure 32. The s refers to scanning direction. The writing condition consistency enables the comparable data between the experiments. Although there is small difference in power absorbed from top and bottom of the sample, the power along z axis is kept same to simplify the experiments executed with optimization purpose.

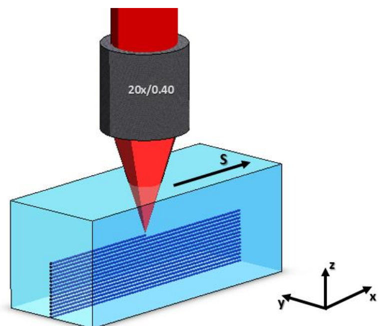

Figure 32. 2D plane writing direction with combination of multiple 1d writing from bottom to up with z increments

There are some circumstances to be careful about such as dwelling time, stage acceleration, and laser turn on and off, and coding for 3D step by step process. In the experiment the stage and laser are controlled by A3200 motion controller which enables controlling both laser and stage with G-code. To understand the 2D writings and etching, simple rectangular shapes are written with various laser parameters to analyze the surface quality and compare the parameters as shown in Figure 33.

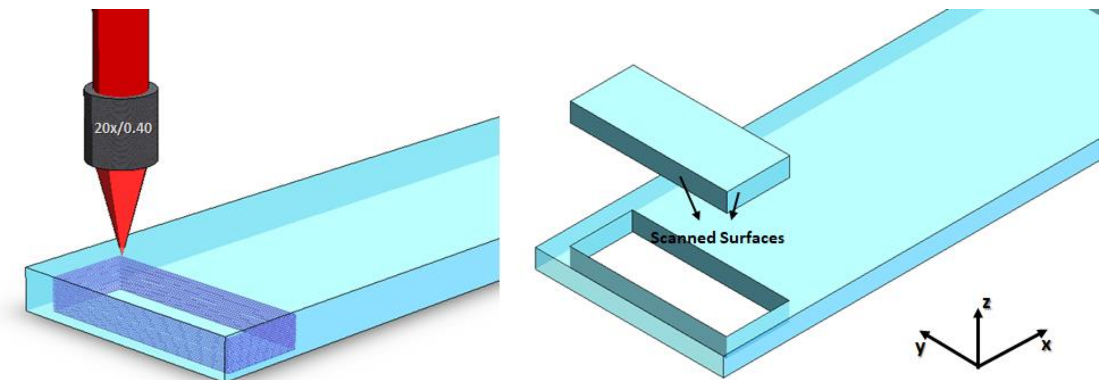

Figure 33. Laser irradiation and released material from 1 mm fused silica substrate after chemical etching.

The parameters are varying from polarization to writing speed or overlapped pulses with some other parameters. Firstly, the polarization is studied on the 2D scanned surfaces. The etched silica plate has a thickness of 1 mm. To evaluate the scanned surface shape and quality, WLI images are used which has an area a little bigger than 1 mm^2 covering the 1 mm thick of scanned surface. The images can be stitched together using the stitching tool in the profiler software and imaging the whole scanned surface becomes possible.

3.3.1 Polarization Effect

Proven with the 1D selectivity data, polarization is one of the key factors effective on surface quality. 3D optical surface profiler is used to evaluate the surface quality. RMS surface roughness is chosen without applying any filtering to reflect the surface form better. While Rq shows the root mean square average of the 2D surface profile, Sq is used for represent the RMS roughness of 3D surface. As we discussed previous chapters, surface consist of roughly three spatial wavelength regimes. The large wavelength indicated the waviness and form on the surface. The small wavelengths represent the micro roughness on the surface. After etching process, the

surfaces are changing dramatically for both wavelength zones according to the laser parameters. When the surface has some forms on the surface which increase the roughness significantly as the forms has high peak values. To distinguish the roughness values from real micro roughness, there is an industrial standard for surface roughness measurements. 80 µm Gaussian low pass filtering is one of the well-known and practical solution for this purpose. We demonstrate and compare both real surface roughness and filtered roughness data to understand the micro roughness and form of the profiles. Some of the optical profile images obtained from different polarization applied surfaces are shown in Figure 34.

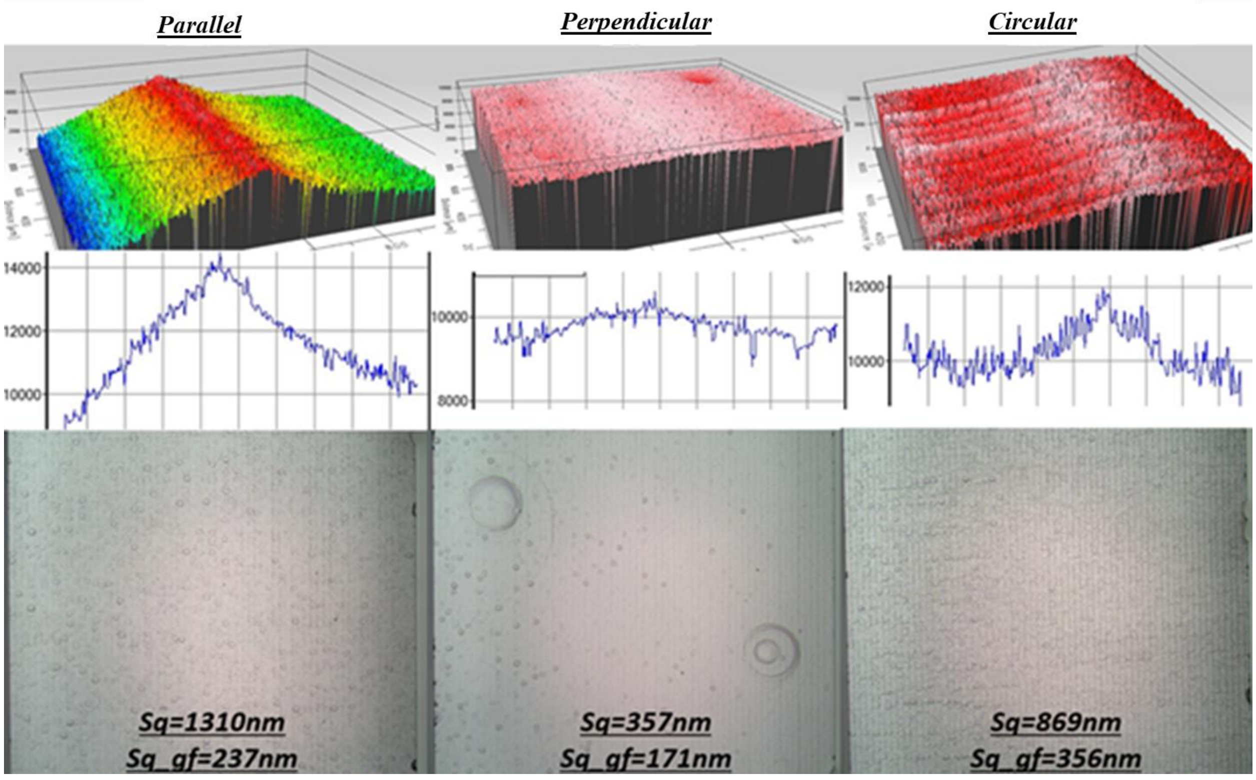

Figure 34. White light interferometry images, profiles and microscope images of the surfaces which are written at 1 mm/s and 0.4 µJ with parallel, perpendicular and circular polarizations, respectively

One can easily read from the polarization test graphics in Figure 34 that perpendicular polarization ends in the smallest roughness and hence the best quality with four different pulse energy and speed combinations. Parallel polarization on the other hand yields the worst results. The above data is just to show some surface profile images. The effect of polarization on surface is shown with other parameters in the following optimization results.

The Sq roughness is highest at parallel polarization which shows the highest form on the surface. There is nearly 5 µm bump on the surface which increase surface roughness. However; in circular polarization, there is 2 µm bump on the surface which shows less roughness than the one with parallel polarization. But, when the filtered roughness values compared, the circular polarization has higher micro roughness than the parallel. As the pulse energy decreases while penetrating through the glass, it is hard to say the sample surface getting same amount of energy at each location. The self-focusing also taken into account for better comparison. To simplify the parameters the pulse energy is fixed for the 2d writing process. It is also addressed that some surface deformation is observed in some condition at perpendicular polarization. The reason for this circular deformation is thought to be the silica sample purity. It is also interesting that the circular deformation is visible seen at closer area to the both top and bottom surfaces.

3.3.2 Pulse Energy Effect

The surface roughness change is minimal with pulse energy in s polarization, though it is critical for circular polarization. The results of some chosen parameters are shown in Figure 35.

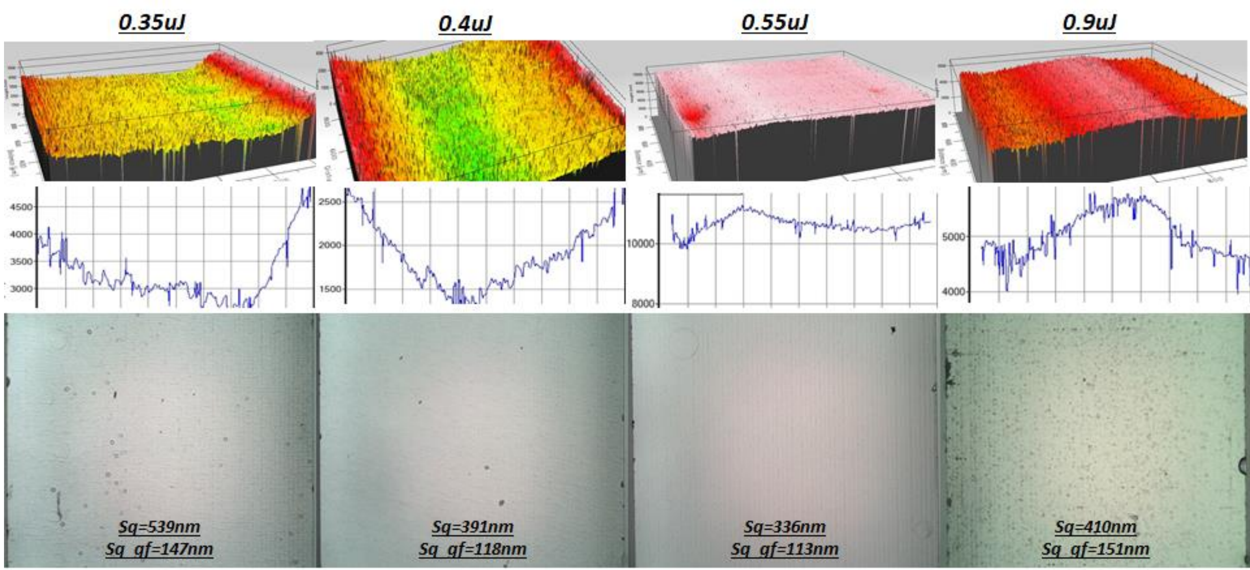

Figure 35. Surface profiles which are written in perpendicular polarization with various pulse energy

Evident from these results, the surface profile changes from v shape to inverse v shape only with the change in pulse energy. The right or left side of the sample could give us this this surface shape difference. Even if the surface profile seems 1 or 2 μm which leads to 200 nm RMS roughness increase, with different polarizations, this change could cause a dramatic effect.

3.3.3 Overlapped Number of Pulses

Speed effect should be taken into account in improving the surface quality. The surface RMS change seems minimal in s polarization while a great impact is observed with speed in parallel and circular polarizations. The roughness change in perpendicular polarization with writing speed is shown in Figure 36.

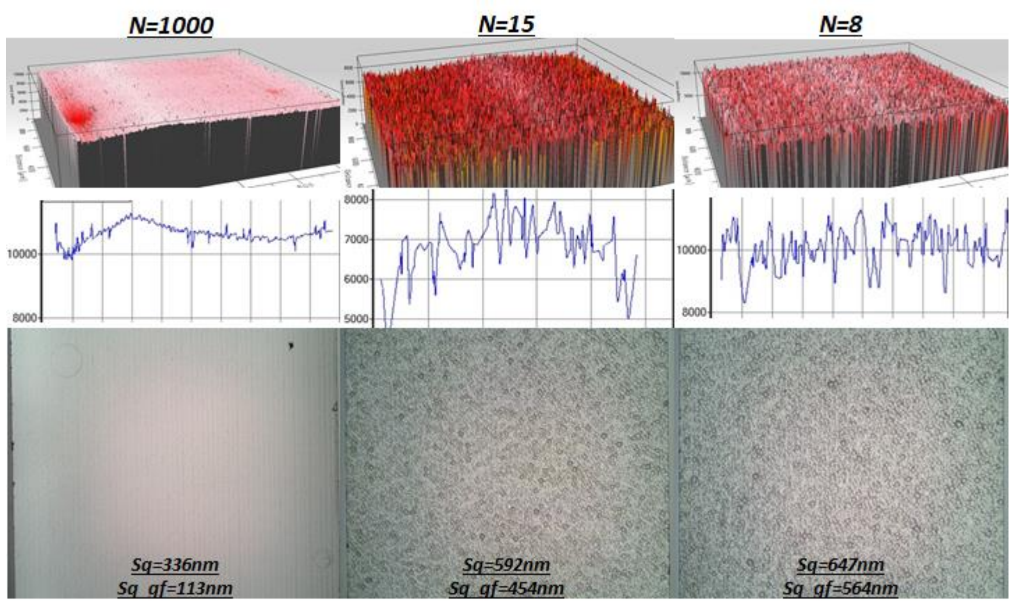

Figure 36. Surfaces which are written in perpendicular polarization at 0.55 μJ pulse energy with various writing speeds

As seen in above graphs, not only the surface shape but also the Gaussian filtered RMS roughness shifts over the speeds. Roughness gets worse as the speed increases which is explained due to nanograting lengths and numbers. This change is minimal in perpendicular polarization, while there are huge changes in parallel and circular polarizations.

3.3.4 2D Optimized Results

The optimization experiment is conducted with pulse energy of 0.4 μJ and the z increment is adjusted to 10 μm in air which corresponds to 15 μm depth in silica plate due to the refractive index of the material. The microscope images of the scanned surface with various writing condition is shown in Figure 37.

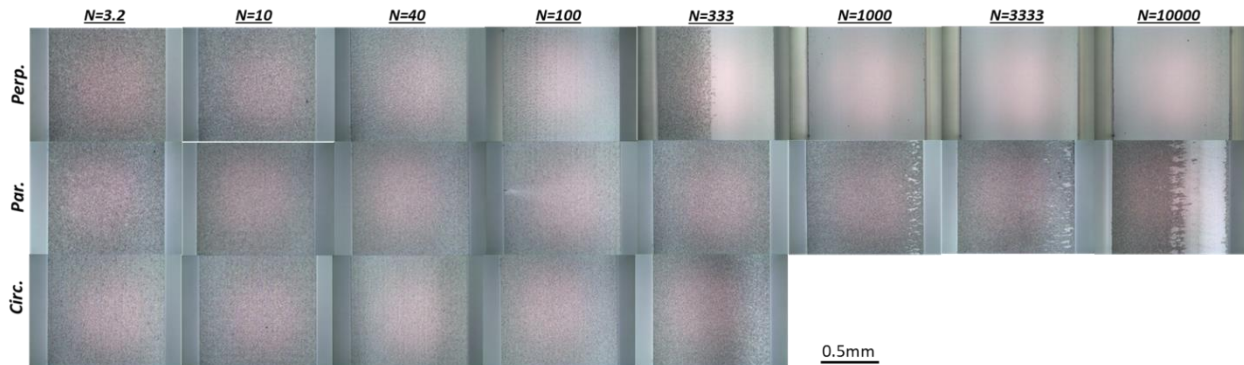

Figure 37. The microscope images of scanned surface with various writing condition

When N increases, the surface gets better in perpendicular polarization, but this phenomenon is not valid for the other polarizations. It is observed that for perpendicular polarization at given N is equal 333, while the half of the surface close to the bottom has better micro roughness, the other half close to the top surface gets high micro roughness. The reason could be the variation of pulse energy at closer to the bottom than top surface. To evaluate surface quality, the surface roughness is measured with and without filtering. While the filtered roughness data show micro roughness on the surface, the not filtered roughness data helps us understand the form on the surface. The overall polarization and overlapped pulse effect can be seen well in Figure 38.

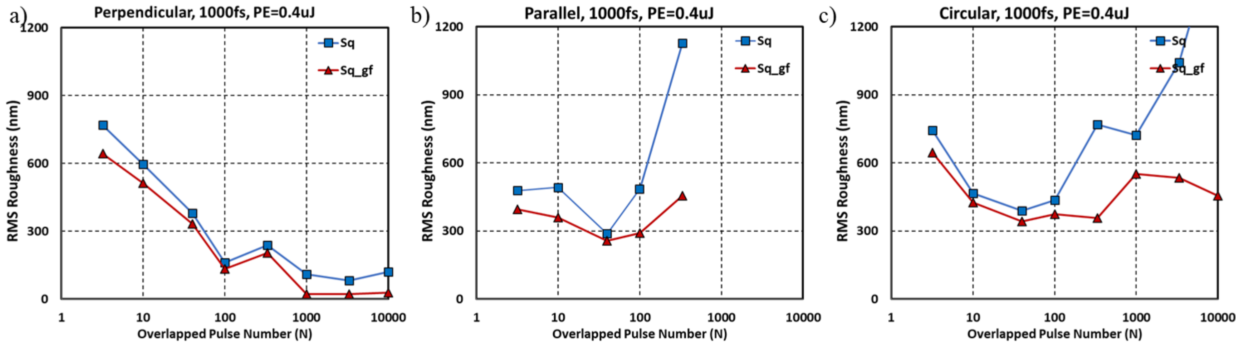

Figure 38. Surface roughness over overlapped number of pulses with 3 different polarization.

It is proven that the perpendicular polarized beam to wiring direction is giving the best surface quality in general especially with high number of overlapped pulses. According to the RMS roughness data, the best surface is achieved at N equal to 3333. The z increment and pulse energy are strongly related with each other. The nanograting size changes with pulse energy and depth of focus as shown in Figure 29. Thus, the z increment and the pulse energy should be analyzed together. The microscope images at various condition can be seen in Figure 39. While the brighter images represent the low micro roughness, the darker images represent the high micro roughness.

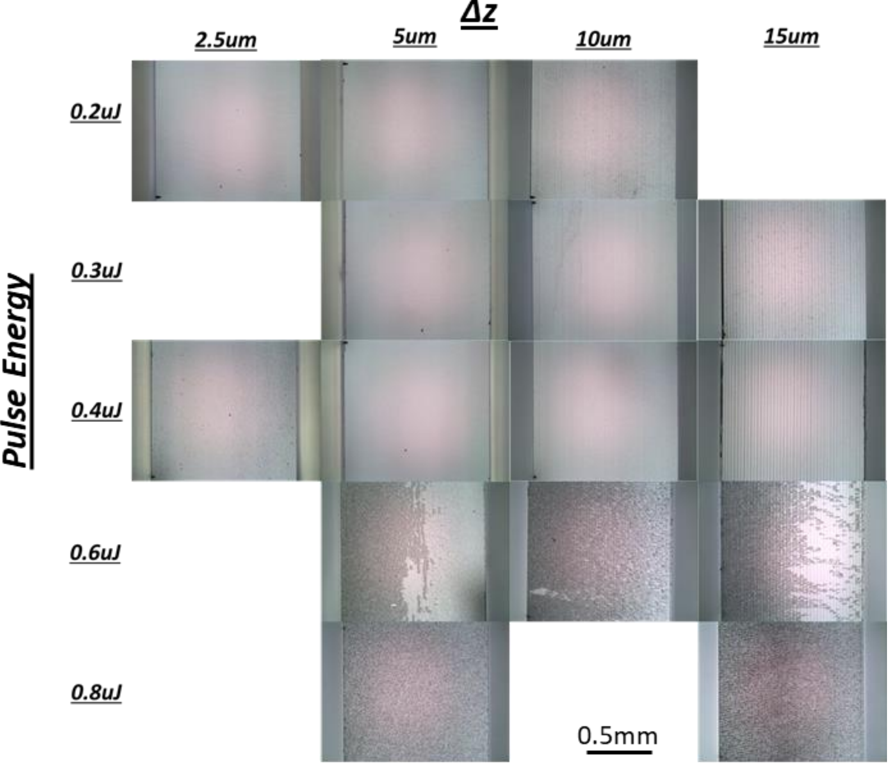

Figure 39. Microscope images of scanned surfaces for optimization

As seen in Figure 40, z stage increments have an undeniable impact on the surface quality. 2.5, 5, 10 and 15 µm increments in air are applied to the surfaces with different pulse energies, and surface RMS roughness and Gaussian filtered roughness are analyzed. Lowering the z increment will normally reduce the high surface roughness. However, it could deform the surface when the increment size reduces more. The result presented here is average value of scanned left and right side of the surface.

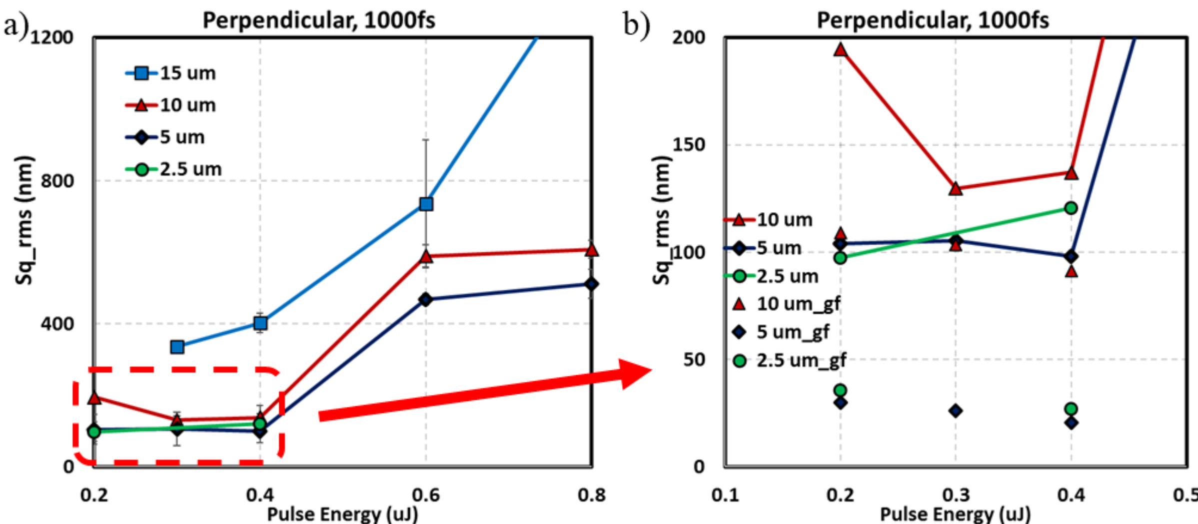

Figure 40. The laser writing conditions for best surface quality

The main goal of this study is to fabricate the silica plate in any desired shape. There are three considerations for optimizing the scanned surface. These configurations are high manufacturing speed, complex writing and high surface quality. The laser parameters should be optimized for need of the application. Some of the configuration can be adjusted as shown in Figure 41 according to application need like speed, complex writing and surface quality.

Parameters	*Configuration 1 (Speed)*	*Configuration 2 (Complex Writing)*	*Configuration 3 (Surface Quality)*
PRR	2 MHz		
Pulse Width	1000 fs		
Beam Polarization	**Parallel**	**Circular**	**Perpendicular**
Exp. spot size	~1.9 um		
Pulse Energy	0.4 uJ		
Number of pulse N	**3.2 (1.25m/s)**	**40 (>100mm/s)**	**3333 (1.2mm/s)**
Z inc. in air	5um		
Etching specs	12-24hr at 5% KOH, 85°C with 75rpm		
*Surface RMS Roughness Sq (1*1mm2)*	**Sq = 477nm Sq_gf = 395nm**	**Sq = 388nm Sq_gf = 341nm**	**Sq = 63.4nm Sq_gf = 21.8nm**
Surface 3D Profiles			
Surface 2D Profiles			

Figure 41. Some of the optimized configurations for the application needs for high manufacturing speed, complex writing and high surface quality.

3.3.5 45° Coupler Surface

Using FLICE, not deformed and good side wall surfaces have already been realized with relatively low surface roughness. Once the sidewall is optimized, the coupler is aimed to be optimized. The coupler in our waveguide design is 45 degree surface attached to the waveguide. The coupler surface is a critical part of the fabrication as it leads the collected lights from lens to the inside of the light pipe. Surface of the coupler ought to be as smooth as possible and highly reflective, which bears the need for high reflective coating. Fabrication of the coupler is a challenging process with several problems to overcome to reach the desired quality.

Above all, there is a significant surface quality difference between the top and bottom 45 degree surfaces due to the modified zone at the focal beam. Figure 42 depicts the top and bottom faces of the coupler.

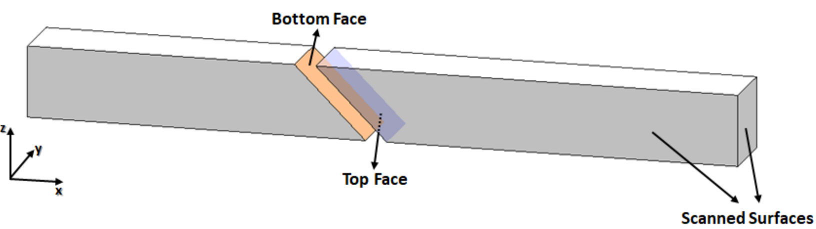

Figure 42. Top and bottom face of fabricated 45° coupler surface

The modified spot area is not exactly a circle as it is expected due to focusing and beam waist but is elliptical reflecting that the beam propagation direction (z) is a little over the other plane which is perpendicular to the writing direction. The power effect is greatly related to objective numerical aperture (NA). The refractive index of silica plate could change during the exposure and generates self-focusing phenomena inside the glass because of high intensity.[62] This process will increase the intensity at focal spot, and spot diameter will change as a result leading a non-uniform exposure over z axis. Moreover, the modified focus spot has a tail towards the propagation direction as shown in Figure 43.[63]

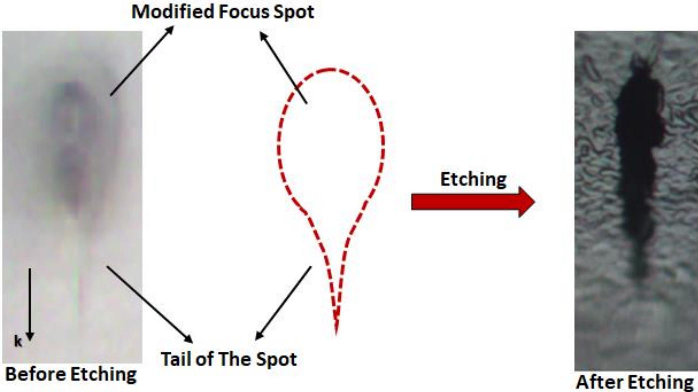

Figure 43. The modified focal spot before and after etching

Channel has aspect ratios from 3.2 to 4.7 at given pulse energy of 0.2 to 1.6 µJ respectively. For a given 0.4 µJ pulse energy at 1000 fs pulse duration, the modified and etched channel lateral and vertical dimensions are 5.5 µm and 23 µm respectively with the aspect ratio of 4.24.

The tail of the focal spot deteriorates the surface quality of the 45 degree surface top and bottom faces. While the top face has larger modified area incurring smooth surface, the bottom face has a highly rough surface with the effect of the tails. Thus, the top face of 45 degree modified region is preferred for the following studies.

Secondly, z increments which lead quite different surface profiles on the 45 degree face should be tested and adjusted not to have patterns on the surface as seen in Figure 44.

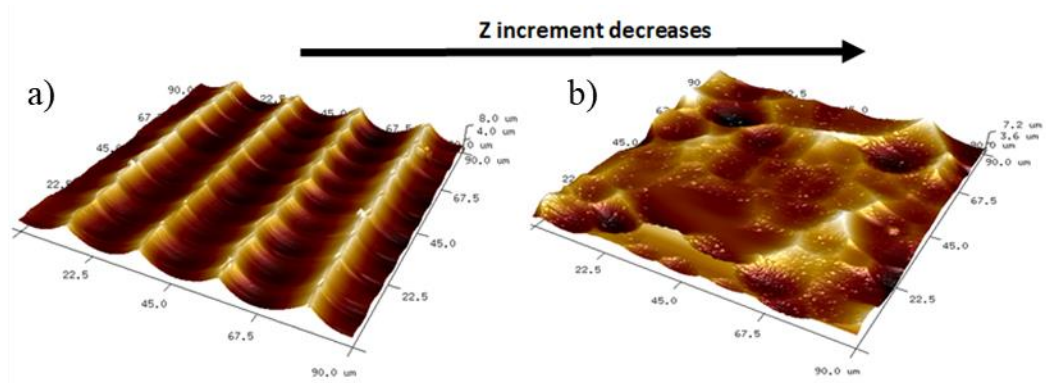

Figure 44. AFM images of etched surface with various z a) Δz = 15 µm, b) Δz = 3 µm

However, the surface quality gets worse if the z increment is too small. Z increment optimization results are demonstrated in Figure 45. 2.5 µm z increment has the better surface quality than the others. The graph in Figure 45 reveals the RMS roughness values versus z increments.

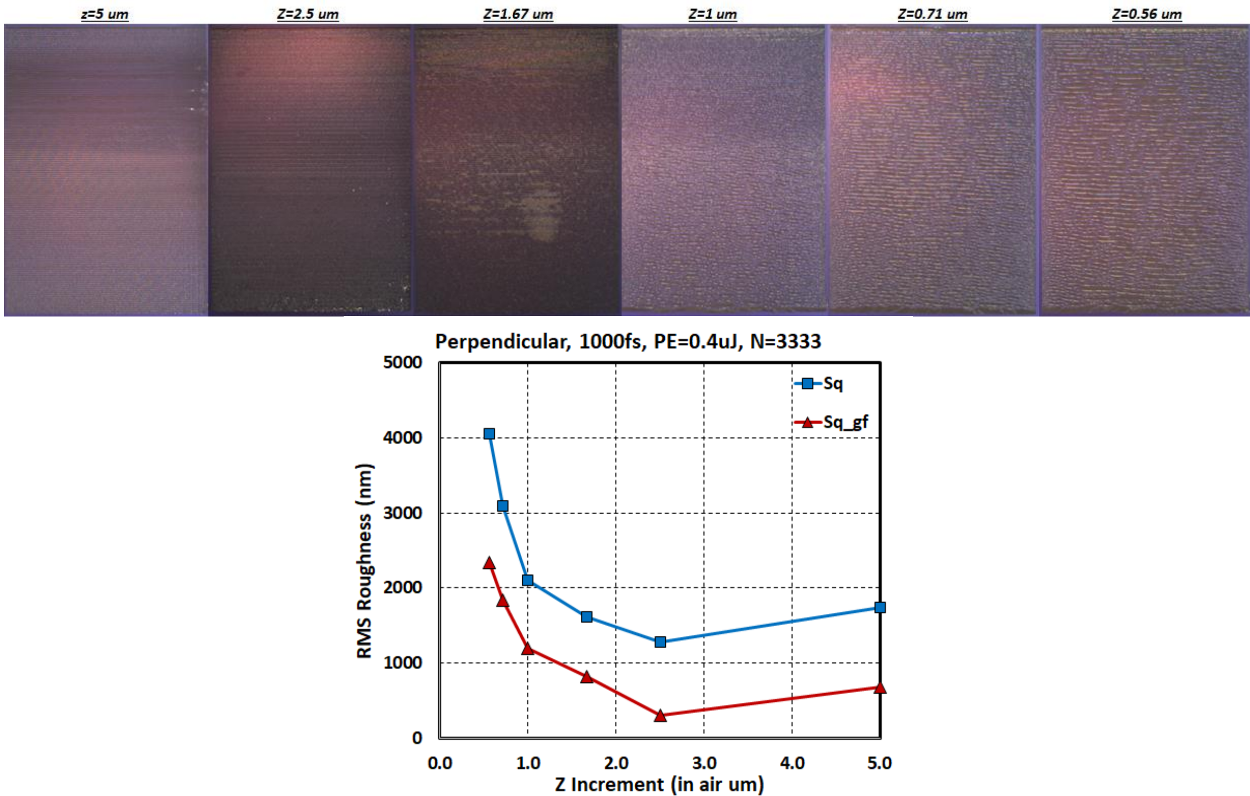

Figure 45. 45° coupler surface microscope images with various z increment and z increment vs surface roughness of all coupling surface (1 x 1.41 mm^2)

One of the competitive advantages of this process is being able to get precision. Due to the nm level stage accuracy and repeatability, we can get accurate tapered surfaces. The increments in both directions are adjusted accurately in line with the optimization results and the 45 degree angle is achieved with the accuracy less than ±0.5° as shown in Figure 46.

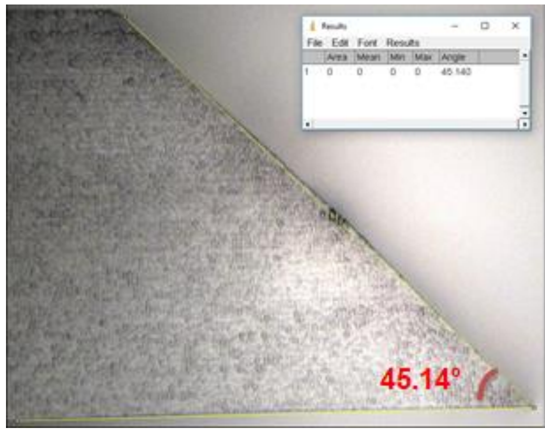

Figure 46. Microscope image of 45° surfaces for angle measurement

3.3.6 Other Process Capabilities for Complex Structures

It is possible to fabricate some other complex structures with a precise motion control and good programming skills. Different light pipe designs are tested and fabricated successfully. Figure 47 exhibits a side tapering as the secondary concentration in the light pipe which has reached the desired micron level thickness and has been released without any cracks at the edges or corners as top and side view shown in Figure 47.

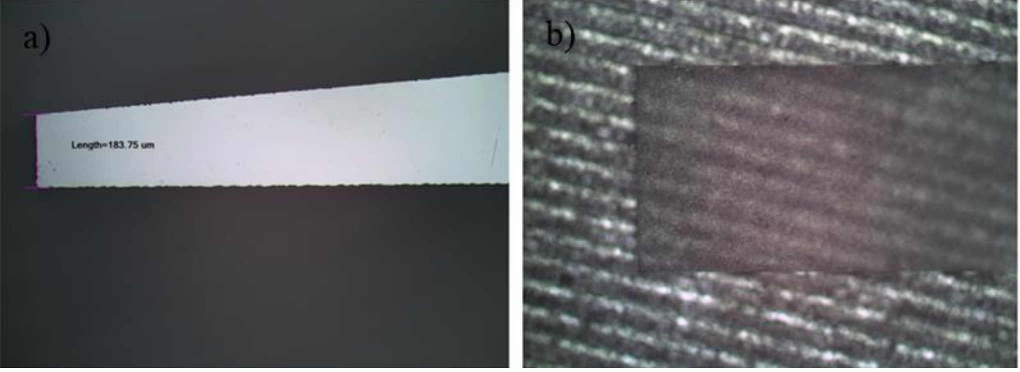

Figure 47. Released the tapered surface without cracks at corners a) top view, b) side view

Releasing less than 200 micron size sample without any cracking and getting 45 degree surface with sharp edge prove the feasibility of the process for the industry. In addition, the accuracy of side tapering which can be seen in Table 3 support the capability of producing accurate samples. The measured horizontal tapered surface angle is matches with designed angle with accuracy of ±0.01°.

Table 3. Accuracy of horizontal tapered surface angle

Designed	Measured
1.13°	1.14°
2.29°	2.29°
3.43°	3.44°
4.57°	4.58°

However, it should be remembered that there may be some design specific challenges. Crack propagation is observed at the corners because of fast polarization shift. To eliminate this unfavorable situation, the dwell time at the corner is adjusted. Before and after optimization images shown in Figure 48 represent the improvements. Cracks are disappeared after changing the coding and adding milliseconds dwell time at the corner of the turn.

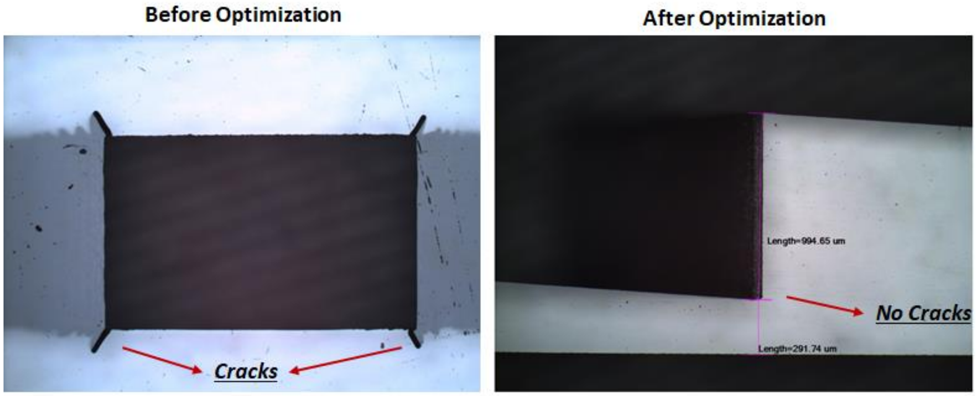

Figure 48. The cracks at the corners are prevented after optimizing the coding

A simple staggered structure has been decided to fabricate for testing the projects other goals like HR, AR coating. Optimization studies has resulted in success, and the proposed 1x3 straight light pipe without tapering and 1x2 both sides tapered light pipe for 1000x concentration has been achieved. Tapered waveguide structures are key elements to reach high concentration. It is understood that any desired structure is possible to realize. A complex prototype including horizontal tapering and bi-directional tapering as well as 45 degree coupler surfaces is shown in Figure 49. We have successfully achieved small 3D shaped structure less than mm level with FLICE technique.

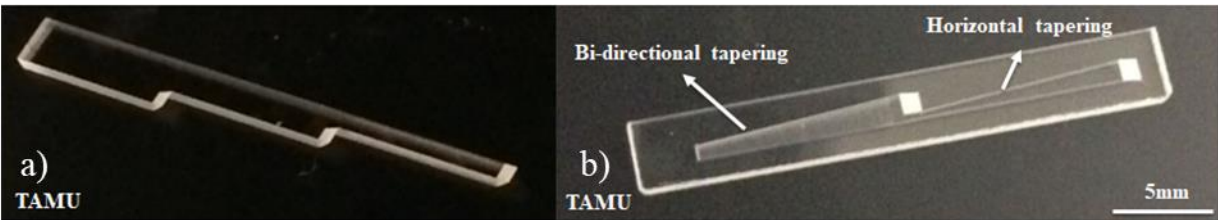

Figure 49. a) 1x3 straight staggered light pipe, b) 1x2 bi-directional tapered light pipe

4. GLASS POLISHING FOR LOW SURFACE ROUGHNESS AND DEFORMATION OF LIGHT PIPES

4.1 Glass Polishing Techniques

Applying FLICE we can get the silica waveguide in the exact shape we desired. However; we need a better surface quality to eliminate the drawbacks of a rough surface. To acquire such a smooth surface, we decided to polish the FLICE processed sample. Among many glass polishing methods only a few of them are applicable for our study. We can divide the glass polishing methods into two group as conventional and non-conventional glass polishing. The conventional polishing can be named as full lap polishing that includes pitch, polyurethane, Teflon, float and fixed abrasive polishing techniques. This polishing technique is contact based, which is impossible to apply to our micro level glass samples. For this reason, the non-contact method or sub-aperture polishing methods outshines the other as seen in Table 4.

Table 4. Contact free polishing techniques

	ION BEAM POLISHING	ATMOSPHERIC PRESSURE PLASMA POLISHING	MAGNETO RHEOLOGICAL (MR) POLISHING	ELASTIC EMISSION MACHINING (EEM)	LASER POLISHING
	Low-energy ion-beam sputtering on the sample. nm level beam sizes	Chemical reactions between reactive plasma and surface atoms	MR particles becomes aligned and form chain in MR fluid under magnetic field	Chemical reaction between fine powder in pure water and workpiece	CO2 laser is used because of the absorption Surface should be heated below the evaporation temperature
BENEFITS	• Atomic level polishing • Controllable beam	• Atomic level metal removal • No need high temperature	• 1nm smoothness achievable • Selectable particle size	• Atomic level surface finishing	• Various surface geometries • Selective polishing • High speed • 1nm smoothness achievable • No polishing waste • No liquid needed • Remove cracks on the surface • Keep overall shape
LIMITATIONS	• Slow removal rate • Small areas • Need high temperature • Expensive	• Slow removal rate • Hard to selective polishing	• Robotic arms needed • Not applicable for small 3D samples	• Need large surface area	• Precise temperature control

Non-contact polishing can be introduced with different methods such as ion beam polishing,[64] atmospheric pressure plasma polishing,[65] magneto rheological (MR) polishing,[66] elastic emission machining (EEM)[67] and CO_2 laser polishing.[68-70] Ion beam polishing is atomic level surface finishing that uses ion beam sputtering to remove atoms by using energetic ions to success sub nanometer surface roughness. This process is considerably expensive and has a long run of polishing cycles. Atmospheric plasma polishing is also atomic level surface finishing method that uses chemical reactions between surface atoms and reactive radicals generated by reactive gas and plasma gas mixture. This method also achieves sub-nanometer surface finishing. It is generally used after conventional contacting machining processes to minimize the defects. Even if this technique is cheaper than the ion beam polishing, it is a more expensive method than others and has a low material removal rate. Magneto rheological (MR)

polishing is another method that uses a fluid containing magnetically soft ferromagnetic particles that polarizes and forms chains to increase yield stress of the fluid which polishes the surface needed. Although 1 nm surface roughness can be achievable, this process is very costly process. Elastic emission machining (EEM) uses fine abrasive grain particles in pure water to remove atoms or molecules on the surface by making a fluid flow on the workpiece. Sub-nanometer level surface finishing can be achieved by this technique, however may introduce undesirable surface deformities.

All of these techniques have drawbacks for our study; while some are pretty expensive and slow, some are not applicable for polishing our stair shaped waveguide design. On the other hand, CO_2 laser polishing techniques rely on laser surface heat treatment by using the high absorption coefficient of the glass sample for given 10.6 µm wavelength laser. The surface is heated slightly below the evaporation temperature and causes glass to flow under surface tension. As a result, it will reduce the roughness without changing the shape of the sample. By using this technique and preheating the glass, approximately 1 nm roughness can be achievable without forming low frequency deformation [68, 71].

4.2 CO_2 Laser Processing of Silica

CO_2 laser polishing has been preferred for post processing as it is a fast, local and non-touch based method without any loss of material or need for polishing agent making it advantageous over the conventional techniques which are time consuming.[72] This system can be summarized as the reduction of viscosity in the surface layer with the heat effect and decrease of the roughness with surface tension caused by viscosity reduction. The radiated laser is absorbed in thin layer of the silica plate. The fused silica has softening (melting) point of 1665°C and

annealing point of 1140 °C. Since above the melting temperature could lead the surface material removal and surface deformation, the desired temperature should be lower than melting temperature.[69, 73]

The wavelength for CO_2 is around 10.6 μm which has very high absorption coefficient for most of the materials. Silica has high absorption at given infrared wavelength that penetration depth of the laser beam through the silica plate is less than 30 μm which makes CO_2 laser a good candidate among the other lasers with different wavelengths.[74] The laser reduces the viscosity with thermal energy induced by absorption and causes a flow of a thin surface layer with surface tension forces.[75] Silica has elastic vibration of oxygen atom between two Si atoms, which results in local heating. The linear absorption is described by Beer-Lambert Law, which expresses the intensity reduction as following:

$$I(z) = I_0 e^{-\alpha z}$$

$$\alpha = 4\pi k/\lambda$$

where I_0 is initial intensity of laser beam after subtracting the back reflection, α is absorption coefficient which is wavelength and temperature dependent, k is extinction coefficient of silica and z is the propagation distance.

The laser polishing has high processing speed with minimal shape change without material loss, however; it requires precise temperature control. For a satisfying result, the surface should be heated homogeneously below the evaporation temperature. Laser interaction time, laser intensity, initial roughness, ambient temperature and heat control are the factors to be considered during the polishing process. Besides, waviness formation is faced as a big challenge during polishing the

process. Surface spatial wavelength analysis plays a key role for evaluating the polishing process efficiency.

Heidrich argues that a spatial wavelength larger than 100 µm requires more interaction time for achieving conventional roughness range while less interaction time is enough for smaller spatial wavelengths. There is a strong correlation between interaction time, temperature of the sample and roughness. Over exposure time will lead to surface deformation. [76, 77] The laser polishing of glass is conducted for many years[78] and used for fabricating micro optics.[79] There are some other studies that uses defocused beam.[69, 80]

In this chapter, CO_2 laser polishing is applied to the silica rod that is fabricated by FLICE technique. The laser experimental setup and specifications, optical beam path, beam focusing, sample preparation, alignment, laser exposure parameters and surface measurement will be discussed in detail.

4.3 Experimental CO_2 Polishing Setup

Synrad Ti series 60 watt water cooled CO_2 laser is used for this study. The IR beam is collimated with diode pointer for alignment and visualization purposes. The polishing system schematic and experimental setups are represented in the Figure 50.

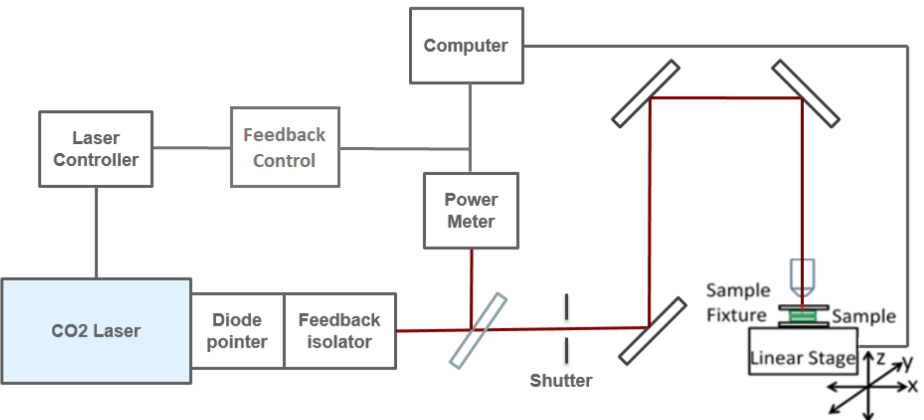

Figure 50. Schematic of polishing setup

The laser manipulation is administered using laser power, duty cycle and modulation frequency. Laser power is modulated with pulse width modulation (PWM), and it is related to raise/fall time and duty cycle; scales up with increased duty cycles. A uniform optical intensity is required for the polishing process; thus, the laser should have a continuous wave to prevent power fluctuation. Though it is a pulsed laser it could behave as a continuous wave laser after adjusting the PWM frequency. The laser PWM frequency is determined as 20 KHz that gives 50 µs periods, and the rise time is set 75 µs. These conditions enabled the laser act as a continuous laser. The laser specification can be seen in Table 5.

Table 5. CO_2 laser parameters

Parameters	**CO_2 Laser**
Power	60W
Mode Quality	$M^2 < 1.2$
Rise Time	75 µsec
Beam Diameter	2.2 mm ± 0.3 mm
Beam Divergence (full angle)	< 7.0 mR
Wavelength	9.3 µm/10.2 µm/ 10.6 µm
Power Stability	+ 7%/+ 6%
Cooling	Water

A diode pointer emitting the red laser beam is attached in front of the laser head. This pointer has adjustment knobs that helps us to align the laser and pointer beam at near and far field distances. Feedback isolator is used to protect laser from back reflection which affects the power stability of the laser. The linearly polarized laser beam gets circularly polarized after the isolator. The wedge zinc selenide window is placed in an angle to the beam to divide the input beam power. The reflected beam is measured by power meter, and the laser power is measured and controlled by this reflected beam. There are many attenuated copies of the reflected and transmitted beams from wedge surface due to multiple reflections as shown in Figure 51.

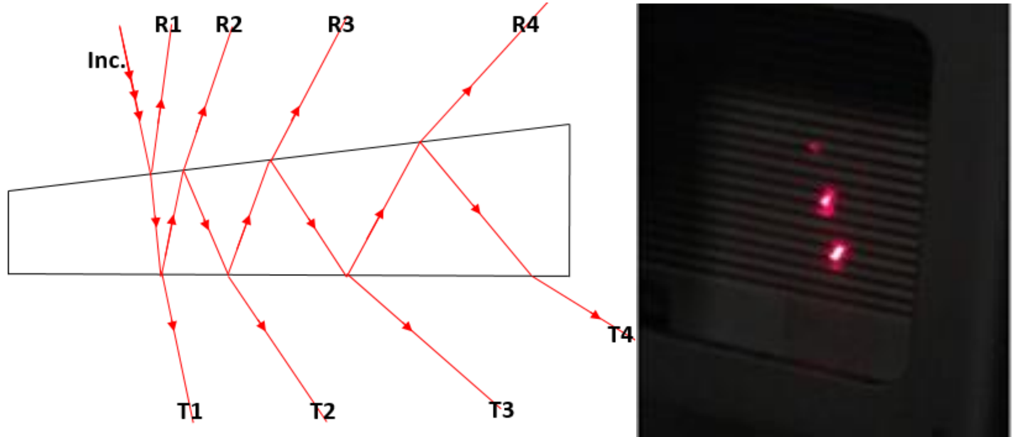

Figure 51. Attenuated copies of the reflected and transmitted beams

The aperture of the power meter covers all the reflected beams. The first order transmitted beam is used as the primary beam for the polishing process. Nearly 33 % of the incident power is reflected while the 67 % of the incident power is transmitted. 89.8 % of the transmitted power is measured on the 1st order of the beam. The other 10 % power is from the following order beams.

Laser stabilization is a big hurdle against maintaining the laser polishing process. The laser demands couple minutes to minimize the power fluctuation. The laser is run for a while to get stable output power in the tests. It is observed that the laser power fluctuation frequency changes over time. While it fluctuates at high frequency at the beginning, later the frequency is decreases. In the experiment, the stable power output is chosen for the experiments. In later on the laser stability is controlled with a feedback system that measures the laser power and adjust the laser PWM according to the measured power. A high reflective mirror is assembled on a motorized rotation stage as a shutter to avoid the laser beam on the workstation. When the shutter is on, the laser is guided to beam blocker that absorbs the laser power. When the shutter is off the beam follows the path through the work station.

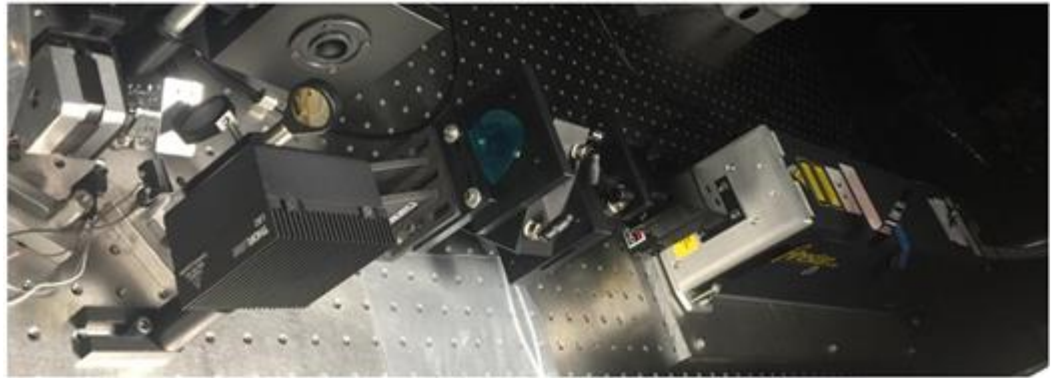

Figure 52. The experimental setup consists of the CO_2 laser, diode pointer, isolator, beam splitter and shutter

The beam after couple reflections from the mirrors is focused to workstation by zinc selenide plano convex lens with a 50 mm focal length. Beam diameter is 2.2 mm at the aperture, around 7.7 mm at the lens calculated from the divergence angle, and the full angle of beam divergence is 7 mrad. The beam propagates nearly 1.9 m away from the laser aperture. The beam size on the lens is also measured after lens focusing and the measured data are closely matches with the calculated beam diameter. The beam size measurement is performed by measuring power with precise aperture control in front of power meter.

A small spot size places on the sample when the sample is at focus or the working distance, the distance between the lens and the sample, is equal to the focal length of the lens. This small focal spot is highly evaporative and could deform or even cut the glass. In the experiment, the sample is placed under the focal point to get larger spot size which is favorable for polishing experiment. This large spot size heats the silica surface but does not evaporate the sample. Approximately 78% transmission on the power is obtained at the end of the whole path of beam

delivery. Hence, transmission to the stage is 47% of the initial laser power, which corresponds to ~ 1.56 times measured power from power meter after reflection from the sampler.

The sample is placed on a sample holder that has both vacuuming and heating system. The vacuum chuck is designed to hold the silica rod while the temperature is controlled with thermocouple. The hot plate with vacuum chuck is placed on a manual pitch, yaw and rotation stages on the top of Thorlabs xy two axis motorized linear stages. The lens is mounted on z axis linear Thorlabs stage. ActiveX Control interference is built in C++ to control the stages in a more professional way. The work station can be seen in Figure 53.

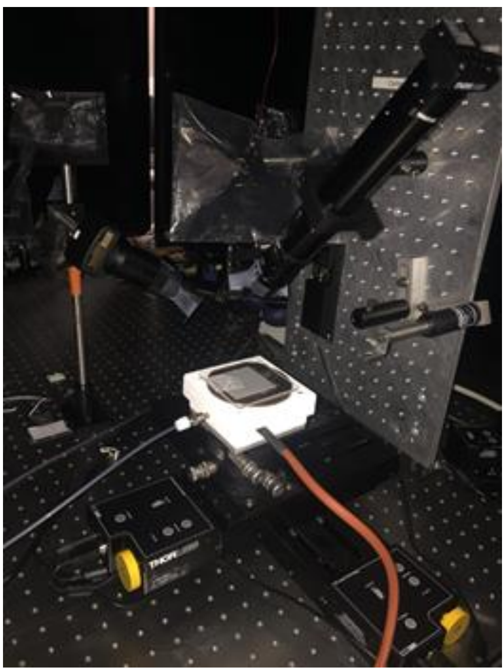

Figure 53. The laser polishing work station with stages, heater, vacuum chuck and imaging systems

A rod silica sample (1 mm x 1 mm x 70 mm) is prepared by FLICE process to employ in laser polishing experiments. Fabricated sample is cleaned with water, methanol and Isopropyl

alcohol (IPA) and placed on the sample holder. The scanned rough surface of the sample is faced towards the z direction.

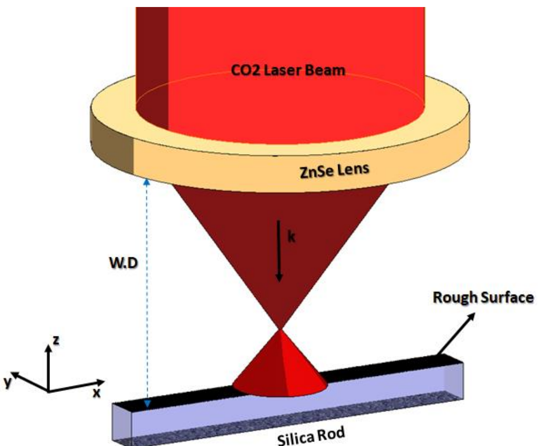

Figure 54. Laser exposure on silica rod with defocused laser beam

The Gaussian function represents the intensity distribution over the distance from the beam center, and intensity distribution can be described by the following equation:

$$I(r,a) = \frac{2P}{\pi a^2}\exp(\frac{-2r^2}{a^2})$$

where P is beam power, I is the beam intensity, a is the beam radius where the intensity drops to 13.5 % of the peak intensity at center of the beam and r is the distance from the center of the beam. The P_e power contained within the radius of r can be expressed as

$$P_e(r,a) = P[1 - \exp\left(\frac{-2r^2}{a^2}\right)]$$

Defocused CO_2 laser beam under f enables a sufficient working distance between the lens and substrate. It is located on rough silica sample and moved at various speeds and configurations

to polish the surface. In addition to calculating the expected spot diameter at a given position, the spot size is measured by precisely adjusting the aperture on power meter. The effective spot size on rough silica sample is tried to be analyzed, however; it is a challenging task. For instance, affected area or fingerprint on rough silica sample changes with various power and various exposure durations. The most important polishing parameters are laser power, beam diameter, interaction time, scanning speed, material and ambient temperature which have a significant effect on surface temperature.

Imaging the temperature is very important part of the polishing process which require fine temperature control. Because the contact measurement is not applicable for a small scale heat measurement, the contact free temperature measurement is the only solution that needs to be applied. The atoms and molecules have their own vibration, and when the heat is applied to the material, the space between the atoms and the vibration speed increases. The effect of this energy can be seen with various forms like volume, pressure, charge and radiation. The detection of the radiated energy can be measured via inferred detectors and cameras which detect the emission of electromagnetic radiation from the heated and non-heated surfaces. A thermal camera (FLIR A310) is used for temperate measurement. The camera temperature range is up to 350°C which is pretty low temperature when compared to softening and melting point of silica. As the process requires both laser radiation and measurement at the same time. The laser reflection is one of the biggest challenge for the process that not only damage for human body but also for thermal imaging. To use thermal camera properly, it requires proper filters and precise calibration of glass with considering the emissivity of silica which temperature dependent. Alternative solution is proved via light source and CCD camera. The light source with low divergence is placed with a

certain angle to illuminate the sample surface. The CCD camera with attached zoom optics is placed the opposite side of the light source with a certain angle. When the surface is rough, the illuminated light on the sample surface diffuses the light and the camera doesn't collect enough light. When the surface gets polished, the surface reflects more light at given angle and the camera collect enough light for imaging. The polishing process is performed with the manual control and imaging. For automated laser control, the image processing is studied via counting the black and white pixels on record at the same time, and adjusting the working distance accordingly.

5. POLISHING PROCESS DEVELOPMENT AND EXPERIMENTAL RESULTS

In this chapter, CO_2 laser polishing procedures and experimental data will be presented. Several attempts have been made to polish the rough silica plate. Raster scanning on different directions and combination of the transverse scans will be mentioned first with before and after polishing AFM images. The 1 mm width polished surface will be analyzed under optical profiler to observe the large polishing area and see the deformations. After discussing the laser polishing challenges and some solution approaches, the successfully polished surfaces will be demonstrated.

5.1 Raster Scan as a CO_2 Laser Polishing Method

In raster scan mode the laser PWM is adjusted to 35% which delivers 18.7 W to the stage. The lens focal length is 50 mm and the working distance is adjusted to nearly 60 mm which gives 1.68 mm beam radius according to the measurement that we explained previous chapter. However, the measured effective beam radius is measured roughly 0.5 mm at given condition. The measurement is performed on rough silica plate by measuring the polishing area on the plate. The effective beam size is prioritized for polishing the surface via raster scanning which is multiple scanning back and forth with an increment in transverse direction. CO_2 laser raster scan polishing is performed along the longitudinal, transverse direction according to the sample long surface. The initial polishing capabilities is first optimized under optical microscopy for reducing the spent time and money. To increase the production and efficiency, the diced silica samples prepared by dicing saw tool are used in the tests.

First of all, the raster scan is applied in the X direction with three different speeds, and it is observed that 2 mm/s scan speed gives us a good result without visible deformation at the edges

which are more prone to deform as shown in Figure 55. While the laser and material interaction time increases the surface gets better according to roughness, but the deformation is increases dramatically. When the interaction time decreases, the sample roughness doesn't reduce enough. The observed surface roughness will be presented afterwards.

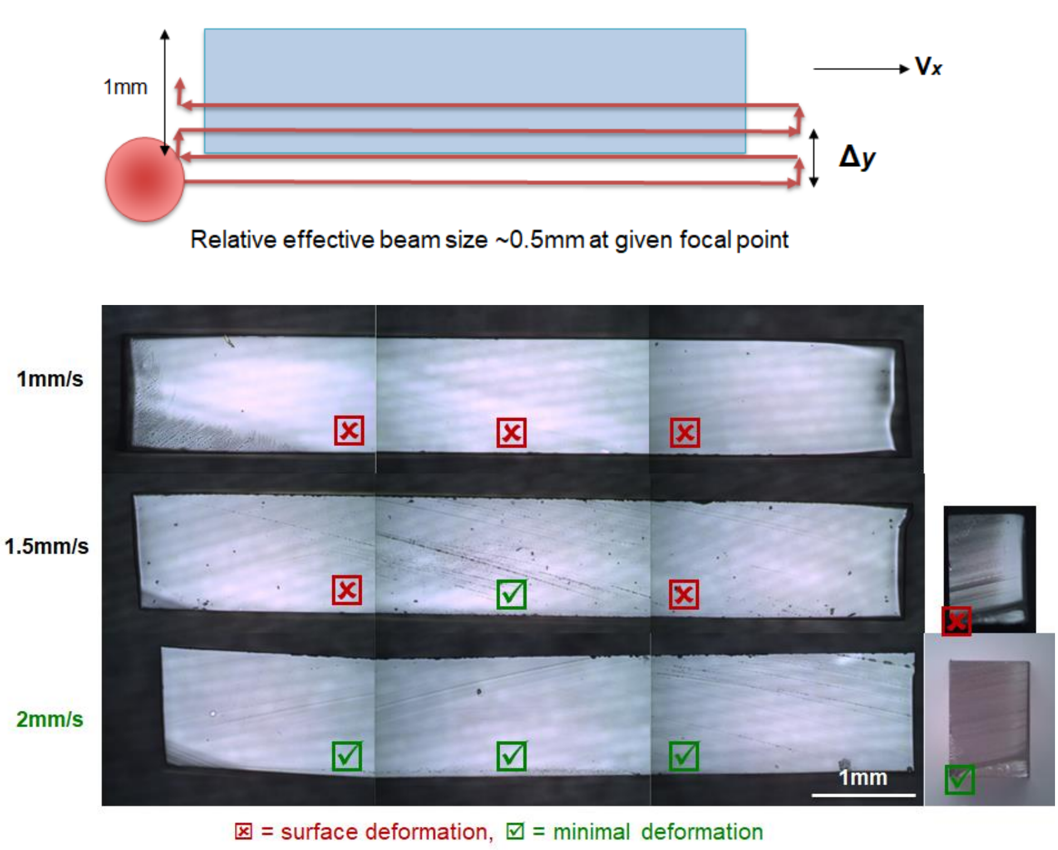

Figure 55. X direction raster scan polishing and deformation analysis

CO_2 laser raster scan polishing is performed along to the Y direction as shown in Figure 56 which gives us much better control for the polishing process. Raster scan is applied in the Y direction with different speeds and it is observed that the combination of 1 mm/s y direction scan

speed with 0.0111 mm/s x direction scan speed gives us the best result without any deformation at the edges as shown in Figure 56. Because we have high priority on the shorter edges, the Y axis raster scan gives us better control at the short edges. However, this process increases the polishing time as the laser is running off sample many times.

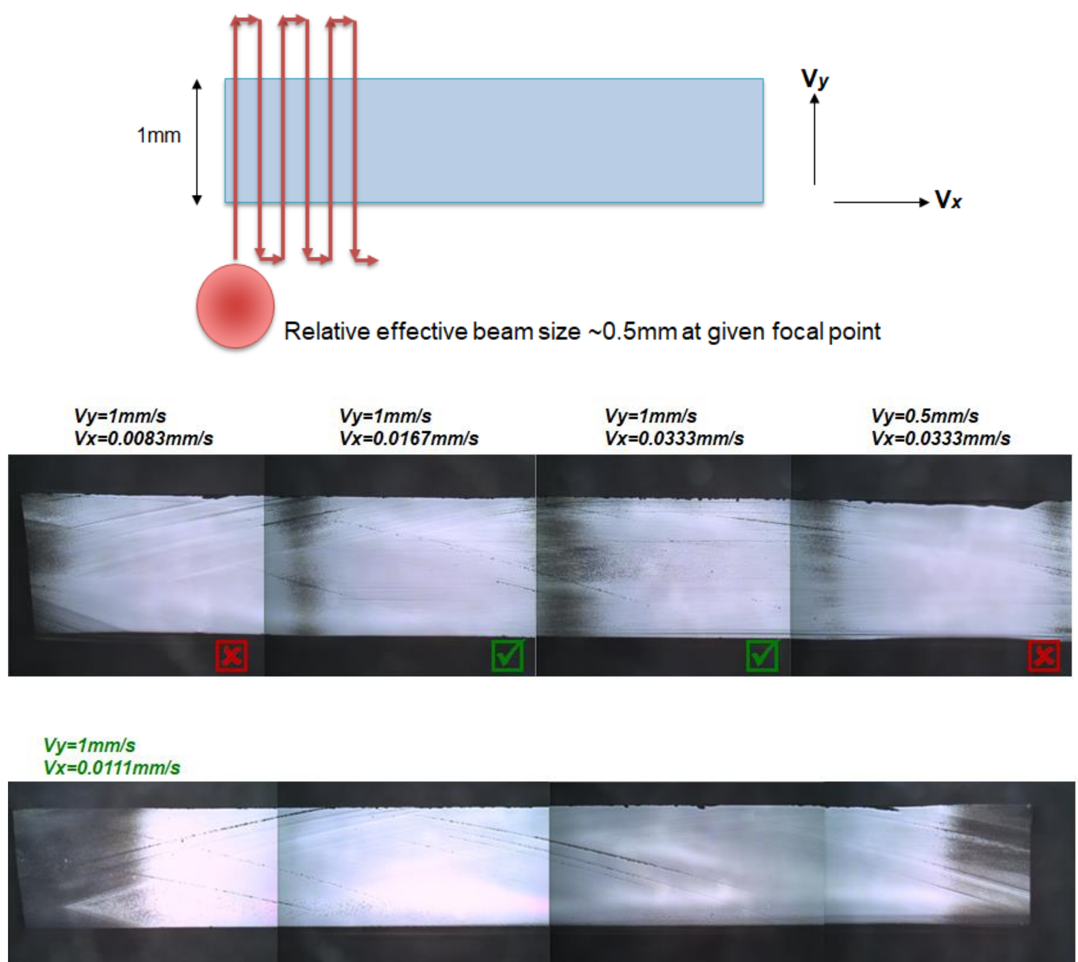

Figure 56. Y direction raster scan and polishing and deformation analysis

To get the optimum polishing, CO_2 laser raster scan polishing is performed along both x and y directions. Raster scan is applied in transverse direction with 1 mm/s y and 0.0111 mm/s x

direction speeds followed by longitudinal scans with 2 mm/s x direction speed with 50 nm y direction steps. The polished rod surface is shown in Figure 57.

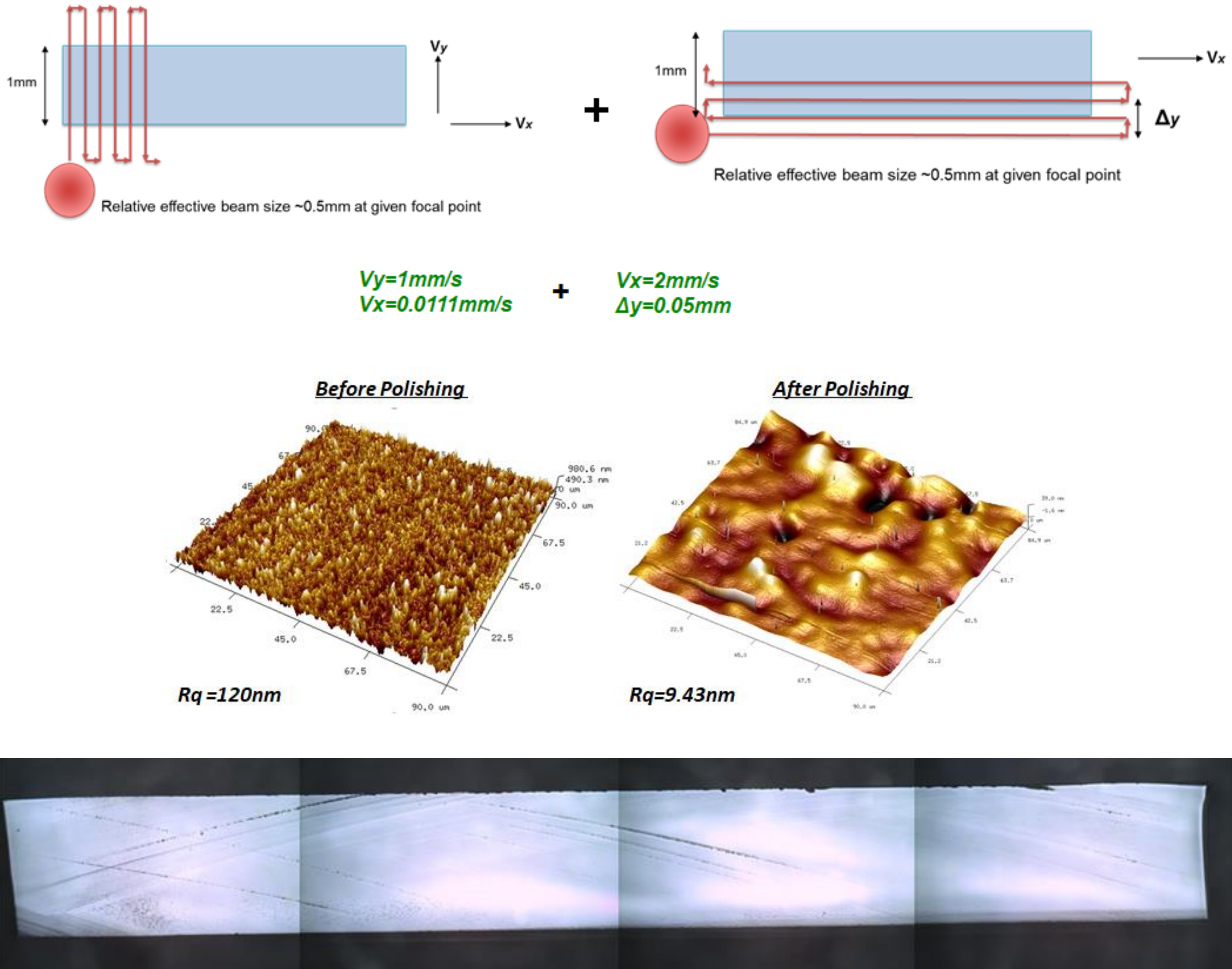

Figure 57. One pass Y+X direction raster scan polishing and deformation analysis with AFM and microscope images

The AFM data show us RMS roughness has decreased dramatically from 120 nm to the roughness under 10 nm with only one time combined raster scan. This clearly shows the process capability on polishing process. To further improve the surface quality of the surface, multiple

raster scans are tested. Multiple scans will eliminate the surface deformations. We kept the conditions same as one pass both directional raster scan polishing test.

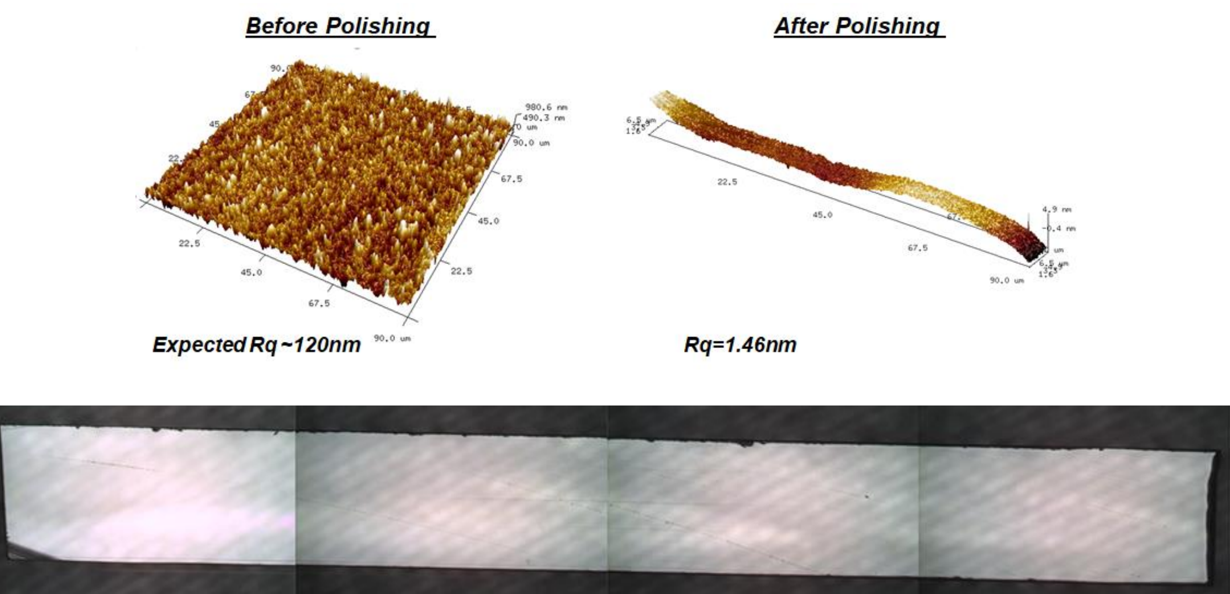

Figure 58. Polishing test with multiple passes Y+X direction raster scan of AFM and microscope images

The AFM data show us RMS roughness has decreased dramatically from 120 nm to the roughness under 2 nm as shown in Figure 58. As it can be seen from the experimental results, multiple passes of raster scanning has improved to surface quality to precision level for given 90 μm AFM scan size. We anticipate that further improvement can lead us to sub nanometer level polishing.

As observed from the polishing experiments, less than 2 nm RMS roughness can be achieved for the surface which has around 120 nm surface roughness. To implement this process for highly rough surfaces like 45 degree surface, multiple passes both directional raster scan has

been applied to rough surface which has 931 nm. The AFM data showing us RMS roughness has decreased remarkably from 931 nm to the roughness under 2 nm. This result implies that our method is applicable for rough surfaces like 45 degree coupling surface and makes the surface of typical quality for optical elements. The microscope images of polished and unpolished surface are represented in Figure 59.

Figure 59. Microscope and AFM images of rough surface before and after polishing

Roughness consist of surface irregularities which can be best described via power spectral density (PSD). The PSD function explains the amplitude of a surface's roughness as a function of the spatial frequency which is the inverse of the wavelength of the roughness features. The PSD function represents periodic surface features and provides a graphic representation of how such

features are distributed. The 2D PSD, which is the square of the surface profile's Fourier spectrum, contains all information about both the vertical and the lateral structural properties. Figure 60 shows the CO_2 laser polished surface of fused silica with AFM after first attempt. The surface profile, power spectrum density (PSD) and slope analysis of the surface before and after polishing is shown Figure 60. The PSD is power spectrum of surface roughness.[81, 82] Roughness and slope relation with PSD are given in the following equations:

$$\sigma_{rms}^2 = \int 1DPSD(f)df$$

$$s^2 = \int (2\pi f)^2 1DPSD(f)df$$

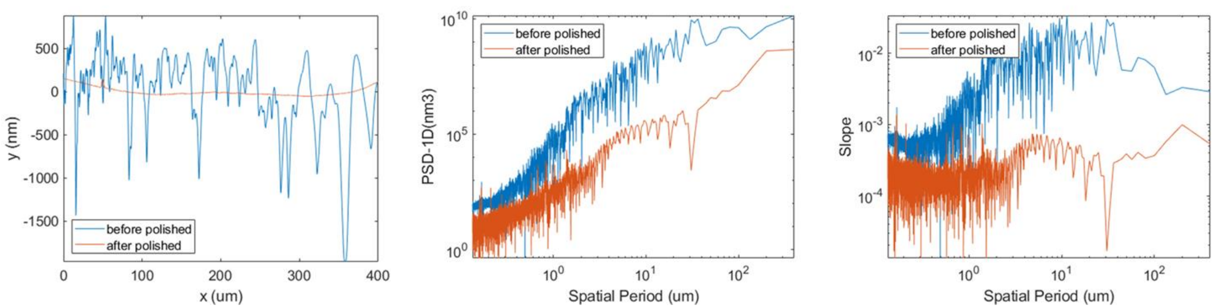

Figure 60. The profile, PSD and slope of the surface before and after polishing

The micro roughness of the surface is decreased well enough as it can be seen in the rms roughness data from AFM. Going forward, we want to improve our PSD measurements and fitting as follows: a) investigate larger scan sizes for fitting the longer spatial wavelengths, b) average values from multiple samples to improve the fit quality and c) understand the impact of surface

waviness on the goodness of fit and predicted optical waveguide loss. The overall surface profile before and after also clearly shows the surface improvement.

Even the surface seems great according to the optical microscope and AFM images, the larger scale imaging is required for understanding the laser polishing at shorter spatial frequencies of the surface. Thus, the polished surface is profiled by white light interferometry for large size scanning, and the profile obtained is shown in Figure 61. The deformation is clearly imaged with white light interferometry imaging. To understand the deformation at side, the surface height scale is heightened. In the following image, the initial surface gets deformed at sides when the laser exposure increases.

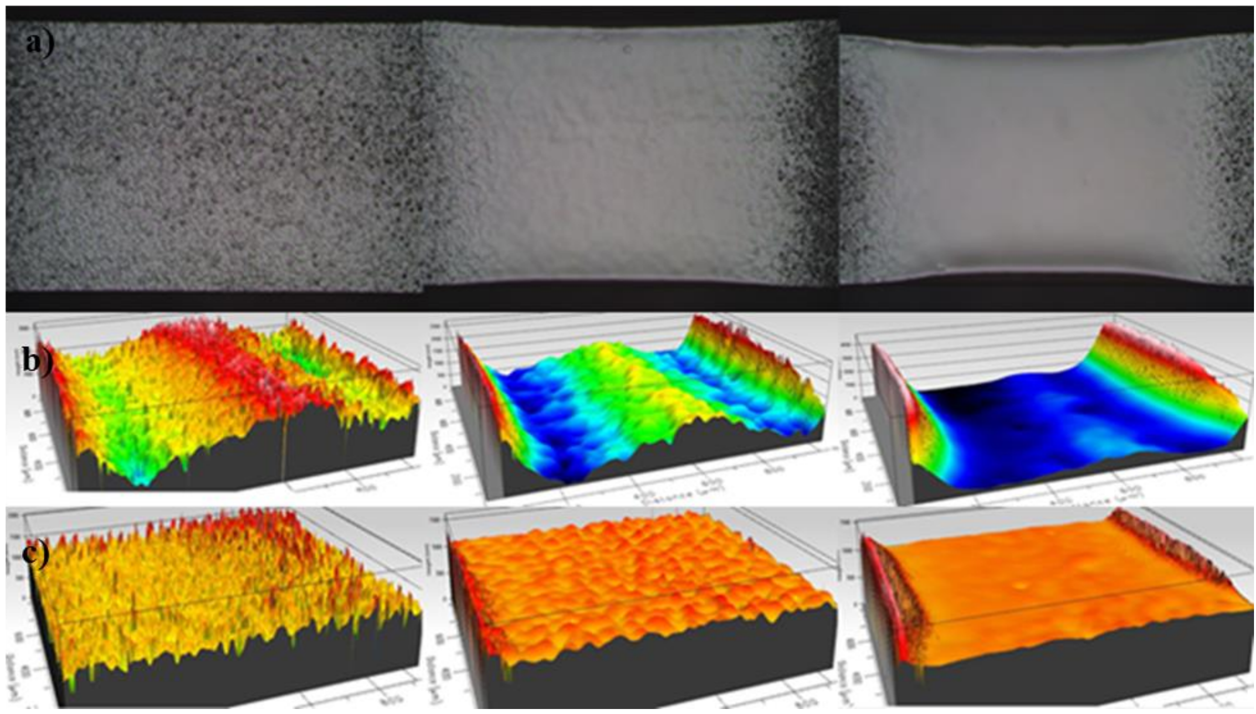

Figure 61. Raster scan polished surfaces a) Microscope images, b) true profile and c) filtered profile with Sq_gf = 121 nm, 34 nm and 11 nm, respectively.

While RMS roughness is 3.42 in the AFM with a scale of 90*35 μm^2 area, it is 11 nm after 80 µm Gaussian filtering in the scale of 619*640 μm^2 area. Clearly, the filtered surface roughness after CO_2 laser polishing is pretty low, around 10 nm, for an area larger than 0.5 mm^2. However, we should consider the waviness and forms on the surface. The surface shape changes near the sides, visible from the image above. Even if the image above is not reflecting the true scale (3-4 µm over 1 mm, <0.005), this small deformation will be critical for the propagation of light under that region in waveguide. Large scale surface characterization will be our next goal and investigated details in the following sections.

One pass large beam scan is applicable to our study as we aim to implement CO_2 laser polishing on nearly 1 mm silica rod pieces. The surface profiles after large beam one scan polishing can be seen in Figure 62. The laser PWM is adjusted to 80 % which delivers 47.5 W laser power on the stage. The working distance is adjusted roughly 70 mm, which gives 3.2 mm beam radius. However, the measured effective beam radius is around 2.4 mm. In the experiments the laser PWM is never increased more than 80 %, to keep the laser and the process safe as the laser is running for couple hours for the experiments. To understand the polishing effect the working distance is adjusted instead of changing the laser power. The change in PWM of laser makes the laser unstable again. Also adjusting working distance is quicker than changing the laser power. The working distance is changed with 250 micron increments on the experiments. Less than 1 mm change in working distance is enough for the experiment below. The x axis scanning speed is set between 0.05-0.1 mm/s. The filtered surface roughness is measured 8 nm over 557*663 μm^2 area. Deformation on sides is observed in this polishing technique as well.

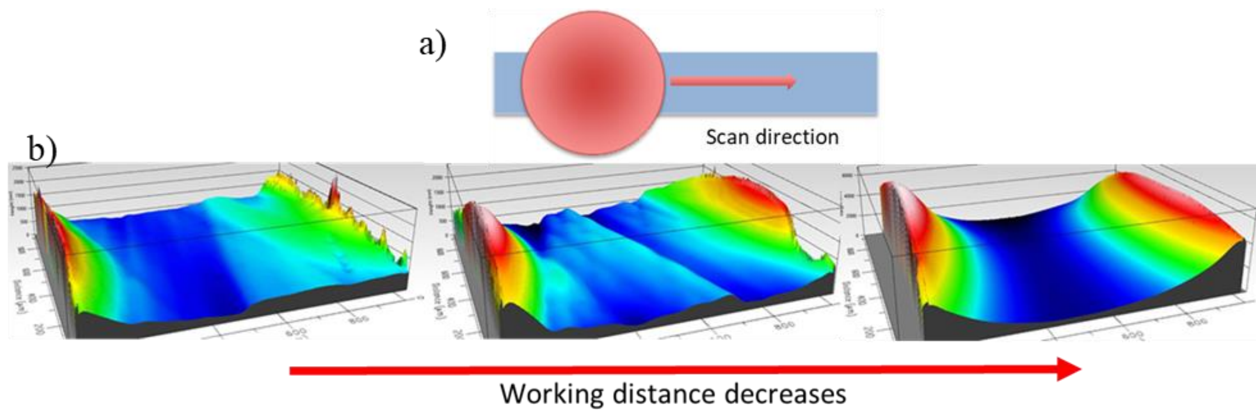

Figure 62. a) Large beam one scan and b) surface profile behaviors over various polishing levels.

The surface is deformed after laser polishing with large beam on x axis slow scan which is visible in the images above. The amplitude of surface high spatial frequency decreases as the amplitude of low spatial frequency increases. In the same manner, a better surface is obtained over the exposure while deformation increases in the meantime. The deformation at the edges is observed for this process as well. It is also seen that the deformation area on y axis is increased when compared the y axis raster scan as seen in Figure 63.

This means waviness or forms are introduced to the surface while the filtered roughness is decreasing. The deformation does not result from the Gaussian beam shape, the underlying reason is either Marangoni flow or fast cooling effect on melted surface.

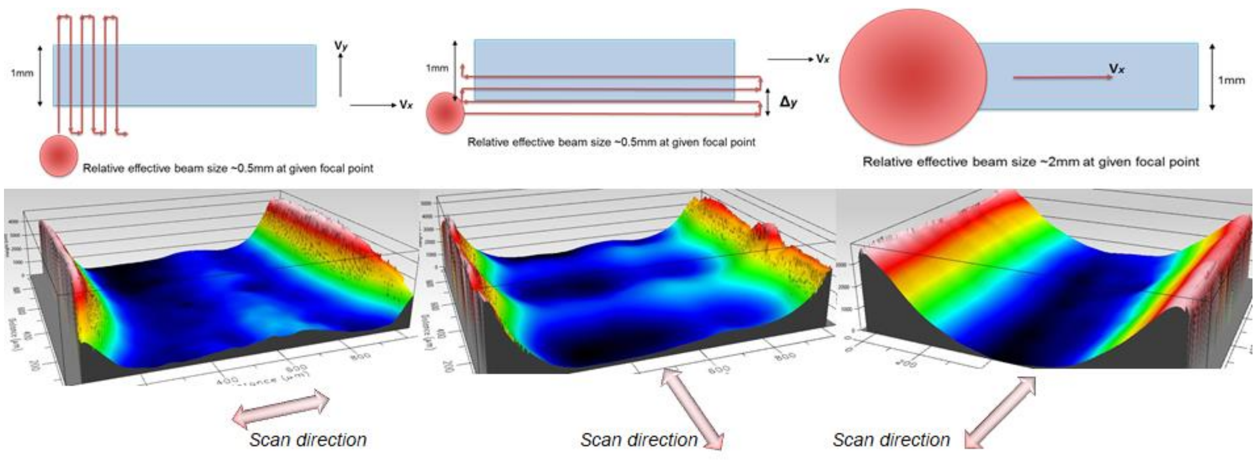

Figure 63. Surface profiles of three different polishing methods

All the polishing techniques tried will improve the surface roughness to some extent, and deformation will happen in all cases. Results reflect that high spikes or deformation is observed on the polished surface even if the filtered surface roughness is successfully decreased. To understand the reasons for the deformation, some conducted experiments will be conducted in the following subsection.

5.2 Deformation Analysis

In the case of perpendicular scan; the laser beam is scanned with one pass over the rod silica sample on y direction and gotten surface profile as presented in Figure 64. It is observed that the latter surface is deformed while the former entrance surface keeps its form. This could be explained with the regional temperature change on the sample surface during scanning. At the starting region, the surface does not heat well and not initiate the polishing process. But exit region has a high temperature that initiates both polishing and deformation in the same time. In the case of parallel scan; the laser beam is scanned at the edge of the silica rod through x direction as shown in Figure 64.

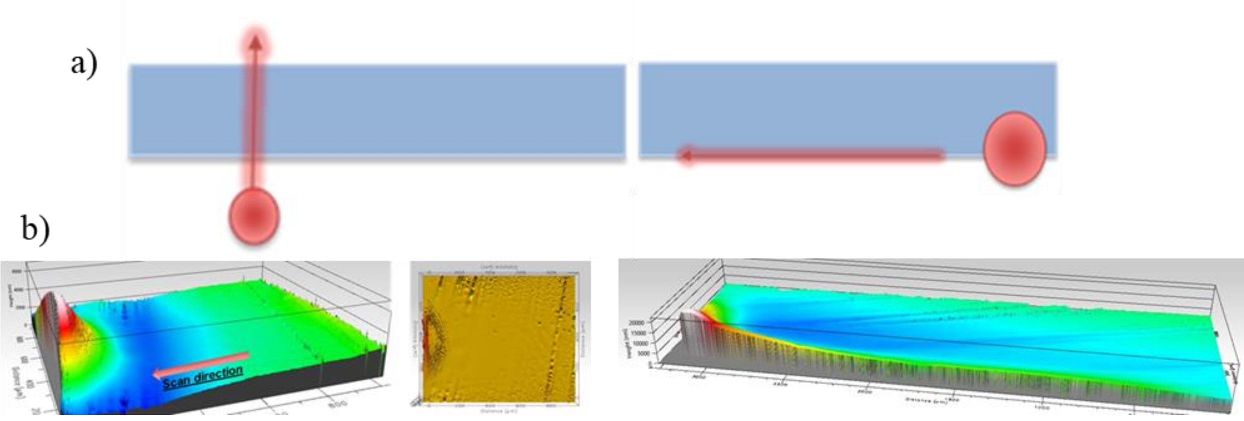

Figure 64. a) One pass laser scan on y and x axis b) surface profile after scan

As it is seen from the stitched surface profiles, in the initial position almost no deformation is observed while high deformation can be observed in the exit region. Increased temperature or the stored energy on the sample towards the exit region may be the reason behind. In the case of one point; the laser beam is shot at the edge of the sample as shown in following illustration.

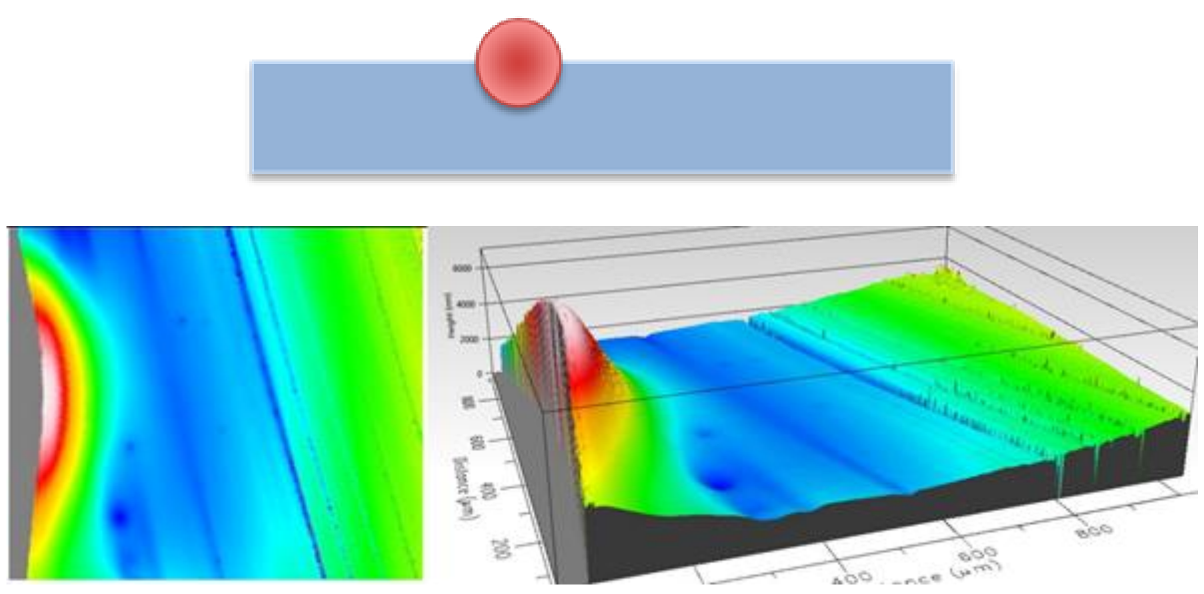

Figure 65. Laser beam effect on edge

Evident from the Figure 65, the deformation appears in the spot where the laser beam touches. To comprehend this phenomenon better we should understand the melt pool behavior at the edges. Because the outer parts of the melt pool have higher surface tension than the inner sections,[83] the molten metal is driven outwards within the melt pool until resolidification. Marangoni flow effect (thermocapillary effect) comes to the fore here.[84, 85] Marangoni flow can be described as a mass transfer along an interface between two fluids due to a gradient of the surface tension, which is resulted from hot and cold surface boundaries.

The studies on water droplets and thermocapillary force shows that there is a flow from hot side to cold. They found that the droplet migrates towards cold side.[86, 87] At ambient temperature, while the silica rod is heating, the surrounding of the sample is relatively cold according to sample surface which deforms the corner. The driving force takes place at this region that viscosity also plays a role.[88, 89]

5.3 Solutions Attempts

5.3.1 Masking

The purpose of this method is to minimize the laser exposure at the edge of the sample. Thus, it will eliminate the deformation on the edges. An aluminum closed capsule with aluminum mask on the silica rod is tested. The sample is placed in the slid and the cover mask is placed on the top of the sample. The process seems promising to prevent deformation at the edge. Nevertheless, there are some hurdles to come over like adjusting the mask dimensions and aligning the mask. A high precision control is needed. The surface profile of the polished sample under the mask layer is shown in Figure 66. As it can be seen from the profile, the polishing process is taken

placed closed to one side and with smaller effected area then size of the 1 mm silica surface. The cover mask requires fine dimensional adjustment with precise alignment.

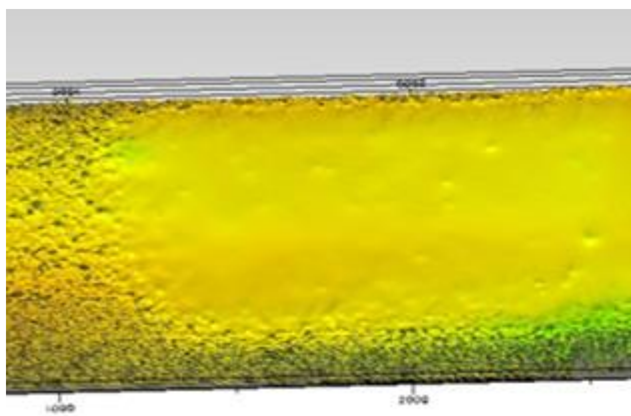

Figure 66. Surface profile of polished sample under mask layer.

5.3.2 Laser On/Off Timing with Pulse Wave

The heat and cool timings are tested to overcome the deformation. The pulse wave is generated with function generator to control the laser timing on and off state. The duty cycle and timing can be adjusted by changing the t1 and t2 timing as shown in Figure 67.

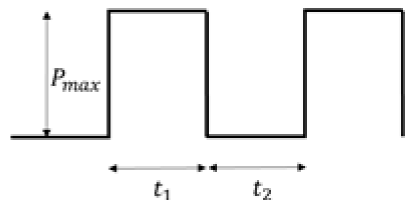

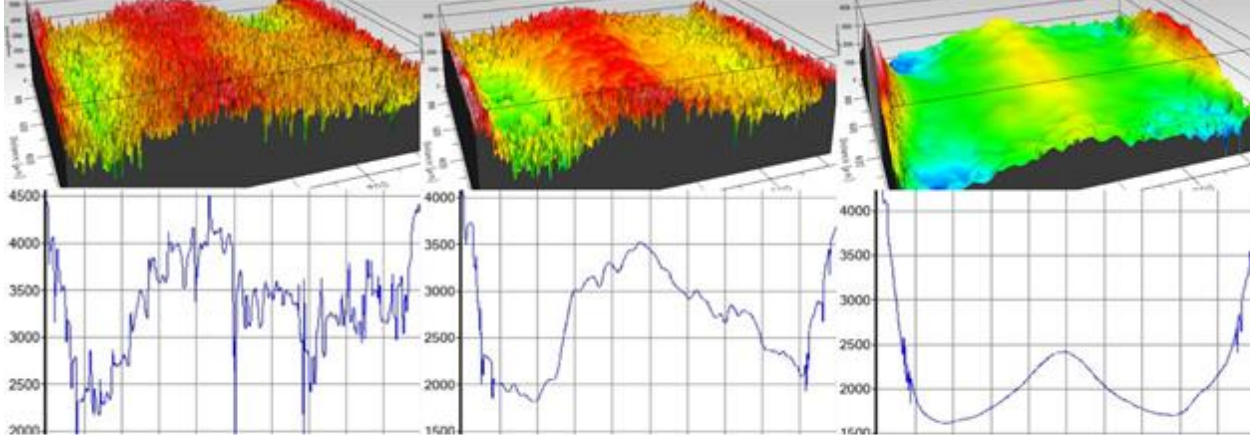

Figure 67. Surface change over exposure duration, square pulse timing (20 KHz, 80 % PWM, ~2 mm radius, Ton/off=150/50ms, 1sec, 3sec and 5sec)

Even with on/off timing, the surface gets deformities at sides under this given condition. The on/off timing should be adjusted accurately and it requires more tests and simulations for better surface quality. It is observed that when the off is time longer than 50 µs, the laser requires more time for on position and vice versa. The off timing could be too long for thermal cooling and might cause deformations on the sides. In the future experiments, these parameters are needed to optimize to control surface of the sample better. To eliminate the cooling effect, PWM pulse shape is controlled and it is explained in the following section.

5.3.3 Arbitrary Signal Generation

To minimize the cooling effect on silica sample, an arbitrary signal is generated as shown in Figure 68. The main aim of the experiment is to control the cooling time of the sample. The

sample surface temperature is tried to cool down slowly. The used parameters can be seen in Table 6.

Table 6. Laser polishing parameters for PWM control

Parameters	Description	Values
Pmax	Defined maximum power	34.5% PWM ~18.7W
Px	Adjusted secondary power level	25%, 50% and 75%*Pmax
t1	Time at max power	10 sec.
t2	Time for decreasing to Px	5, 10 and 20 sec.
t3	Time for decreasing to 0% power	60 sec.
D	Working distance under f	8 mm
A	Expected beam radius (1/e2) $a = 0.1508d + 0.171$	1.378 mm

The arbitrary waveform consists of a square wave followed by a slow cooling time. After the laser is ramped to 34.5% PWM, the laser is cooling time is varied to optimize surface qulity. The purpose of this experiment is to understand the reason of the corner deformation and generate some solution for that. Two step cool time is proposed. While the laser power is decerased fast at the initial phase, at the second phase the laser power is decreased slowly. The Px power is adjusted as 25, 50 and 75 percent of maximum power with various timing. At the first phase, the time is changed from 5 sec to 20 sec. The time for second phase, t3 is adjusted to 1 min.

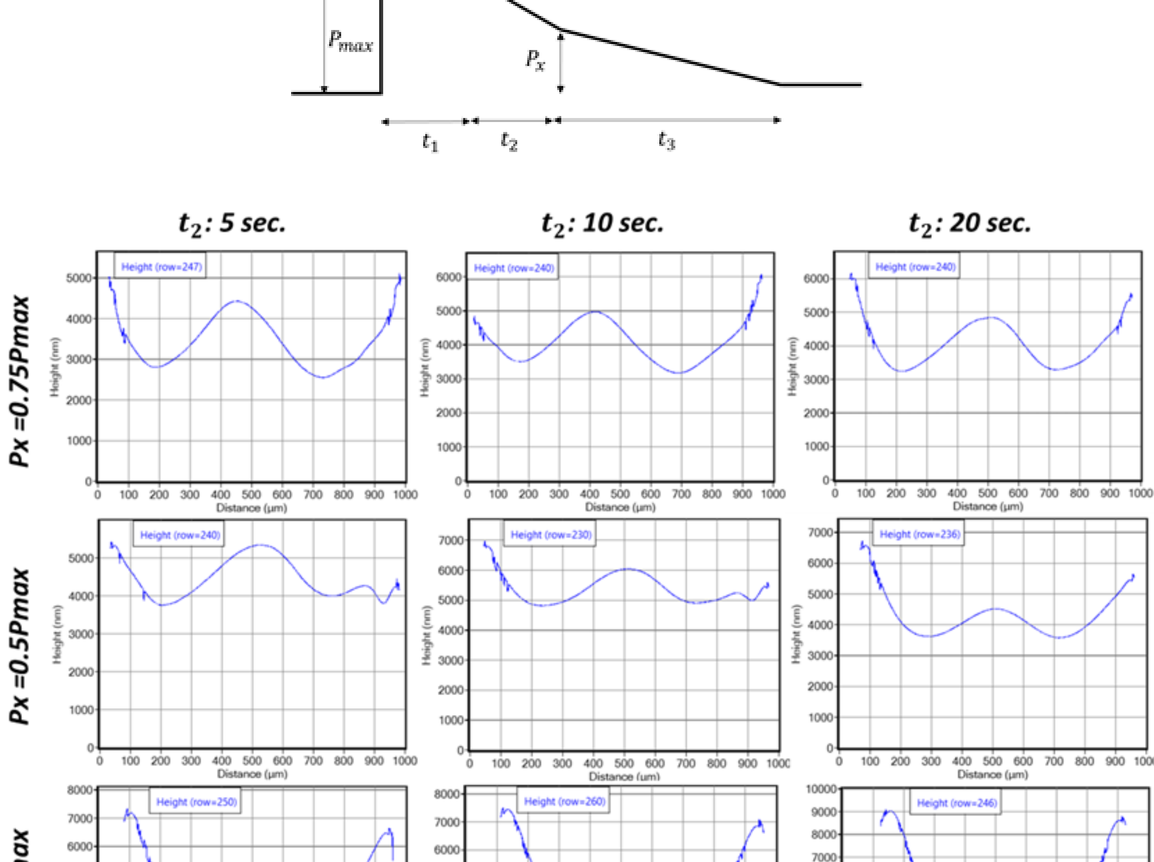

Figure 68. Surface profiles of samples polished with arbitrary PWM signal

Some of the test parameter results are represented in Figure 68. It should be taken into account for a better interpretation of the surface profile that the sample used had 2 µm bump before applying any process. This test reveals that the cooling process happens even when the laser is on. Because the laser heats the sample from top, sides are exposed to the cooling process which leads

the side deformation. Even after optimization of the parameters we may still get deformation due to side cooling affect. Following experiments are made to understand the heat effect on the sample.

5.3.4 Substrate Heating Effect

By heating the sample from bottom, the minimizing the thermal difference between the seated sample surface and the substrate, and the hot sample and surrounding medium. Hot plate is placed under the substrate under the silica rod. The hotplate is heated to 400°C and 2 mm thick Tungsten plate is chosen as the substrate since it has high melting point, high tensile strength and low thermal expansion. The process parameters can be seen in Table 7.

Table 7. CO_2 laser polishing parameters for heat effect study

Parameters	***Values***	
Pwm (P)	35 % ~18.7 W	80 % ~47.5 W
Time	10-20 sec	
Hot plate temp	20-400 °C	
Substrate	2 mm tungsten carbide rod	
Working distance (d) ***exp. beam radius (a)***	d=59.5 mm & a=1.6 mm for cold d=61 mm & a=1.83 mm for hot	d=67 mm & a=2.73 mm for cold d=70 mm & a=3.19 mm for hot

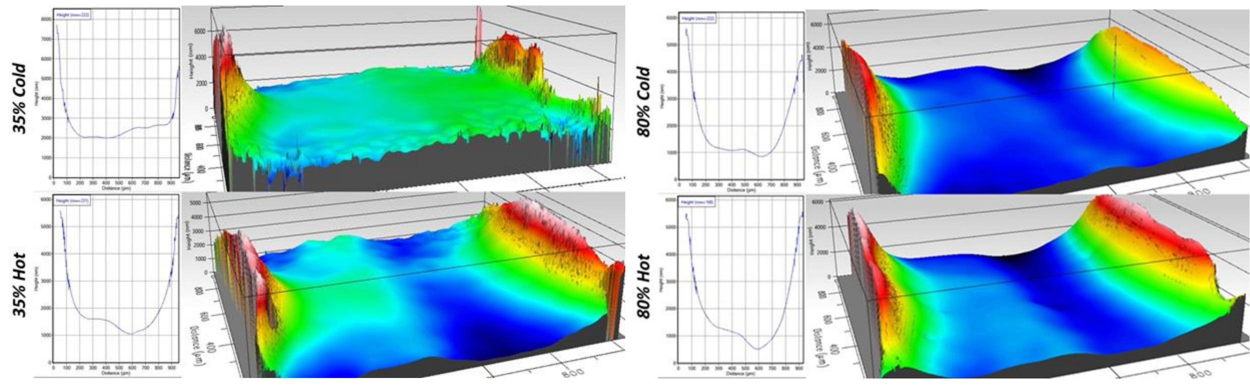

Figure 69. Surface profile of polished sample under 35% and 80% PWM with cold and hot substrate

Surface profiles of two polished samples at 35% PWM with & without heating with the hotplate. In line with the result, the surface profiles are nearly same. An increase in the temperature was expected to cause better results but the profiles does not support the idea. The ambient temperature around the silica rod may not get enough heat, and this may be underlying reason. To understand the temperature effect better, different sets of parameters are tried on the following tests. It is wise to increase the beam size to eliminate the Gaussian beam effect on the 1 mm rod.

No substrate heating effect is observed at 80% PWM similarly to the previous test for 35% PWM. Again, the surrounding temperature around the polished silica rod may not be high enough, and there is a temperature difference especially at the side corners accordingly.

5.3.5 Substrate Material Effect

To conduct a comparison, Tungsten carbide and Silica plate are determined as substrates to place under the silica rod due to their absorption values at given 10.6 µm wavelength. Tungsten carbide is highly reflective while silica is highly absorptive at given CO_2 wavelength. The result presented in Figure 71 show that the deformation at the sides are minimum when we used the silica

plate as a substrate. The deformation is decreased from nearly 5 µm to 2 µm at 35% PWM system setup. Another test with a larger beam is applied to better analyze this effect. Substrate material effect is investigated with large beam with parameters given in Table 8.

Table 8. CO_2 laser polishing parameters for substrate material effect

Parameters	***Values***	
PWM	35 % ~18.7 W	80 % ~47.5 W
Time	10-20 sec	
Hot plate temp	400 °C	
Substrate	2 mm tungsten carbide (WC) rod & 1 mm fused silica	
Working distance (d) ***exp. beam radius (a)***	d=61 mm & a=1.83 mm on WC d=64 mm & a=2.28 mm on Silica	d=70 mm & a=3.19 mm on WC d=72 mm & a=3.49 mm on Silica

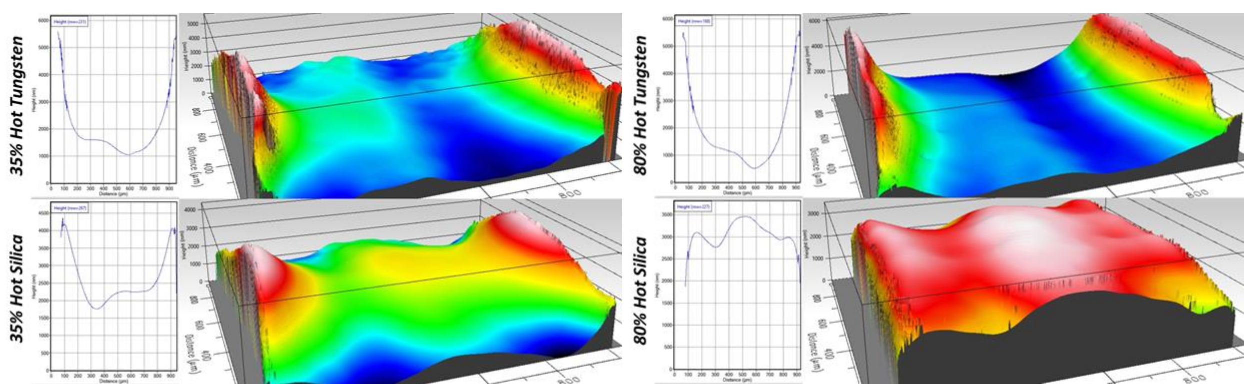

Figure 70. Surface profiles of two polished samples at 35% and 80% PWM with tungsten carbide and silica substrate on hot plate

The surface deformation at sides are decreased dramatically with 80% hot silica under given conditions. The deformities at sides disappeared as shown in Figure 70. When we compare the result from 35% PWM case, the surface improved much better.

As we increased the beam size on the silica rod and increased the power accordingly, more power is delivered to the bottom substrate. While the rough Tungsten carbide surface reflects that power, the Silica plate absorbs it and corresponds to an external heat source. The conductive and convectional heat transfer makes a quite hot environment for polishing with the absorption of laser energy in silica plate. As a result of the minimum thermal difference we are getting better surface quality. While the top surface get polished, the deformation on the side surface also investigated. While there is a bend at the corners, the sidewall, non-polished side, keeps its original surface. The non-polished side of the polished sample can be seen in Figure 71 to better understand.

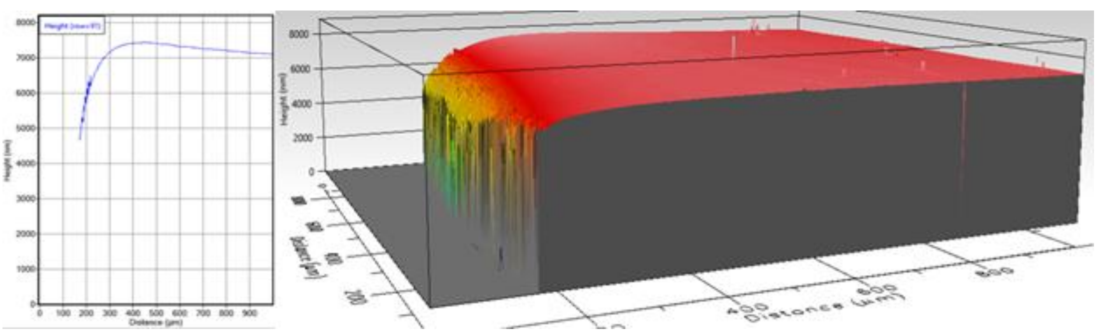

Figure 71. Non-polished side surface profile of polished sample to observe the corners

5.4 Long Silica Rod Polished Surface

The laser PWM is adjusted to 80% which delivers 47.5 W power to the stages. The working distance is kept between 69 mm and 73 mm given in Table 9. The working distance is very

important and sensitive for polishing. The ambient temperature and the bottom heating is one of the important factors that affects polishing. Hot plate is used and set to 400°C. At the corresponding working distance, the spot diameter of the laser at the silica rod scanned surface is changed between 3.04 mm and 3.64 mm. 70 mm long silica rod placed on a silica substrate and the long silica rod polishing experiment parameters and results can be seen below. No upward deformation but rounding is observed on the edges of the sample. Achieved Gaussian filtered surface roughness is 6.4 nm over 0.5 mm x 2.66 mm surface area as seen in Figure 72.

Table 9. CO_2 laser polishing parameters for long silica rod polishing

Parameters	***Values***
PWM &P	80% ~47.5 W on the sample
Hot plate temp	400C
Substrate	1 mm silica plate
Working distance (d) ***exp. beam radius (a)***	d= between 69-73 mm a = 3.04-3.64 mm respectively
Speed	0.05 mm/s

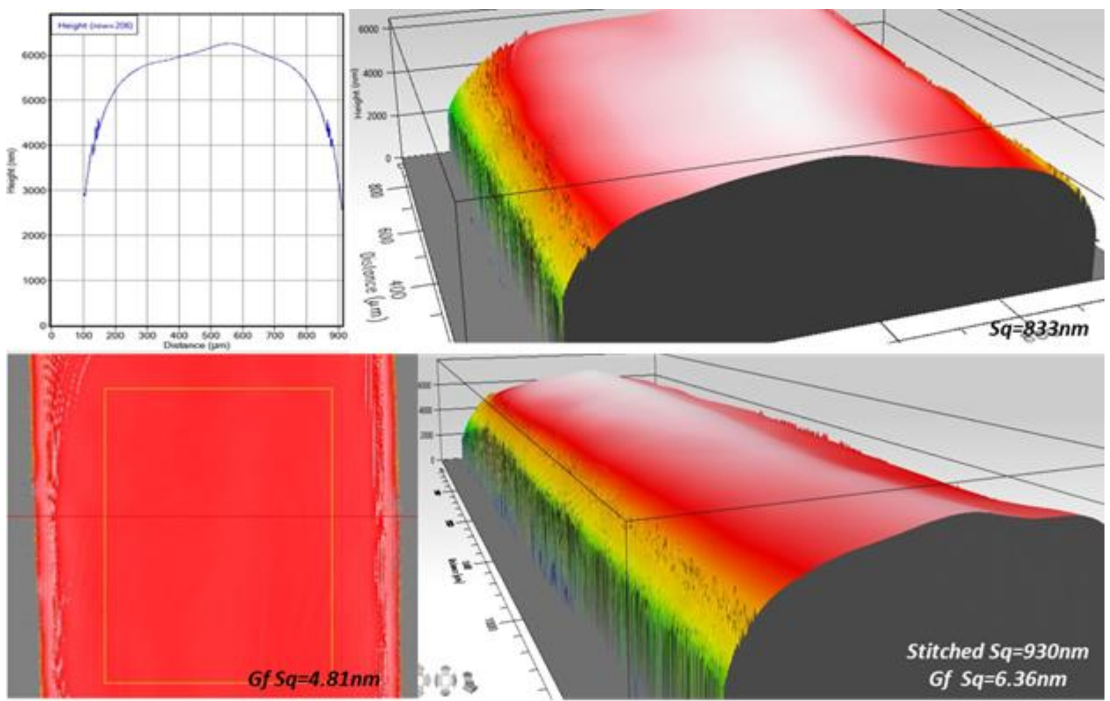

Figure 72. 70 mm silica sample surface profiles

6. SUMMARY

Renewable energy has become a must for our world in the modern day dominated with ever-growing technologies. Solar energy, the best candidate as a renewable energy source, is in high demand. Regular PV cells to concentrate the sunlight still suffer from low efficiency, the commercially available PV cells has less than 20% efficiency. This drawback has brought about the need for high efficiency cells. Multijunction solar cells has a theoretical efficiency limit of 87%; however, they are expensive. Studies are conducted to further improve the efficiency and lower the prices with the improvements on the semiconductor industry. High concentrator photovoltaic system is proposed as a cost effective alternative. Different from the conventional CPV systems using lenses and mirrors to concentrate the sunlight HCPV requires high vertical distance leading some challenges like wiring many separated cells, localized heat, cooling problem and low concentration. Waveguiding as a secondary concentrator offers a solution to overcome these challenges. For high efficiency purposes, silica is used as the waveguiding material. There is no commercially available technique to fabricate 3D silica waveguides yet.

In this dissertation, a new approach FLICE is analyzed and performed to demonstrate the feasibility of 3D waveguide fabrication. Short pulse laser irradiation in transparent material is studied with nonlinear absorption process as the first step once short pulse fast laser cutting is decided to use in processing silica. Femtosecond direct writing is applied afterwards to see the applicability. Wet chemical etching and selectivity is studied as the process involves etching as the second step.

Having setup the femtosecond laser and gained the laser control, initial tests are performed. High surface quality is crucial for the waveguide to minimize the scattering loss and satisfy the TIR condition. Surface roughness is investigated in the laser processed sample by utilizing various surface metrology tools. Later, nanograting formation and selectivity are optimized by consecutive tests evaluating different laser parameters and combinations of these parameters. These parameters include writing speed, polarization, pulse width, pulse energy power and z increments. 2D plane etching is examined to release the irradiated silica plate. High surface quality, direction independence and high speed manufacturing is achieved. Other process capabilities and accuracy of process are presented with complex 3D fabrications like aspheric lens and tapered light pipe.

FLICE processed sample undergoes to CO_2 laser polishing process to get a smoother surface. Before choosing CO_2 laser polishing technique, all glass polishing techniques have been evaluated. Since deformations are observed after polishing process, several solution attempts have been done. Masking, laser on/off timing with pulse wave, arbitrary signal generation, heating the substrate and using alternative substrate material have been tried and results are presented.

As a result, in overall: A new approach for getting light pipe from silica plate with complex surfaces is achieved and proved to be applicable for mass production. Tapered light pipes with up to 7x concentration factor with a 45° angled input facet is successfully fabricated. Direct writing speed up to 1.25 m/s (N = 3.2) with Sq of 477 nm has been achieved. Surface quality without post processing less than Sq = 63.4 nm, Sq_gf = 21.8 nm. 6.4 nm surface RMS roughness of silica samples at a given area of 0.5 mm x 2.66 mm has been accomplished. Prototype of our overall HCPV design and measurements of the final sidewall surface are depicted in Figure 73.

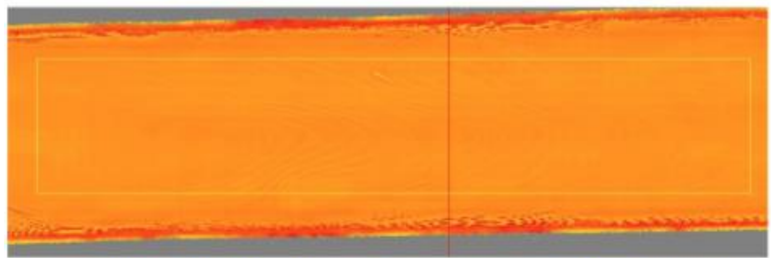

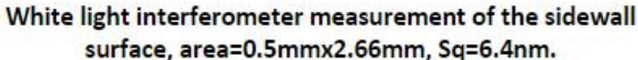

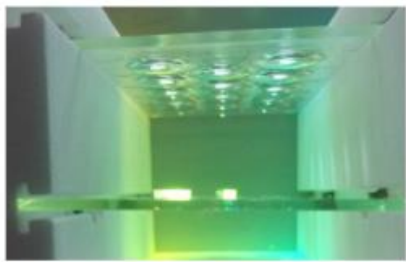

Prototype using a 3x5 lens array

Figure 73. Polished sidewall surface and proposed prototype

REFERENCES

[1] "Theoretical Limits of Photovoltaic Conversion and New-Generation Solar Cells," in *Handbook of Photovoltaic Science and Engineering*, ed.

[2] G. R. Whitfield, R. W. Bentley, C. K. Weatherby, A. C. Hunt, H. D. Mohring, F. H. Klotz*, et al.*, "The development and testing of small concentrating PV systems," *Solar Energy,* vol. 67, pp. 23-34, 1999/07/01/ 1999.

[3] M. Khamooshi, H. Salati, F. Egelioglu, A. Hooshyar Faghiri, J. Tarabishi, and S. Babadi, "A Review of Solar Photovoltaic Concentrators," *International Journal of Photoenergy,* vol. 2014, p. 17, 2014.

[4] K. Shanks, S. Senthilarasu, and T. K. Mallick, "Optics for concentrating photovoltaics: Trends, limits and opportunities for materials and design," *Renewable and Sustainable Energy Reviews,* vol. 60, pp. 394-407, 2016/07/01/ 2016.

[5] J. H. Karp, E. J. Tremblay, and J. E. Ford, "Planar micro-optic solar concentrator," *Optics Express,* vol. 18, pp. 1122-1133, 2010/01/18 2010.

[6] K. Arizono, R. Amano, Y. Okuda, and I. Fujieda, "A concentrator photovoltaic system based on branched planar waveguides," in *SPIE Solar Energy + Technology*, 2012, p. 8.

[7] Y. Liu, R. Huang, and C. K. Madsen, "Design of a lens-to-channel waveguide system as a solar concentrator structure," *Optics Express,* vol. 22, pp. A198-A204, 2014/03/10 2014.

[8] S. Nikumb, Q. Chen, C. Li, H. Reshef, H. Y. Zheng, H. Qiu*, et al.*, "Precision glass machining, drilling and profile cutting by short pulse lasers," *Thin Solid Films,* vol. 477, pp. 216-221, 4/22/ 2005.

[9] S. Nisar, L. Li, and M. A. Sheikh, "Laser glass cutting techniques—A review," *Journal of Laser Applications,* vol. 25, p. 042010, 2013.

[10] K. L. Wlodarczyk, A. Brunton, P. Rumsby, and D. P. Hand, "Picosecond laser cutting and drilling of thin flex glass," *Optics and Lasers in Engineering,* vol. 78, pp. 64-74, 2016/03/01/ 2016.

[11] K. Itoh, W. Watanabe, S. Nolte, and C. B. Schaffer, "Ultrafast Processes for Bulk Modification of Transparent Materials," *MRS Bulletin,* vol. 31, pp. 620-625, 2006.

[12] V. R. Bhardwaj, E. Simova, P. B. Corkum, D. M. Rayner, C. Hnatovsky, R. S. Taylor*, et al.*, "Femtosecond laser-induced refractive index modification in multicomponent glasses," *Journal of Applied Physics,* vol. 97, p. 083102, 2005.

[13] R. Taylor, C. Hnatovsky, and E. Simova, "Applications of femtosecond laser induced self-organized planar nanocracks inside fused silica glass," *Laser & Photonics Reviews,* vol. 2, pp. 26-46, 2008.

[14] C. Hnatovsky, R. S. Taylor, P. P. Rajeev, E. Simova, V. R. Bhardwaj, D. M. Rayner*, et al.*, "Pulse duration dependence of femtosecond-laser-fabricated nanogratings in fused silica," *Applied Physics Letters,* vol. 87, p. 014104, 2005.

[15] H. Huang, L.-M. Yang, and J. Liu, "Femtosecond fiber laser direct writing of optical waveguide in glasses," in *SPIE Optical Engineering + Applications*, 2011, p. 8.

[16] K. Sugioka and Y. Cheng, "Ultrafast lasers—reliable tools for advanced materials processing," *Light: Science &Amp; Applications,* vol. 3, p. e149, 04/11/online 2014.

[17] K. Sugioka, J. Xu, D. Wu, Y. Hanada, Z. Wang, Y. Cheng*, et al.*, "Femtosecond laser 3D micromachining: a powerful tool for the fabrication of microfluidic, optofluidic, and electrofluidic devices based on glass," *Lab on a Chip,* vol. 14, pp. 3447-3458, 2014.

[18] R. Paschotta, J. Nilsson, A. C. Tropper, and D. C. Hanna, "Ytterbium-doped fiber amplifiers," *IEEE Journal of Quantum Electronics,* vol. 33, pp. 1049-1056, 1997.

[19] P. Alberto, C. Y. A. Raymond, K. Heungsoo, A. C. Nicholas, and A. M. Scott, "Laser 3D micro-manufacturing," *Journal of Physics D: Applied Physics,* vol. 49, p. 223001, 2016.

[20] L. J. Jiang, S. Maruo, R. Osellame, W. Xiong, J. H. Campbell, and Y. F. Lu, "Femtosecond laser direct writing in transparent materials based on nonlinear absorption," *MRS Bulletin,* vol. 41, pp. 975-983, 2016.

[21] N. Bloembergen, "Laser-material interactions; fundamentals and applications," *AIP Conference Proceedings,* vol. 288, pp. 3-10, 1993.

[22] H. A. Haus, "Mode-locking of lasers," *IEEE Journal of Selected Topics in Quantum Electronics,* vol. 6, pp. 1173-1185, 2000.

[23] R. Ganeev, A. Ryasnyanskiy, B. Palpant, and S. Debrus, *Third-Order Nonlinearities of B12GeO20 Crystal Measured by Nanosecond Radiation* vol. 97, 2005.

[24] R. R. Gattass and E. Mazur, "Femtosecond laser micromachining in transparent materials," *Nature Photonics,* vol. 2, p. 219, 04/01/online 2008.

[25] B. S. Chris, B. André, and M. Eric, "Laser-induced breakdown and damage in bulk transparent materials induced by tightly focused femtosecond laser pulses," *Measurement Science and Technology,* vol. 12, p. 1784, 2001.

[26] A. Q. Wu, I. H. Chowdhury, and X. Xu, "Femtosecond laser absorption in fused silica: Numerical and experimental investigation," *Physical Review B,* vol. 72, p. 085128, 08/22/ 2005.

[27] C. Hnatovsky, R. S. Taylor, E. Simova, V. R. Bhardwaj, D. M. Rayner, and P. B. Corkum, "Polarization-selective etching in femtosecond laser-assisted microfluidic channel fabrication in fused silica," *Optics Letters,* vol. 30, pp. 1867-1869, 2005/07/15 2005.

[28] C. Ross, D. G. MacLachlan, D. Choudhury, and R. R. Thomson, "Towards optical quality micro-optic fabrication by direct laser writing and chemical etching," 2017, pp. 100940V-100940V-15.

[29] T. V. Roberts, M. Lawless, C. C. Chan, M. Jacobs, D. Ng, S. J. Bali, *et al.*, "Femtosecond laser cataract surgery: technology and clinical practice," *Clinical & Experimental Ophthalmology,* vol. 41, pp. 180-186, 2013.

[30] C. L. Hoy, N. J. Durr, P. Chen, W. Piyawattanametha, H. Ra, O. Solgaard, *et al.*, "Miniaturized probe for femtosecond laser microsurgery and two-photon imaging," *Optics express,* vol. 16, pp. 9996-10005, 2008.

[31] Q. H. Gong, S. Wang, T. Q. Zhang, W. Huang, and H. Yang, *Femtosecond Laser Spectroscopy and Applications*, 2001.

[32] G. C. Franssen, H. M. A. Schleijpen, J. C. v. d. Heuvel, H. Buersing, B. Eberle, and D. Walter, "Femtosecond lasers for countermeasure applications," in *SPIE Security + Defence*, 2009, p. 9.

[33] D. R. Alexander, D. Doerr, L. Jianchao, and Z. Haifeng, "Femtosecond laser propagation through aerosol clouds for improved communications and remote sensing applications," in *IGARSS 2004. 2004 IEEE International Geoscience and Remote Sensing Symposium*, 2004, pp. 3880-3883 vol.6.

[34] S. Maruo, O. Nakamura, and S. Kawata, "Three-dimensional microfabrication with two-photon-absorbed photopolymerization," *Optics Letters,* vol. 22, pp. 132-134, 1997/01/15 1997.

[35] M. Malinauskas, A. Žukauskas, S. Hasegawa, Y. Hayasaki, V. Mizeikis, R. Buividas, *et al.*, "Ultrafast laser processing of materials: from science to industry," *Light: Science &Amp; Applications,* vol. 5, p. e16133, 08/12/online 2016.

[36] B.-B. Xu, Y.-L. Zhang, H. Xia, W.-F. Dong, H. Ding, and H.-B. Sun, "Fabrication and multifunction integration of microfluidic chips by femtosecond laser direct writing," *Lab on a Chip,* vol. 13, pp. 1677-1690, 2013.

[37] K. M. Davis, K. Miura, N. Sugimoto, and K. Hirao, "Writing waveguides in glass with a femtosecond laser," *Optics Letters,* vol. 21, pp. 1729-1731, 1996/11/01 1996.

[38] M. Ams, G. D. Marshall, P. Dekker, J. A. Piper, and M. J. Withford, "Ultrafast laser written active devices," *Laser & Photonics Reviews,* vol. 3, pp. 535-544, 2009.

[39] M. Li, K. Mori, M. Ishizuka, X. Liu, Y. Sugimoto, N. Ikeda*, et al.*, "Photonic bandpass filter for 1550 nm fabricated by femtosecond direct laser ablation," *Applied Physics Letters,* vol. 83, pp. 216-218, 2003.

[40] J. Lin, Y. Xu, Z. Fang, M. Wang, J. Song, N. Wang*, et al.*, "Fabrication of high-Q lithium niobate microresonators using femtosecond laser micromachining," *Scientific Reports,* vol. 5, p. 8072, 01/28/online 2015.

[41] P. Ettl, B. E. Schmidt, M. Schenk, I. Laszlo, and G. Haeusler, "Roughness parameters and surface deformation measured by coherence radar," in *International Conference on Applied Optical Metrology*, 1998, p. 8.

[42] E. A. Donley, T. P. Heavner, F. Levi, M. O. Tataw, and S. R. Jefferts, "Double-pass acousto-optic modulator system," *Review of Scientific Instruments,* vol. 76, p. 063112, 2005.

[43] K. Sugioka and Y. Cheng, "Femtosecond laser three-dimensional micro- and nanofabrication," *Applied Physics Reviews,* vol. 1, p. 041303, 2014.

[44] K. Sugioka, H. Sun, M. Masuda, K. Midorikawa, and K. Shihoyama, *3D microstructuring of glass by femtosecond laser direct-writing for micro-TAS application* vol. 5399, 2004.

[45] H. Huang, L.-M. Yang, and J. Liu, "Micro-hole drilling and cutting using femtosecond fiber laser," 2014, p. 9.

[46] A. Marcinkevičius, S. Juodkazis, M. Watanabe, M. Miwa, S. Matsuo, H. Misawa*, et al.*, "Femtosecond laser-assisted three-dimensional microfabrication in silica," *Optics Letters,* vol. 26, pp. 277-279, 2001/03/01 2001.

[47] Y. Bellouard, A. Said, M. Dugan, and P. Bado, "Fabrication of high-aspect ratio, micro-fluidic channels and tunnels using femtosecond laser pulses and chemical etching," *Optics Express,* vol. 12, pp. 2120-2129, 2004/05/17 2004.

[48] C. Hnatovsky, R. S. Taylor, E. Simova, P. P. Rajeev, D. M. Rayner, V. R. Bhardwaj*, et al.*, "Fabrication of microchannels in glass using focused femtosecond laser radiation and selective chemical etching," *Applied Physics A,* vol. 84, pp. 47-61, July 01 2006.

[49] K. C. Vishnubhatla, N. Bellini, R. Ramponi, G. Cerullo, and R. Osellame, "Shape control of microchannels fabricated in fused silica by femtosecond laser irradiation and chemical etching," *Optics Express,* vol. 17, pp. 8685-8695, 2009/05/11 2009.

[50] M. Toofan and J. Toofan, "Chapter 5 - A Brief Review of the Cleaning Process for Electronic Device Fabrication," in *Developments in Surface Contamination and Cleaning*, R. Kohli and K. L. Mittal, Eds., ed Oxford: William Andrew Publishing, 2015, pp. 185-212.

[51] F. He, Y. Liao, J. Lin, J. Song, L. Qiao, Y. Cheng*, et al.*, "Femtosecond Laser Fabrication of Monolithically Integrated Microfluidic Sensors in Glass," *Sensors,* vol. 14, p. 19402, 2014.

[52] D. Choudhury, J. R. Macdonald, and A. K. Kar, "Ultrafast laser inscription: perspectives on future integrated applications," *Laser & Photonics Reviews,* vol. 8, pp. 827-846, 2014.

[53] X. Yu, Y. Liao, F. He, B. Zeng, Y. Cheng, Z. Xu*, et al.*, "Tuning etch selectivity of fused silica irradiated by femtosecond laser pulses by controlling polarization of the writing pulses," *Journal of Applied Physics,* vol. 109, p. 053114, 2011.

[54] M. Beresna, M. Gecevičius, and P. G. Kazansky, "Polarization sensitive elements fabricated by femtosecond laser nanostructuring of glass [Invited]," *Optical Materials Express,* vol. 1, pp. 783-795, 2011/08/01 2011.

[55] S. Rajesh and Y. Bellouard, "Towards fast femtosecond laser micromachining of fused silica: The effect of deposited energy," *Optics Express,* vol. 18, pp. 21490-21497, 2010/09/27 2010.

[56] S. Kiyama, S. Matsuo, S. Hashimoto, and Y. Morihira, "Examination of etching agent and etching mechanism on femotosecond laser microfabrication of channels inside vitreous silica substrates†," *The Journal of Physical Chemistry C,* vol. 113, pp. 11560-11566, 2009.

[57] M. Hermans, J. Gottmann, and F. Riedel, "Selective, Laser-Induced Etching of Fused Silica at High Scan-Speeds Using KOH," *Journal of Laser Micro / Nanoengineering,* vol. 9, pp. 126-131, 06// 2014.

[58] Y. F. Dufrêne, "Atomic Force Microscopy, a Powerful Tool in Microbiology," *Journal of Bacteriology,* vol. 184, pp. 5205-5213, 2002.

[59] P. de Groot and L. Deck, "Surface Profiling by Analysis of White-light Interferograms in the Spatial Frequency Domain," *Journal of Modern Optics,* vol. 42, pp. 389-401, 1995/02/01 1995.

[60] Y. Shimotsuma, P. G. Kazansky, J. Qiu, and K. Hirao, "Self-Organized Nanogratings in Glass Irradiated by Ultrashort Light Pulses," *Physical Review Letters,* vol. 91, p. 247405, 12/11/ 2003.

[61] Q. Sun, F. Liang, R. Vallée, and S. L. Chin, "Nanograting formation on the surface of silica glass by scanning focused femtosecond laser pulses," *Optics Letters,* vol. 33, pp. 2713-2715, 2008/11/15 2008.

[62] J. Canning, M. Lancry, K. Cook, A. Weickman, F. Brisset, and B. Poumellec, "Anatomy of a femtosecond laser processed silica waveguide [Invited]," *Optical Materials Express,* vol. 1, pp. 998-1008, 2011/09/01 2011.

[63] K. Mishchik, G. Cheng, G. Huo, I. M. Burakov, C. Mauclair, A. Mermillod-Blondin*, et al.*, "Nanosize structural modifications with polarization functions in ultrafast laser irradiated bulk fused silica," *Optics Express,* vol. 18, pp. 24809-24824, 2010/11/22 2010.

[64] N. I. Chkhalo, S. A. Churin, M. S. Mikhaylenko, A. E. Pestov, V. N. Polkovnikov, N. N. Salashchenko*, et al.*, "Ion-beam polishing of fused silica substrates for imaging soft x-ray and extreme ultraviolet optics," *Applied Optics,* vol. 55, pp. 1249-1256, 2016/02/20 2016.

[65] C. Gerhard, T. Weihs, A. Luca, S. Wieneke, and W. Viöl, *Polishing of optical media by dielectric barrier discharge inert gas plasma at atmospheric pressure* vol. 8, 2013.

[66] W.-B. Kim, E. Nam, B.-K. Min, D.-S. Choi, T.-J. Je, and E.-C. Jeon, "Material removal of glass by magnetorheological fluid jet," *International Journal of Precision Engineering and Manufacturing,* vol. 16, pp. 629-637, April 01 2015.

[67] M. Kanaoka, C. Liu, K. Nomura, M. Ando, H. Takino, Y. Fukuda*, et al.*, "Figuring and smoothing capabilities of elastic emission machining for low-thermal-expansion glass optics," *Journal of Vacuum Science & Technology B: Microelectronics and Nanometer Structures Processing, Measurement, and Phenomena,* vol. 25, pp. 2110-2113, 2007.

[68] F. Laguarta, N. Lupon, and J. Armengol, "Optical glass polishing by controlled laser surface-heat treatment," *Applied optics,* vol. 33, pp. 6508-6513, 1994.

[69] J. Hildebrand, K. Hecht, J. Bliedtner, and H. Müller, "Laser Beam Polishing of Quartz Glass Surfaces," *Physics Procedia,* vol. 12, pp. 452-461, 2011/01/01/ 2011.

[70] C. Weingarten, A. Schmickler, E. Willenborg, K. Wissenbach, and R. Poprawe, "Laser polishing and laser shape correction of optical glass," *Journal of Laser Applications,* vol. 29, p. 011702, 2017.

[71] J. N. Desai, "Advances and processes in precision glass polishing techniques," *Report of the University of Florida,* 2009.

[72] C. Weingarten, E. Uluz, A. Schmickler, K. Braun, E. Willenborg, A. Temmler*, et al.*, "Glass processing with pulsed CO2 laser radiation," *Applied Optics,* vol. 56, pp. 777-783, 2017/02/01 2017.

[73] J. Hildebrand, K. Hecht, J. Bliedtner, and H. Müller, "Advanced Analysis of Laser Beam Polishing of Quartz Glass Surfaces," *Physics Procedia,* vol. 39, pp. 277-285, 2012/01/01/ 2012.

[74] A. D. McLachlan and F. P. Meyer, "Temperature dependence of the extinction coefficient of fused silica for CO2 laser wavelengths," *Applied Optics,* vol. 26, pp. 1728-1731, 1987/05/01 1987.

[75] C. Buerhop, B. Blumenthal, R. Weissmann, N. Lutz, and S. Biermann, "Glass surface treatment with excimer and CO 2 lasers," *Applied surface science,* vol. 46, pp. 430-434, 1990.

[76] H. Y. Wang, D. L. Bourell, and J. J. Beaman, "Laser polishing of silica slotted rods," *Materials Science and Technology,* vol. 19, pp. 382-387, 2003/03/01 2003.

[77] S. Heidrich, E. Willenborg, C. Weingarten, and A. Temmler, "Laser polishing and laser form correction of fused silica optics," *Materialwissenschaft und Werkstofftechnik,* vol. 46, pp. 668-674, 2015.

[78] P. A. Temple, W. H. Lowdermilk, and D. Milam, "Carbon dioxide laser polishing of fused silica surfaces for increased laser-damage resistance at 1064 nm," *Applied Optics,* vol. 21, pp. 3249-3255, 1982/09/15 1982.

[79] K. M. Nowak, H. J. Baker, and D. R. Hall, "Efficient laser polishing of silica micro-optic components," *Applied Optics,* vol. 45, pp. 162-171, 2006/01/01 2006.

[80] A. Richmann, E. Willenborg, and K. Wissenbach, "Laser Polishing of Fused Silica," in *International Optical Design Conference and Optical Fabrication and Testing*, Jackson Hole, Wyoming, 2010, p. OTuC2.

[81] J. M. Elson and J. M. Bennett, "Calculation of the power spectral density from surface profile data," *Applied Optics,* vol. 34, pp. 201-208, 1995/01/01 1995.

[82] A. Duparré, J. Ferre-Borrull, S. Gliech, G. Notni, J. Steinert, and J. M. Bennett, "Surface characterization techniques for determining the root-mean-square roughness and power spectral densities of optical components," *Applied Optics,* vol. 41, pp. 154-171, 2002/01/01 2002.

[83] Y. Hou, B. Xue, S. Guan, S. Feng, Z. Geng, X. Sui*, et al.*, "Temperature-controlled directional spreading of water on a surface with high hysteresis," *Npg Asia Materials,* vol. 5, p. e77, 12/20/online 2013.

[84] F. E. Pfefferkorn, N. A. Duffie, X. Li, M. Vadali, and C. Ma, "Improving surface finish in pulsed laser micro polishing using thermocapillary flow," *CIRP Annals,* vol. 62, pp. 203-206, 2013/01/01/ 2013.

[85] T. D. Bennett, D. J. Krajnovich, C. P. Grigoropoulos, P. Baumgart, and A. C. Tam, "Marangoni Mechanism in Pulsed Laser Texturing of Magnetic Disk Substrates," *Journal of Heat Transfer,* vol. 119, pp. 589-596, 1997.

[86] G. Karapetsas, N. T. Chamakos, and A. G. Papathanasiou, "Thermocapillary Droplet Actuation: Effect of Solid Structure and Wettability," *Langmuir,* vol. 33, pp. 10838-10850, 2017/10/17 2017.

[87] Y. Sui, "Moving towards the cold region or the hot region? Thermocapillary migration of a droplet attached on a horizontal substrate," *Physics of Fluids,* vol. 26, p. 092102, 2014.

[88] Y. Kamotani, S. Ostrach, and M. Vargas, "Oscillatory thermocapillary convection in a simulated floating-zone configuration," *Journal of Crystal Growth,* vol. 66, pp. 83-90, 1984/01/01/ 1984.

[89] Y. Kamotani and S. Ostrach, "Theoretical Analysis of Thermocapillary Flow in Cylindrical Columns of High Prandtl Number Fluids," *Journal of Heat Transfer,* vol. 120, pp. 758-764, 1998.